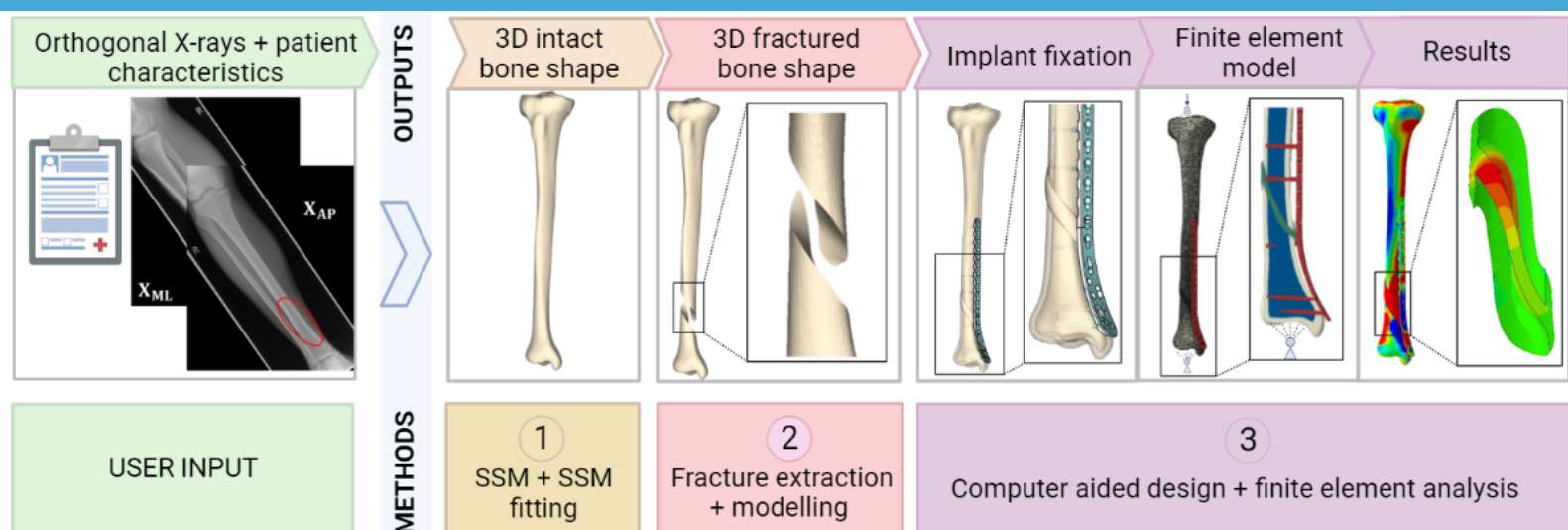


The development of a computational workflow for the semi-automated construction of patient-specific finite element models of tibial fracture fixation

Jet Zoë Moolenaar

2022-2023



MSc thesis in Biomedical Engineering

The development of a computational workflow
for the semi-automated construction of patient-
specific finite element models of tibial fracture
fixation

Jet Zoë Moolenaar

2022-2023

Jet Zoë Moolenaar: *The development of a computational workflow for the semi-automated construction of patient-specific finite element models of tibial fracture fixation (2023)*

The work in this thesis was carried out in the:

- Computational Mechanobiology research group, Berlin Institute of Health at Charité, Universitätsmedizin Berlin, Julius Wolff Institute, Germany;
- Department of Biomechanical Engineering, Delft University of Technology (TU Delft), Delft, the Netherlands

Supervisors: Prof.Dr. Sara Checa

Dr. Nazli Sarkalkan Tümer

ABSTRACT

Introduction: Tibial fracture healing complications occur frequently with reported non-union rates up to 23%. Preoperative patient-specific finite element (FE) modelling of fracture fixation may help to minimize these complications. However, developing such models requires labour-intensive work including (manual) segmentation of bones from medical images, making them unpractical for clinical applications. This study aims to establish a semi-automated workflow for the development of three-dimensional (3D) patient-specific FE models of long bone fractures based on two-dimensional (2D) X-ray images and patient characteristics.

Methods: A statistical shape model (SSM) of the tibia was developed based on computed tomography (CT) scans of subjects without tibial fractures. Using this model, shape parameters were correlated to patient characteristics, including gender, age, weight, and height of the subjects, using multilinear regression. Thereafter, strategies were developed to (1) fit the SSM of the tibia to a previously unseen fractured tibia based on two orthogonal X-rays and patient characteristics to estimate its intact 3D shape, and to (2) automatically model the fracture lines as detected on the X-rays in the intact tibia model. Using the automatically created geometries of the fractured tibia, FE models of the stabilized fracture were developed in Abaqus/CAE and used to investigate strains within the callus under post-operative loading conditions. The workflow was tested on one patient and the strains obtained from the FE models within the fracture region were compared to strains reported in the literature.

Results: An SSM of the tibia was successfully developed based on CT scans of 25 subjects (15 male, age = 60 ± 5.5 ; 10 female, age = 51 ± 7.1). The first five shape modes captured 90% of the total shape variation in the studied population. Significant correlations were found between the first shape mode, which described shape changes in the tibial length, and patient gender, age, weight, and height. SSM-to-patient fitting was achieved with a mean error of 0.81 mm and a maximum error of 4.22 mm. FE analysis of the stabilized fracture predicted inter-fragmentary compressive strains between 0 and 10% with a median value of 2%. Increasing the fixation working length by 13 mm, led to a 10-fold increase in the predicted median compressive strains.

Discussion and Conclusions: A workflow for the semi-automated generation of FE models of tibia fractures was successfully established. Patient-specific FE analysis results predicted strains within the fracture in a range reported for optimal bone formation. Additionally, predicted strains were highly dependent on the fixation configuration and material, most notably the fixation working length. Future work should focus on fully automating the suggested workflow and on the validation of the results. Ultimately, such a workflow could be used to formulate individualized treatment recommendations during the early pre- and post-operative phase in tibial fracture management to prevent non-union development.

ACKNOWLEDGEMENTS

With this thesis, I wrap up my seven years as a student at the Delft University of Technology, which started with a bachelor's in Clinical Technology and which I now conclude with a master's in Biomedical Engineering. However, for me this did not mean that I only browsed around Delft all these years. I feel privileged to have had the opportunity to fulfil parts of my curriculum in Leiden, Rotterdam, The Hague, Amsterdam, Cape Town (South Africa), Waterloo (Canada), Leuven (Belgium) and finally, to top it all off, Berlin (Germany)! I am incredibly grateful to have received such a rich, international, and multi-faceted education, where I had ample opportunity to explore different countries, research areas and healthcare systems and to challenge and reinvent myself continuously. This thesis, which I conducted during this last year at the Julius Wolff Institute in the Charité hospital in Berlin, on the topic of patient-specific preoperative planning of bone fracture surgery, forms a wonderful capstone to this time.

Already during my (more clinically oriented) bachelor's, my interests in the field of musculoskeletal biomechanics and patient-specific modelling were first triggered, by many clinical cases and applications that I saw during lectures and clinical rotations. When I learned more about the programming, physics and biology behind such applications, this interest was even more firmly established and decided to make it the focus of my master's. What I love about this research area, is that this is one of the fields where biology and engineering really meet, and which has the potential to radically impact patients' lives.

During my master thesis research at the Julius Wolff Institute, I got the opportunity to work on a highly translational project and to apply my knowledge to real-life applications affecting patients. The long-term goal of this project - being able to efficiently predict the most optimal fracture fixation strategy for individual patients - was highly motivating. Although it was overwhelming and extremely challenging at times, I hope my research made a (small) contribution to achieving this goal.

During this project, I got support from and met many wonderful people, who I would like to thank personally. First of all, my daily supervisor Sara, who has been extremely involved and motivating during all stages of this project, but who also gave me plenty of freedom to define my goals and shape the project according to my own interests. Together with my TU Delft supervisor Nazli, you also encouraged me to pursue the publication of my literature review and the presentation of my results at the CMBBE in Paris later this year, which I am very proud of and excited about. I would also like to thank Nazli, not only for your encouragement in these matters but also for your great ideas about the project, your critical thinking and your feedback that really helped me improve the manuscript and see the bigger picture. I also want to thank everyone at the Julius Wolff Institute for having me and for providing inspiration and feedback during this year. I especially wish to express my thanks and love to all the members of my research group in Berlin: Mahdi, Chiara, Giorgio, Vincenzo, Özgür, Olia, Philipp, Britt, Vahid, Siddarth (and Amaria). Thank you all for making me feel welcome in the group and Berlin from the start, for the fun times and words of encouragement and advice during many coffee breaks, lunches, dinners, and group meetings... A special shout-out to Madhi and Amaria, who I spent nearly every day with at the institute during the first few months when many of us were still doing home office – this process was a lot more fun because of you! Furthermore, I want to extra thank Özgür for your

guidance during different stages of the project and, together with Prof.Dr. Amir Zadpoor, for taking the time to be on my graduation committee. Finally, many thanks to my parents and friends for always supporting me in all my endeavours!

Lastly, thank you all for taking the time to read this research and I hope you enjoy it!

Jet Zoë Moolenaar

Amsterdam, February 2023

CONTENTS

Abstract.....	4
Acknowledgements.....	5
Contents	7
List of Figures.....	10
List of Tables	14
Nomenclature.....	15
1 Introduction.....	16
1.1 Clinical motivation.....	16
1.2 Background	17
1.2.1 Biomechanics influences bone fracture healing	17
1.2.2 (Tibia) fractures.....	17
1.3 State-of-the-art in virtual surgical planning of fracture fixation	21
1.3.1 Limitations of current virtual surgical planning tools	22
1.4 Research objectives.....	22
1.5 Thesis outline	23
2 Materials & Methods.....	24
2.1 Step 1: Development of a patient-specific intact 3D tibia model based on two orthogonal X-rays & patient characteristics.....	25
2.1.1 SSM building.....	26
2.1.2 Multilinear regression model building.....	32
2.1.3 SSM-to-patient fitting using patient characteristics & orthogonal X-rays.....	33
2.2 Step 2: Development of a patient-specific fractured 3D tibia model based on the intact 3D bone shape and orthogonal X-rays	41
2.2.1 Extracting approximate 3D fracture line coordinates using orthogonal X-rays	42
2.2.2 Modelling the 3D fracture lines in the intact tibia model	43
2.3 Step 3: FE analysis of the fixated fractured tibia	45
2.3.1 Assembling bone fracture geometries & fixation device	46
2.3.2 FE model building & analysis.....	48
3 Results	55
3.1 Tibial SSM.....	55

3.1.1	Training data acquisition.....	55
3.1.2	Segmentation.....	56
3.1.3	Automated pre-alignment performance	56
3.1.4	Initial estimated means.....	56
3.1.5	Establishing correspondences: morphing performance.....	57
3.1.6	Principal component analysis.....	57
3.2	Multilinear regression models.....	60
3.3	SSM-to-patient fitting.....	61
3.3.1	Fractured patient case	61
3.3.2	Intact validation case.....	63
3.4	FE analysis.....	65
3.4.1	Mechanical strains and motions within the fracture region.....	65
4	Discussion.....	72
4.1	Tibial SSM.....	72
4.2	Multilinear regression models.....	73
4.3	SSM-to-patient fitting.....	74
4.4	Fracture line modelling.....	74
4.5	FE models & analysis	75
4.5.1	Geometries and meshing.....	77
4.5.2	Materials	77
4.5.3	Interactions & boundary conditions	77
4.5.4	Loading	78
4.6	Future outlook	78
5	Conclusions	80
6	Appendices.....	82
	Appendix A: Segmentation methods in 3D Slicer	82
	Appendix B: SSM-to-patient fitting and fracture line back-projection.....	83
	Appendix C: DRR Generation in 3D Slicer and pre-processing	89
	Appendix D: Postprocessing in Meshmixer	91
	Appendix E: Post-processing & assembly in SOLIDWORKS	93
	Appendix F: Pre-processing & assembly in Abaqus/CAE.....	97
	Appendix G: Details FE analysis results	98

7 Bibliography..... 100

LIST OF FIGURES

Figure 1: Basic structure of the tibia. <i>Note:</i> Adapted from Zhang and McCully [23].	18
Figure 2: Anatomy of the human tibia, including the main bony features. <i>Note:</i> From <i>Essential clinical anatomy</i> by Moore, K. L., Agur, A. M. R., & Dalley, A. F. (2015), p. 316 [24].	19
Figure 3: Axes of the tibia. Frontal and sagittal views. <i>Note:</i> Adapted from <i>Principles of Deformity Correction</i> by Paley, D. (2002), p.2 [25].	19
Figure 4: Graphical abstract of the review on the state-of-the-art in virtual surgical planning (VSP) [10].	22
Figure 5: Overview of the proposed computational workflow. SSM: statistical shape model, 3D: three-dimensional.	25
Figure 6: Step 1 of the workflow, <i>i.e.</i> , development of a patient-specific intact 3D tibia model based on two orthogonal X-rays and patient characteristics.	25
Figure 7: Overview of steps taken to build the statistical shape model. GPA: Generalized Procrustes Analysis, PCA: Principal Component Analysis, SD: standard deviation, A: anterior, L: lateral, P: posterior.	27
Figure 8: Overview of the main steps of the SSM-to-patient fitting algorithm. Blue dots (0,2,3): indicated contour points on the X-rays of the given patient, Red boxes (0,2): automatically computed bounding boxes using the indicated contour points of the given patient (0) and projections of the SSM realization (2) respectively, Red contours (3): automatically computed contours of the projections of the SSM realization. <i>Note:</i> X-rays are from the test case of the patient with a spiral diaphyseal tibial fracture.	34
Figure 9: Preoperative (A-B) and postoperative (C-D) X-rays of the fractured tibia patient case used to test the success of the workflow. A: frontal view; preoperative, B: lateral view; preoperative, C: frontal view; postoperative, D: lateral view; postoperative.	35
Figure 10: Digitally reconstructed radiographs (DRRs) generated using the computed tomography (CT) scans of the intact validation case.	36
Figure 11: Custom-made GUI that requires the user to indicate the contour points on the AP and ML X-rays. AP: anteroposterior, ML: mediolateral. <i>Note:</i> X-rays are from the test case of the patient with a spiral diaphyseal tibial fracture.	37
Figure 12: Definition of the repeatable coordinate system with respect to the 3D tibia instance and its projections. x-axis = 2nd principal axis. y-axis = 3rd principal axis. z-axis = 1st principal axis. Origin: most inferior, lateral, anterior point of the 2D projections of the 3D shape.	38
Figure 13: Assumed X-ray projection setup for anteroposterior (AP) in orange and mediolateral (ML) projections in blue. SOD: source-object-distance, OID: object-imager-distance, SID: source-imager-distance, S: superior, P: posterior, M: medial.	39
Figure 14: Positioning of the leg for tibia anteroposterior (AP) and mediolateral (ML) X-ray imaging of the tibia in clinical practice. <i>Notes:</i> the pictures on the left and right are adapted	

from [57] and the picture in the middle was generated using the CT scan and tibia segmentation of the intact validation case.....	39
Figure 15: Projection of a point in a point cloud onto a plane. <i>Note:</i> From [58]	40
Figure 16: Overview of steps taken to achieve fracture line extraction from X-rays and modelling of the fracture lines into the intact 3D bone shape. <i>Note:</i> X-rays are from the test case of the patient with a spiral diaphyseal tibial fracture.	42
Figure 17: Custom-made GUI that requires the user to indicate the fracture line points on the AP X-ray and the shaft diameter on AP and ML X-rays. AP: anteroposterior, ML: mediolateral, fracture 1 (red): anterior fracture line, fracture 2 (purple): posterior fracture line, diameter (orange x): two points representing the outer edges of the tibial diaphysis at the level of the fracture. <i>Note:</i> X-rays are from the test case of the patient with a spiral diaphyseal tibial fracture.....	43
Figure 18: Constructed polyhedrons used to clip intact 3D bone shape into two bone fracture fragments. FL_A : anterior fracture line, FL_P : posterior fracture line.	44
Figure 19: Postprocessing of the fracture fragment geometry - smoothing & closing.	45
Figure 20: Reconstruction of the inner cortical bone surface: off-set outer cortical surface by - 5 mm.....	45
Figure 21: Reconstruction of the callus geometry: extrude surface around the fracture lines by 2 mm.	45
Figure 22: Cortical bone fragments, bone marrow and callus geometries after postprocessing in SOLIDWORKS. Left: frontal Right: lateral.	45
Figure 23: Step 3 of the workflow, <i>i.e.</i> , finite element (FE) analysis of the fixated fractured tibia.	46
Figure 24: Assembly of the stabilized fracture of the test case of the patient with a spiral diaphyseal tibial fracture according to postoperative X-rays (scenario 1/5). Bold text: used screw holes.	47
Figure 25: Alternative fixation scenarios considered for biomechanical analysis. Bold text: used screw holes.	48
Figure 26: FE model of the fixated fractured tibia (scenario 1/5) including boundary conditions, loads and materials. Models of the other scenarios were equivalent.....	48
Figure 27: Meshes of the different geometries. Green: callus, Blue: bone fragments (white: cortical bone, blue: bone marrow, Red: locking plate and screws.	50
Figure 28: Applied constraints, boundary conditions and loads in the developed FE model(s). <i>Note:</i> Scenario 2 is depicted here, the other scenarios are equivalent. U: displacement, CF: concentrated force.	52
Figure 29: The defined node pairs, local coordinate systems and path used for post-processing of the finite element analysis. A: node-pairs and local coordinate systems. B: path. Constant y-coordinate in the global coordinate system ($y = 45$ mm).....	54
Figure 30: Univariate distributions of characteristics of the subjects used for the SSM.	55

Figure 31: Multivariate distributions of characteristics of the training subjects used for the SSM. p : p -value, r : Pearson correlation coefficient, *: significant correlation.....	55
Figure 32: Inspection of mesh quality after segmentation and triangulation. The detail shows step artefacts.....	56
Figure 33: Shape alignment and estimation of the mean shape. A: unaligned tibiae. B: pre-aligned tibiae. C: Initial estimated mean computed using signed distance functions of pre-aligned tibiae without correspondences. D: second estimated mean computed by averaging the coordinates of the initial morphed training shapes. The details show that step artefacts are smoothed out.....	56
Figure 34: Hausdorff distance of original mesh (target) compared to the morphed mesh of one subject. A: morphed using the initial mean. B: morphed using the second mean.	57
Figure 35: Captured variation per principal component (PC). All the PCs up to an accumulated captured variance of 0.9 were retained, <i>i.e.</i> , 5 PCs.	58
Figure 36: Mean tibia shape and shape variations described by the first five PCs. PC: principal component (=shape mode), SD: standard deviation, A: anterior, L: lateral, P: posterior.....	58
Figure 37: Distance maps between the tibial shape at the extremities (+3SD or -3SD) and the mean tibial shape. PC: principal component (= shape mode), SD: standard deviation. A: anterior, L: lateral, P: posterior, arrows: direction of shape change.....	59
Figure 38: Pearson correlation coefficients (r) between patient characteristics and shape model parameters (b_s) in the training population. Significant correlations are indicated with *.....	60
Figure 39: Fit of (2) bounding box optimized and (3) contour fitted SSM shape realization as compared to the anterolateral (AP) and mediolateral (ML) X-ray contours of the fractured patient case. Beige: optimized SSM shape realization. Red boxes: bounding boxes. Red lines: concave hulls. Blue dots: contours as indicated on AP and ML X-rays. Distances are measured between the indicated contour points and the concave hulls of the projected shape realization.	62
Figure 40: Reconstructed shapes using (0) the mean of the SSM, (1) multilinear regression, (2) bounding box fitting and (3) contour fitting as compared to the true segmented 3D shape for the intact validation case. Left column: Hausdorff distances of the reconstructed shape to the true shape. Right column: Overlay of the reconstructed shape and the true shape.....	64
Figure 41: Maximum absolute principal strain [-] distribution of the fixated fractured tibia. Green box: callus region. Blue box: tibia bone region. Pink box: locking plate.....	66
Figure 42: Boxplots of the minimum (A) and maximum (B) principal strains [-] within the callus for the five different fixation scenarios (S1-S5). Lower and upper box boundaries: 25 th (Q1) and 75 th (Q2) percentiles respectively, making up the interquartile range (IQR). Line inside box + number: median. Lower and upper error lines: $Q1 - 1.5 \cdot IQR$ and $Q2 + 1.5 \cdot IQR$ respectively.....	67
Figure 43: Minimum principal strains [-] found along the path in the callus for the five different fixation scenarios. The path runs from lateral to medial, <i>i.e.</i> , from far-cortex to near-	

cortex relative to the plate. Shaded region: reported optimal strain range for bone formation [13]. *Notes:* the scale of the callus is larger compared to the plate for visualization purposes; lines of S1 and S4 overlap..... 68

Figure 44: Maximum principal strains [-] found along the path in the callus for the five different fixation scenarios. The path runs from lateral to medial, *i.e.*, from far-cortex to near-cortex relative to the plate. *Notes:* the scale of the callus is larger compared to the plate for visualization purposes; lines of S1 and S4 overlap..... 69

Figure 45: Relative interfragmentary motions (IFMs) (mm) in the axial (A) and shear (B) directions between three node pairs in the callus region for the five different scenarios. The motions are quantified in the local coordinate systems defined by the node pairs, *i.e.*, relative to the fracture lines..... 70

LIST OF TABLES

Table 1: Characteristics of the cases used to test the success of the workflow.....	36
Table 2: Summary of the used number of elements and element sizes of each part.....	51
Table 3: Material properties assigned to the bone tissues and implants.	51
Table 4: Variance inflation factor (VIF) after centring to assess multicollinearity between the explanatory variables.....	60
Table 5: Regression coefficients (w) of the multilinear regression models relating patient characteristics to shape model parameters (b_s).	61
Table 6: Bounding box dimensions of the contours as measured on X-ray compared to bounding box dimensions of the projected reconstructed shapes of the fractured patient case. AP: anteroposterior, ML: mediolateral.....	61
Table 7: Bounding box dimensions of contours as measured on X-ray compared to bounding box dimensions of projected reconstructed shapes of intact validation case. AP: anteroposterior, ML: mediolateral.	63
Table 8: Distances between concave hulls of reconstructed shape as compared to contours as indicated on X-rays of intact validation case. AP: anteroposterior, ML: mediolateral.....	63

NOMENCLATURE

2D 2-dimensional	SMD standardized mean difference
3D 3-dimensional	SOD source-object-distance
AP anteroposterior	SSAM statistical shape and appearance model
API application programming interface	SSM statistical shape model
CAD computer-aided design	STL Standard Triangle Language
CF concentrated force	VIF variance inflation factor
CI confidence interval	VSP virtual surgical planning
CT computed tomography	
DICOM Digital Imaging and Communications in Medicine	
DRR digitally reconstructed radiograph	
FE finite element	
GUI graphical user interface	
ICP iterative closest point	
IFM interfragmentary motion	
IQR interquartile range	
LPS left, posterior, superior	
ML mediolateral	
MRI magnetic resonance imaging	
NURBS non-uniform rational B-spline	
OID object-imager-distance	
PC principal component	
PCA principal component analysis	
RMSE root-mean-square error	
RR risk ratio	
SD standard deviation	
SI International System	
SID source-imager-distance	

1 INTRODUCTION

1.1 Clinical motivation

The management of bone fractures remains a major challenge for orthopaedic surgeons. With bone fractures being the most common form of hospitalized trauma, they constitute a significant healthcare burden. A systematic analysis from The Global Burden of Diseases, Injuries, and Risk Factors Study (GBD) in 2019 estimated the global number of new fractures to be 178 million [1]. Since fracture rates increase with age, the GBD 2019 predicted that this number will increase even further in the coming years considering the ageing of the population. Fractures are especially common among people with osteoporosis and are associated with an annual cost of 37.5 billion euros and a loss of one million quality-adjusted life years in Europe [2]. Although bone has the ability to self-generate, fracture healing complications occur frequently and non-union rates of 5-10% of all fractures have been reported [3]. 89% of these non-unions occur in the lower limb [4]. Tibia fractures are considered especially problematic with non-union rates reaching up to 23% [5].

Surgical fixation of bone fractures, also called osteosynthesis, aims to restore the original anatomy of the bone and to create the appropriate mechanical conditions for bone healing [6]. Additionally, the fixation system should provide enough strength for the functional loads within the bone. The surgical treatment typically consists of two steps. First, the fragments are surgically reduced to their original anatomical sites and second, the bone is stabilized using fixation tools such as screws, nails, and plates. Suboptimal reduction and fixation can cause delayed bone union, traumatic arthritis [7], re-dislocation of fractures, and mal-/non-unions [8]. Revision surgery is required in 10-15% of all cases [9].

There are typically many options for fracture fixation and the optimal fixation for the individual patient is not straightforward. It is highly dependent on the bone geometry, fracture pattern and postoperative biomechanical conditions [10]. However, these conditions are hard to assess clinically. There is therefore a need to include patient-specific geometry and biomechanics in the preoperative planning of bone fracture fixation. Computer-aided preoperative planning or virtual surgical planning provides a way to do this. Recently, such tools have been developed that are increasingly being used in the field of fracture fixation surgery. The state-of-the-art in virtual surgical planning of bone fracture fixation surgery has been reviewed as part of this thesis [10] and the main results will be summarized in section 1.3. It was shown that while current computer-aided planning approaches are feasible to be used in clinical practice and improve clinical outcomes, there are two main limitations. First of all, the construction of patient-specific geometrical models of the fractured bone currently relies on thin-slice computed tomography (CT) scans of the entire fractured bone. Making a CT scan of the whole bone is usually not part of the clinical routine of bone fracture

management and the segmentation is labour-intensive and hard to automatize. The second limitation is that biomechanical analysis is currently rarely included in the planning framework, although biomechanical conditions are known to highly influence healing outcomes (see section 1.2.1). This knowledge remains to be incorporated into the planning routine.

1.2 Background

1.2.1 Biomechanics influences bone fracture healing

Fracture healing is influenced by a complex interplay of different factors, including (1) the severity of the initial injury, (2) host factors and local (3) biological and (4) mechanical factors [5], [11]. While the first three usually cannot be adequately controlled once the fracture has occurred, the mechanical fracture environment can still be influenced in the pre- and postoperative phases of fracture management.

The key to most bone healing theories is the concept that bone-forming tissues respond to strains – *i.e.*, the change of length of a material as compared to the initial length at a given mechanical load [12]. It has been suggested that the strain that stimulates soft callus formation is between 5-10% while the strain that stimulates osteoblasts to form bone is between 2-5%. Strains above 10% are generally associated with bone resorption [13]. Consequently, it has been proposed that non-unions of bone fractures may occur in two main biomechanical situations. Firstly, bone healing might fail when the fixation of the fracture does not reduce the strain to a level where healing can occur (*i.e.*, > 10%). A second non-union scenario may occur when the fixation construct is so stiff that the strain in the tissue is always lower than 2% [14].

These theories have been confirmed by many experimental studies, both *in vivo* and *in vitro* [18], [24], [26], [30]. Because the local strain values are not directly accessible *in vivo*, the mechanical environment is usually described by global mechanical factors such as gap size and interfragmentary motion (IFM). Additionally, many *in silico* studies exist that assessed the mechanical environment within the fracture zone and their relation to healing outcomes using finite element (FE) techniques [15]–[20]. Using these numerical techniques, it is possible to directly quantify strain values within the healing region of a fracture.

1.2.2 (Tibia) fractures

The prevalence of bone fractures varies strongly for different fracture locations and populations, *e.g.*, among ages, genders, and geographic regions. Increased fracture incidences arise mainly in males in the middle age groups due to lifestyle and in older individuals with osteoporosis [1].

Of all the long bones, the tibia has proven to be the most problematic considering fracture healing. This is likely due to the mechanical loading the tibia is subjected to and the biological environment of the bone [21]. Additionally, it is the most prevalent anatomical fracture site in

the body [1]. For this reason, and because the loading of the tibia is relatively straightforward to model [15], this thesis focuses on fractures of the tibia.

1.2.2.1 Anatomy of the tibia

The tibia or shinbone is one of the two bones that makes up the lower leg - the other being the fibula. Together with the femur, it is the long bone which is subjected to the most loading during daily activities [22]. For this reason, it is larger and stronger than its counterpart.

The basic structure of a long bone is depicted in **Figure 1**. Long bones consist of a diaphyseal segment, which is defined as the long midsection of the bone, with two rounded epiphyses at each end. The metaphysis is the portion between the epiphysis and diaphysis and contains the ossified growth plate. Long bone consists of three main layers: the periosteum, a layer of compact or cortical bone, and a layer of cancellous or trabecular bone. The trabecular bone contains the bone marrow in the medullary cavity.

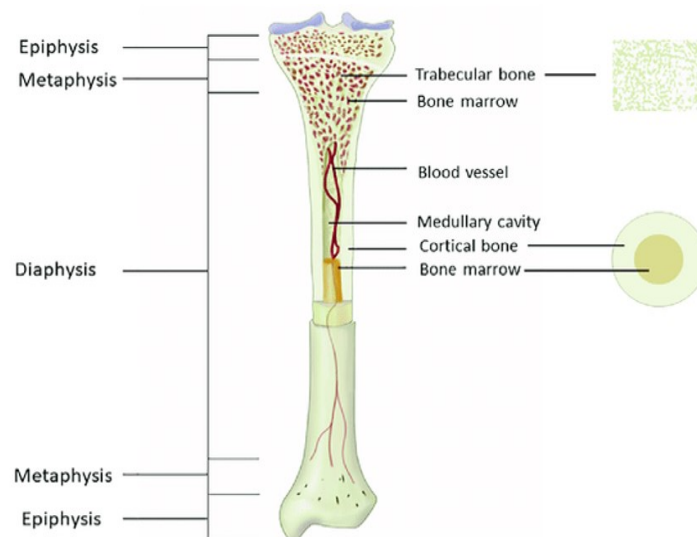


Figure 1: Basic structure of the tibia. *Note:* Adapted from Zhang and McCully [23].

The tibia articulates with the femoral condyles superiorly, the talus inferiorly, and the fibula laterally at its proximal and distal ends. The main bony features of the tibia are indicated in **Figure 2**.

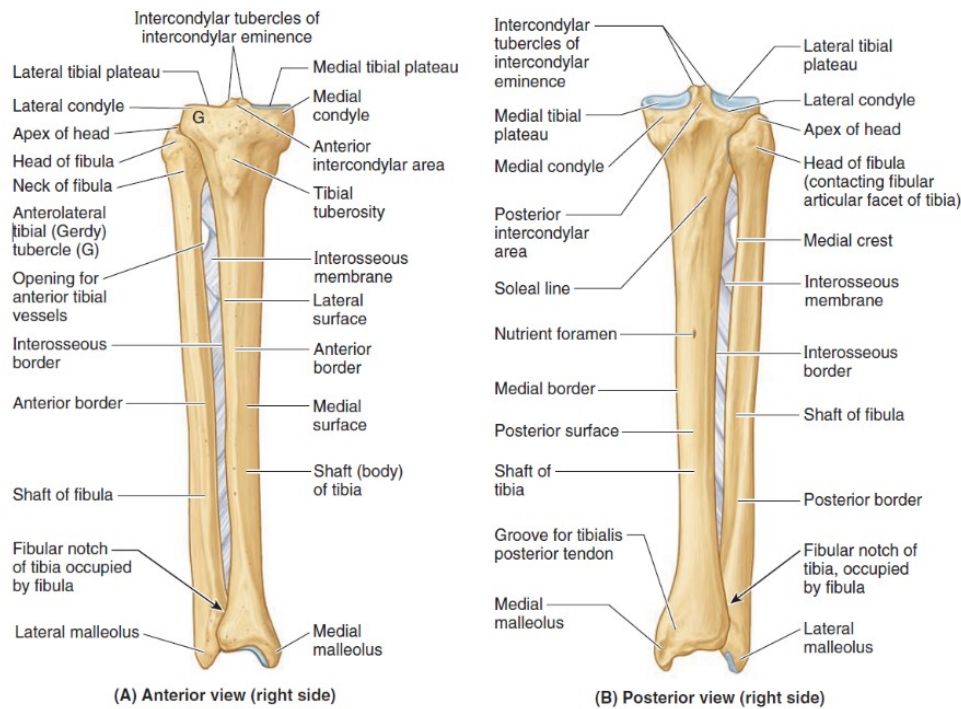


Figure 2: Anatomy of the human tibia, including the main bony features. *Note:* From *Essential clinical anatomy* by Moore, K. L., Agur, A. M. R., & Dalley, A. F. (2015), p. 316 [24].

Each long bone has both an anatomical axis and a mechanical axis [25]. The mechanical axis of a bone is defined as the straight line connecting the proximal and distal joint centres (**Figure 3A**). The anatomical axis is the mid-diaphyseal line running through the intramedullary canal (**Figure 3B**).

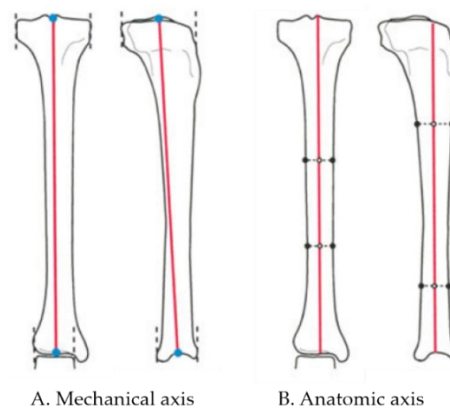


Figure 3: Axes of the tibia. Frontal and sagittal views. *Note:* Adapted from *Principles of Deformity Correction* by Paley, D. (2002), p.2 [25].

In the tibia, in the frontal plane, the two axes are parallel and only a few millimetres apart. In the sagittal plane, the mechanical axis is angled with respect to the anatomical axis.

1.2.2.2 Tibial fracture classification

The most widely accepted tibial fracture classification is the *AO fracture and dislocation classification* as developed by the AO Foundation [26], and this classification will also be adopted in this study.

The most frequent location of tibial fracture is in the diaphyseal segment (type 42A-C), more specifically at the junction of its inferior and middle thirds, where the tibial shaft is the narrowest. In this study, the focus is on simple diaphyseal fractures (type 42A), which is defined as a fracture with a single circumferential fracture line. The fracture pattern of a simple fracture can either be (1) spiral, (2) oblique or (3) transverse, and the focus of this study will be on spiral fractures (type 42A1).

The aetiology of simple fractures can involve both low-energy and high-energy mechanisms [27]. Spiral fractures are usually the result of indirect low-energy torsional forces. Transverse and oblique fractures are typically due to high-energy trauma. They are often associated with soft-tissue injury, compartment syndrome, bone loss, ipsilateral injury [27], and a higher risk of displacement, angulation, and slow healing [26].

1.2.2.3 Tibia fracture management

1.2.2.3.1 Imaging and planning

Tibia fractures are typically diagnosed and classified by physical examination and two planar radiographs (*i.e.* X-rays), taken in frontal and lateral planes [28]. In case the radiographs indicate the presence of either a complex fracture (>2 fragments) or an articular fracture (type 41/43), an additional CT scan is usually done. A particularity of long bone fractures is that the CT scan is usually limited to the fracture region only, not including information about the whole bone. In the case of simple spiral diaphyseal fractures (the focus of this study), a CT scan is not a part of the clinical routine [29].

1.2.2.3.2 Osteosynthesis

The treatment of bone fractures aims to reduce the fracture fragments to their anatomical position and stabilize the fragments until the fracture heals. In this thesis, the focus is on surgical reduction of the fracture followed by internal fixation. The surgical reduction and fixation of bone fractures is also termed osteosynthesis.

For diaphyseal tibial fractures, operative osteosynthesis with intramedullary nailing or plating is the gold standard [26]. Intramedullary nailing is preferred in the case of a normal medullary canal but is contra-indicated in the case of a deformed medullary canal of proximal or distal fractures. It may be difficult to achieve successful intramedullary nailing of these fractures because of the hourglass shape of the intramedullary canal, which prevents a tight endosteal fit [30]. In these cases, internal fixation with (locking) compression plates and screws is the preferred course of treatment [31].

There are two types of compression plates: conventional and locking compression plates. In conventional compression plating, lag screws are used to press the plate onto the bone. Stable fixation is achieved by friction between the plate and bone [26]. This can only be accomplished by adequate pre-contouring of the plate to match the contour of the reduced bone. Locked internal compression plating consists of plate and screw systems where screws are locked in the plate at a fixed angle. This is achieved by using threaded screw heads and corresponding

threaded plate holes [32]. Compared to conventional plating techniques, locked plating provides several advantages. Since the locking screws are engaged in the plate, tightening the screws does not cause the bone to be pulled towards the under-surface of the plate [33]. Because of this, cortical bone perfusion is not compromised as much as in conventional plating systems. Additionally, precise contouring of the plates is no longer necessary because the plate does not need to be pressed onto the bone to achieve stability. This may also prevent primary dislocation of fractures by inexact contouring of a plate [32].

Because of these advantages, and because locked plating requires choices regarding the optimal fixation configuration, this thesis will focus on the preoperative planning of simple spiral tibial diaphyseal fractures using locking compression plates.

1.2.2.3.3 Postoperative management

After plate fixation, progressive weight bearing is recommended after 8-12 weeks. As soon as callus formation is visible, the patient can start full weight-bearing [34].

1.3 State-of-the-art in virtual surgical planning of fracture fixation

As outlined in the previous section, there are typically many options for fracture fixation, and the optimal fixation is highly dependent on the bone geometry and fracture pattern. Therefore, the surgical treatment of bone fractures calls for detailed preoperative planning. Especially with locked plating, preoperative planning is key to success [35]. Many studies have shown that failures of the locking plate occur when the wrong screw configuration or working length is chosen for the fracture pattern [33], [35], [36].

Recently, virtual surgical planning tools have been developed with the aim to assist in the preoperative planning of bone fracture fixation surgery. The state-of-the-art of virtual planning of bone fracture fixation surgery was reviewed as part of this thesis [10]. The methods and results of this review are summarized in **Figure 4**. 79 articles were included to provide an overview of the state-of-the-art in virtual surgical planning. It was found that virtual surgical planning of bone fracture fixation typically consists of the following stages: (1) generation of three-dimensional (3D) patient-specific geometrical models using 3D medical imaging technologies such as CT, (2) virtual bone fracture reduction, (3) virtual bone fracture fixation and occasionally (4) analysis of surgical planning and (5) intra-operative guidance. 21 of the included studies were used to assess the feasibility and efficacy of computer-assisted planning methods. The reported total mean planning duration ranged from 22 to 258 minutes in different studies. Virtual surgical planning resulted in reduced operation time (standardized mean difference (SMD): -2.19; 95% confidence interval (CI): -2.87, -1.50), less blood loss (SMD: -1.99; 95% CI: -2.75, -1.24), decreased frequency of fluoroscopy (SMD: -2.18; 95% CI: -2.74, -1.61), shortened fracture healing times (SMD: -0.51; 95% CI: -0.97, -0.05) and less postoperative complications (risk ratio (RR): 0.64, 95% CI: 0.46, 0.90) as compared to conventional planning.

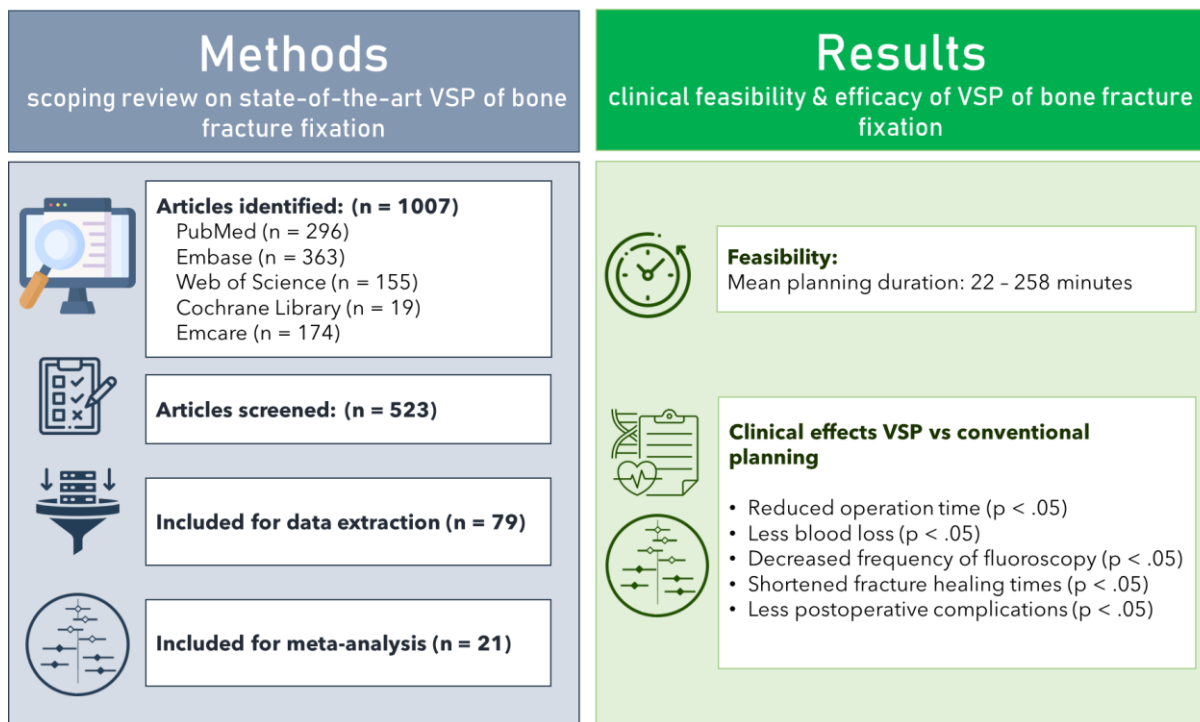


Figure 4: Graphical abstract of the review on the state-of-the-art in virtual surgical planning (VSP) [10].

1.3.1 Limitations of current virtual surgical planning tools

Two main limitations of current virtual surgical planning tools were identified in the review. First of all, the construction of patient-specific geometrical models of the fractured bone currently relies on thin-slice CT scans of the entire fractured bone. Making a CT scan of the whole bone is usually not part of the clinical routine of bone fracture management and the segmentation is labour-intensive and hard to automatize. The second limitation is that biomechanical analysis is currently rarely included in the planning framework.

There is therefore a need to develop a new workflow that fits within the current clinical routine of bone fracture management and that incorporates biomechanical analysis to determine the mechanical environment at the fracture site.

1.4 Research objectives

The general aim of this study is to establish a computational workflow for the semi-automated construction of 3D patient-specific FE models of fractured long bones based on two-dimensional (2D) X-ray images and patient characteristics. In this thesis, the focus is put on spiral diaphyseal tibial fractures treated with locking plates (see section 1.2.2). However, the workflow is developed in such a manner that it should be easily translatable to other long bones.

More specifically, this study aims to:

1. Develop a method to automatically generate an estimate of the patient-specific intact 3D bone shape based on two orthogonal X-rays and patient characteristics and assess its performance,

2. Develop a method to automatically introduce the patient-specific fracture lines as detected on two orthogonal X-rays into the intact 3D bone shape and assess its performance,
3. Using the automatically created geometries, develop FE models of the fixated fractured bone under post-operative loading conditions to determine the mechanical environment in the fracture region.

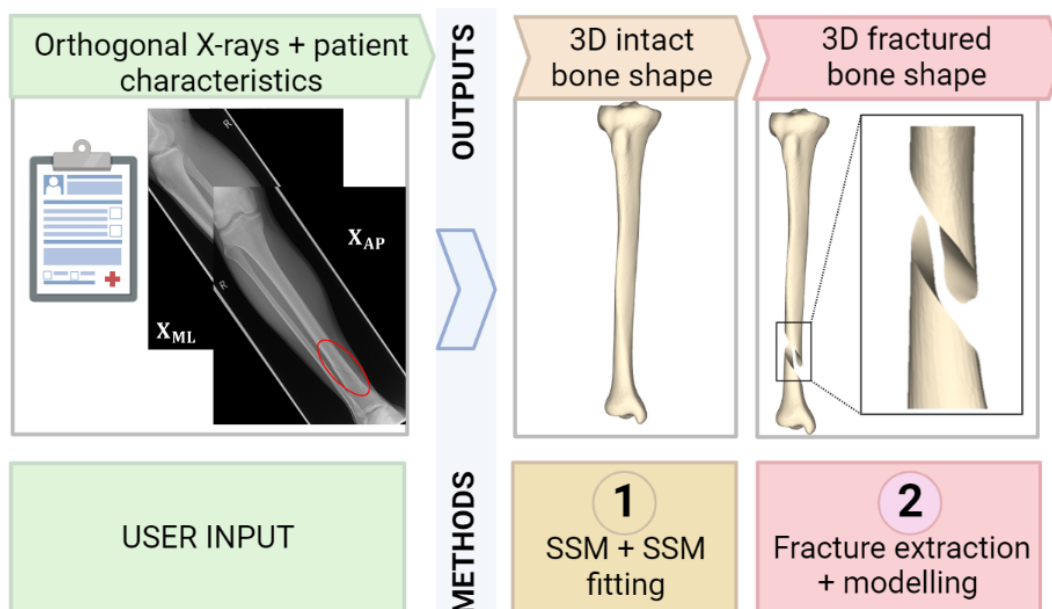
The success of the complete workflow (see **Figure 5**) is tested by applying it to one patient case with a non-displaced simple diaphyseal spiral fracture of the tibia, fixated with a locking plate.

1.5 Thesis outline

Throughout this report, the aforementioned research objectives will be addressed. In chapter 1, background is provided regarding (tibial) bone fractures and the state-of-the-art in preoperative planning of the surgical fixation of these fractures. With this background in mind, the objectives of this thesis are formulated. In chapter 2, the methods and tools used in this thesis are described. This includes methods and tools used to (1) develop a statistical shape model (SSM) of the intact tibia geometry, (2) semi-automatically fit the SSM of the intact tibia to two orthogonal X-rays of a fractured tibia, (3) semi-automatically extract and introduce the patient-specific fracture lines into the intact tibia geometry and to (4) build FE models and perform FE analyses of the fixated fractured tibia. In chapter 3, the results from the developed models (1,4) and methodologies (2,3) from chapter 2 are presented. In chapter 4, the results are evaluated. Furthermore, the assumptions and limitations of the current study are discussed. Finally, possibilities for future work are identified. Final conclusions are drawn in chapter 5.

2 MATERIALS & METHODS

In this chapter, a semi-automated workflow was developed to construct 3D patient-specific FE models of the fractured tibia based on 2D X-ray images and patient characteristics. The workflow is depicted in **Figure 5** and consisted of three main steps corresponding to the research objectives (see section 1.4). **Step 1** focused on a method to automatically estimate the intact 3D bone shape based on two orthogonal X-ray images and patient characteristics. This was achieved by (1.1) building a 3D SSM of the intact tibia and (1.2) developing an automatic method to fit the SSM of the healthy tibia to two orthogonal X-rays of a previously unseen fractured tibia to estimate its 3D shape. Multilinear regression models correlating patient characteristics with the shape parameter values of the SSM training shapes were used to initialize the SSM fitting. **Step 2** focused on a method to automatically introduce the fracture lines as detected on two X-rays into the intact 3D bone shape to obtain the 3D fractured bone geometries. This was achieved by (2.1) manually extracting fracture lines from the orthogonal X-rays and (2.2) developing a method based on polyhedron cropping to introduce these fracture lines into the 3D model. **Step 3** focused on the development of FE models of the fixated fracture using the automatically created geometries. This was achieved by (3.1) assembling and fixating the automatically created geometries using locking plates with different screw configurations and materials using computer-aided design tools and (3.2) building and analysing the FE models of the different fixation scenarios using FE analysis software.



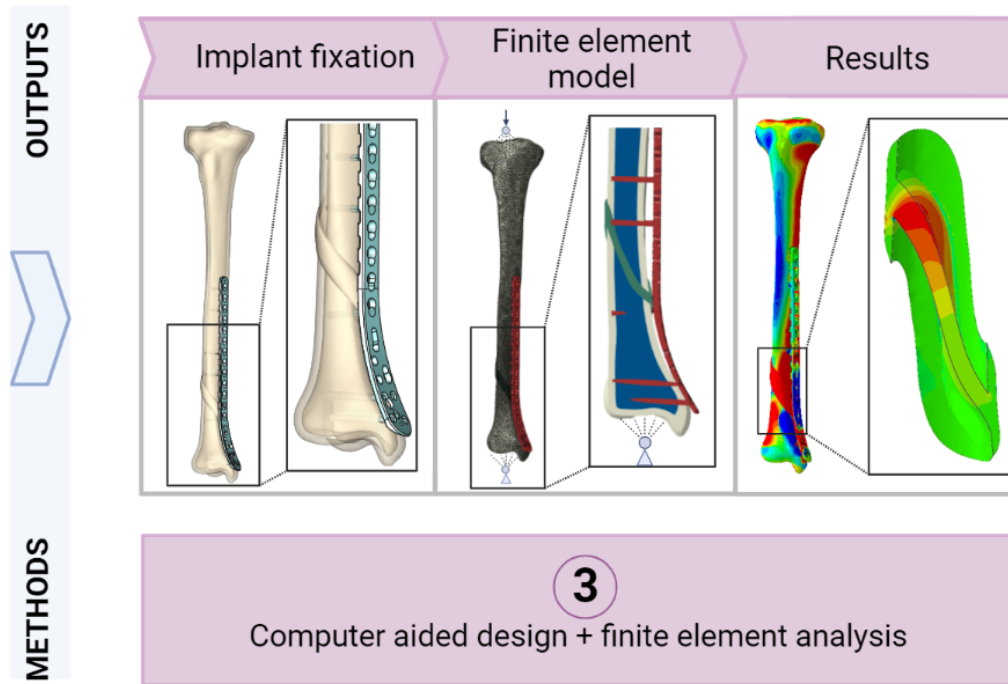


Figure 5: Overview of the proposed computational workflow. SSM: statistical shape model, 3D: three-dimensional.

2.1 Step 1: Development of a patient-specific intact 3D tibia model based on two orthogonal X-rays & patient characteristics

As part of **objective 1** of this study, a methodology was developed to generate an estimate of the patient-specific intact 3D bone shape based on two orthogonal X-rays and patient characteristics (see **Figure 6**). To achieve this, a statistical shape of the tibia was first developed based on a training cohort of healthy tibiae. Thereafter, a method was developed to fit the SSM of the healthy tibia to two orthogonal X-rays of a previously unseen fractured tibia to estimate its 3D shape. Multilinear regression models correlating patient characteristics with the shape parameter values of the SSM training shapes were used to initialize the SSM fitting.

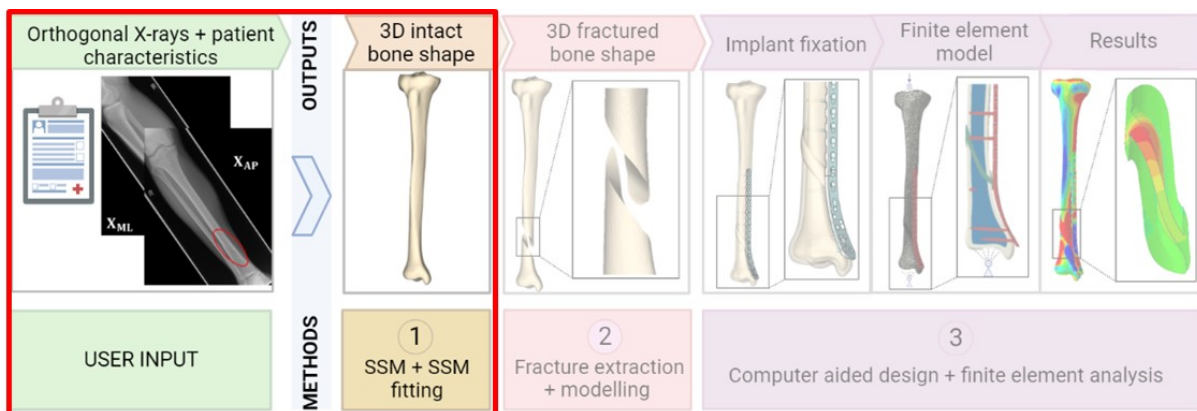


Figure 6: Step 1 of the workflow, *i.e.*, development of a patient-specific intact 3D tibia model based on two orthogonal X-rays and patient characteristics.

2.1.1 SSM building

SSMs of bones describe the mean shape within a certain population as well as the main modes of variation of shape [37]. Since their introduction in 1996 by Cootes and Taylor [38], they have been deployed for a wide variety of biomedical applications, such as automated segmentation, the design of orthopaedic implants, and the generation of 3D patient-specific bone models [37]. A 3D SSM is constructed based on a training dataset to provide the model with a priori knowledge about the expected shape distribution of the bone. In the case of 3D bone SSMs, the training set is usually based on CT or magnetic resonance imaging (MRI) images of the bone of interest. Development of an SSM typically consists of the following four main steps: (1) representation of bone shape, (2) establishing correspondences between training shapes, (3) alignment of training shapes using Generalized Procrustes Analysis (GPA), and (4) Principal Component Analysis (PCA) of the nodal coordinates of the training shapes. For more information on these general steps, the reader is referred to the review on SSMs of bones by Sarkalkan *et al* (2014) [37].

In this research, the process for developing this model included: (1) collection of bi-lateral cadaveric CT scans of 25 individuals (15 male, mean age: 60 ± 5 ; 10 female, mean age: 52 ± 7), (2) segmentation of 50 tibia shapes (*i.e.*, training shapes) from the CT scans, (3) rigid pre-alignment of the training shapes, (4) computation of the estimated mean shape (*i.e.*, template shape), (5) non-rigid surface registration of the template shape to each training shape to establish correspondences, (6) GPA to refine the alignment of the training shapes using correspondences and (7) PCA of the nodal coordinates of the training shapes. An overview of these steps is shown in **Figure 7**.

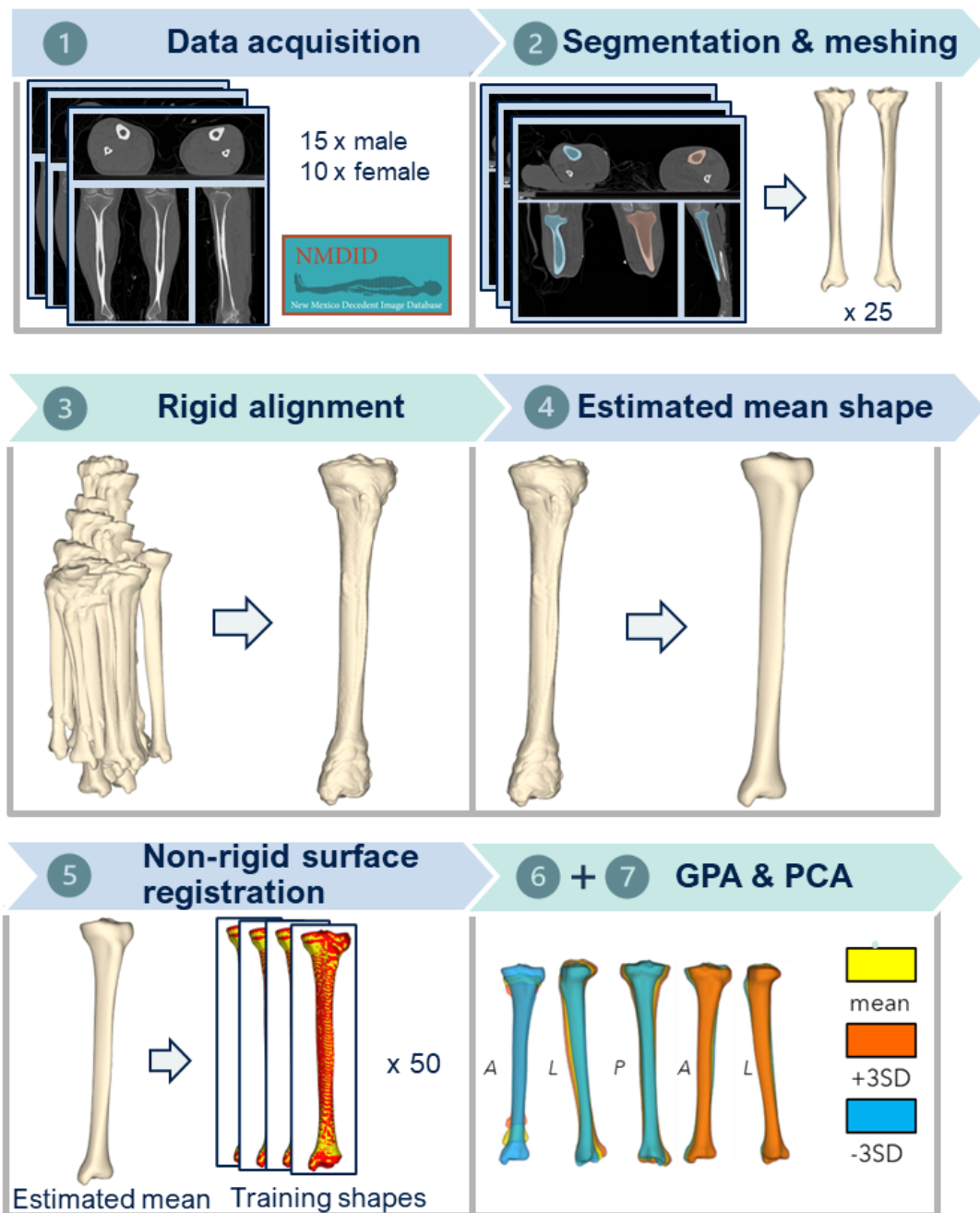


Figure 7: Overview of steps taken to build the statistical shape model. GPA: Generalized Procrustes Analysis, PCA: Principal Component Analysis, SD: standard deviation, A: anterior, L: lateral, P: posterior.

2.1.1.1 Training data acquisition

Bilateral high-resolution CT scans of the lower extremities were collected from the New Mexico Decedent Image Database¹ [39]. This database includes CT scans and metadata about the demography, life and death of New Mexicans who died between 2010 and 2017. Scans were only collected if they adhered to the following inclusion criteria:

- No cadaver decomposition
- No diabetes

¹ <https://nmdid.unm.edu/>

- No osteoarthritis
- No implants or fractures of the lower extremities
- Age, height, and weight available
- Age between:
 - Male: 51-71
 - Female: 38-68

The age range was determined based on the training cohort used by Tümer *et al* (2019) [40], who included 55 male (mean age: 61 ± 10) and 11 female (mean age: 53 ± 15) training subjects. For the selected individuals, the database ID, gender, age (years), height (cm), and weight (kg) were also collected.

All CT scans were acquired using the following acquisition parameters: tube voltage 120 kVp, effective dose 200 mAs, scan length 800-1000 mm, pitch 0.942, collimation 16 x 0.75, rotation time 1.0 sec. Tomographic reconstructions were made with a field of view of 500 mm, a slice increment of 0.5 mm, a slice thickness of 1 mm, and a matrix size of 512 x 512.

2.1.1.2 Segmentation

All left and right tibiae were segmented from the CT scans using the open-source software package 3D Slicer² (Version 4.11) [41]. Segmentation was done semi-automatically using the steps detailed in *Appendix A*, using a combination of thresholding and manual adjustments. Only the outer contours were included, omitting the trabecular bone geometry from the SSM. All right tibia segmentations were mirrored in the sagittal plane to obtain only left tibiae.

2.1.1.3 Triangulated bone surfaces

Next, the segmentations were exported as standard triangle language (STL) files, resulting in 50 surface meshes. The surface meshes were automatically generated by the 3D Slicer software in their original scale and in an LPS (left, posterior, superior) coordinate system. The default resolution was used, which is computed such that the label map contains a total of approximately 256x256x256 voxels. The resulting meshes had a varying number of vertices of approximately 100.000.

2.1.1.4 Rigid pre-alignment

All training shapes were pre-aligned to minimize differences in pose (*i.e.*, translation and rotation). This was done using a custom-made python script. Each mesh was first translated to the origin of a common coordinate system by averaging the x , y , and z coordinates of the mesh points and subtracting them from the original x , y , and z coordinates. Meshes were not scaled to unit centroid size as is often done to correct for differences in scale [42]. Differences in scale arise mostly from the use of different CT protocols. Since the collected CT scans were all acquired using the same protocol, this was deemed unnecessary. Additionally, it is

² <https://www.slicer.org/>

desirable to keep the original scale for easier physical interpretation and it is expected that the scale is also correlated with patient characteristics.

After translation to the origin, the iterative closest point (ICP) registration algorithm [43] was employed to refine the initial transformation. This algorithm requires a source point cloud and a target point cloud as inputs. The vertices of the training shapes were extracted to obtain point cloud representations of the training shapes. One randomly picked training shape was used as a target point cloud to register all other training shapes (*i.e.*, source point clouds) to. The point-to-point implementation of the algorithm in the `Open3D` python library³ was used. The algorithm performs two steps. First, a correspondence set $K = (p, q)$ is defined by matching each point from the target point cloud P to the closest point in the source point cloud Q . Subsequently, an initial transformation matrix T is updated by minimizing an objective function $E(T)$, which is defined over the correspondence set K . The objective function used is the point-to-point objective function:

$$E(T) = \sum_{(p,q) \in K} |p - Tq|^2 \quad (1)$$

Minimization of the objective is done in an iterative manner: at each iteration i , the previous T^{i-1} is used to find q^{i-1} . Residuals and Jacobian matrices are calculated to find the minimum.

2.1.1.5 Computation initial estimated mean

To establish correspondences between the training shapes, it was necessary to first obtain an initial estimated mean shape (see section 2.1.1.6 below). For this purpose, each of the pre-aligned meshes was converted to a continuous signed distance function representation, with the surface as the zero-level. This was done using the `pysdf`⁴ library in python. The continuous distance functions were then discretized using an evenly spaced grid consisting of 200 points along each axis. The discrete signed distance functions were averaged, and the marching cube method was applied on the zero level of the average to obtain the surface mesh of the mean shape. The marching cubes implementation of the `skimage`⁵ package in python was used.

The estimate of the mean tibia shape was remeshed in MeshLab⁶ (version 2022.02) [44] to have 31.471 vertices in line with the work of Tümer *et al* (2019) [40]. To make sure the mesh was of high quality, it was checked for various properties using Amira (version 6.0.1., Zuse Institute Berlin, Germany). These properties included intersections, holes, manifolds, triangle orientation, triangle aspect ratio, and tetra quality. For the last two properties, a threshold of 25 was adopted, as per the Amira guidelines [45]. The training shapes were also decimated to have the same number of vertices (*i.e.*, 31.471), which is necessary for the next step. Decimation

³ http://www.open3d.org/docs/latest/tutorial/Basic/icp_registration.html

⁴ <https://pypi.org/project/pysdf/>

⁵ https://scikit-image.org/docs/stable/auto_examples/edges/plot_marching_cubes.html

⁶ <https://www.meshlab.net/>

was performed automatically using the quadric edge collapse algorithm which is implemented in MeshLab.

2.1.1.6 *Establishing correspondences: non-rigid surface registration*

Dense correspondence between the training shapes was established using a morphing approach [46]–[48]. The idea is to deform the same template shape over all the training shapes using non-rigid surface registration, to establish iso-topological meshes and one-to-one correspondences. An advantage of this approach is that the mesh quality of the template shape is maintained during morphing. The morphing was performed using the surface registration module of Piper⁷ (version 1.1.0., European Commission) which relies on a non-rigid ICP registration algorithm using local surface descriptors [49]. The suitability of the surface registration of Piper for statistical shape modelling was demonstrated in previous work by Richthofer *et al* (2022) [50]. The parameters for the surface registration were kept to their default values (*i.e.*, iterations: 20; curvature precision: 5; smoothing iterations: 2). The estimated mean shape (template shape) was used as a source and registered to the training shapes (targets).

Since this module of Piper is not available in scripting or batch mode, a custom-made Autohotkey⁸ script was written for graphical user interface (GUI) automation. In this way, the morphing was automatically performed for each of the training shapes.

The geometrical fit of the morphed meshes as compared to the original training shapes was inspected by computing the Hausdorff distances between the surfaces using MeshLab [51]. This Hausdorff distance algorithm in MeshLab samples one surface and computes the closest distance to the other surface. Inspection of the Hausdorff distances revealed some high local morphing errors. The reason for this was that the initial estimate of the mean shape (see above, section 2.1.1.5) was missing the medial malleolus because of differences in the length of the different subject tibiae (see Results, section 3.1.4). For this reason, the mean tibia shape as obtained by averaging the coordinates of the initial morphed training shapes was used for a second round of morphing.

2.1.1.7 *GPA*

Using the iso-topological meshes created in the previous step, the initial pre-alignment was further refined using partial GPA [52]. Partial GPA determines the optimal transformation (translation and rotation) that minimizes the sum of squared distances between the corresponding points. Partial GPA, as opposed to full GPA, does not include scaling of the shapes to preserve the size of the shapes. GPA was carried out using a python implementation⁹ of the rigid 3D transform algorithm from Arun *et al* (1987) [53].

⁷ <http://www.piper-project.eu/start>

⁸ <https://www.autohotkey.com>

⁹ https://github.com/nghiaho12/rigid_transform_3D/commit/e6aaed2f9c5827192b001644412e9b7dfc5535e6

2.1.1.8 PCA

After alignment, the nodal coordinates of the different shapes are assumed to represent only shape variations. PCA was performed on the nodal coordinates of the different aligned training shapes to obtain the average shape and the main modes of variation of the training shapes from the average shape. The average shape $\bar{\mathbf{x}}$ is calculated as:

$$\bar{\mathbf{x}} = \frac{1}{N} \sum_{i=1}^N \mathbf{x}_i \quad (2)$$

with \mathbf{x}_i the training shapes and N the number of training shapes. The variation of the training shapes from the mean is calculated using the covariance matrix \mathbf{S} :

$$\mathbf{S} = \frac{1}{N-1} \sum_{i=1}^N (\mathbf{x}_i - \bar{\mathbf{x}})(\mathbf{x}_i - \bar{\mathbf{x}})^T \quad (3)$$

Eigenvalue decomposition is performed on the covariance matrix to obtain the main modes of variation of the training shapes from the average shape using:

$$\mathbf{S} = \mathbf{\Phi} \mathbf{\Lambda} \mathbf{\Phi}^T \quad (4)$$

With $\mathbf{\Phi} = [\phi_1 \dots \phi_c]$ the matrix containing the c eigenvectors ϕ_s and $\mathbf{\Lambda}$ the diagonal matrix containing the corresponding c eigenvalues λ_s that represent the variance of each mode of variation.

The eigenvectors were sorted according to their corresponding eigenvalues in descending order. Each training shape can now be described by adding the contributions of the c eigenvectors to the average shape:

$$\mathbf{x} = \bar{\mathbf{x}} + \sum_{s=1}^c b_s \phi_s \quad (5)$$

with eigenvectors ϕ_s representing the main modes of variation (also termed principal components or PCs) and b_s the shape model parameters or PC scores describing the contribution of the s^{th} mode of variation. New shapes can also be generated using the same equation. The shape model parameters are restricted to be within the following range:

$$-3\sqrt{\lambda_s} \leq b_s \leq 3\sqrt{\lambda_s} \quad (6)$$

with $\sqrt{\lambda_s}$ the standard deviation. This range is determined by assuming the data follows a normal distribution.

To determine c , the number of modes to retain, the ratio r of the accumulated variance to the total variance in the model was calculated using:

$$r = \frac{\sum_{s=1}^c \lambda_s}{\sum_{s=1}^{N-1} \lambda_s} \quad (7)$$

The threshold for r was set to 0.9 which is a generally accepted value for this ratio [37], [54].

PCA was performed using the implementation from the `scikit learn`¹⁰ library in python. PCA results were analysed by generating two shapes for each mode of variation separately, using the extreme values of the shape mode restrictions, *i.e.*:

$$\mathbf{x}_s^+ = \bar{\mathbf{x}} + b_s^+ \phi_s \quad (8)$$

$$\mathbf{x}_s^- = \bar{\mathbf{x}} + b_s^- \phi_s \quad (9)$$

with $b_s^+ = 3\sqrt{\lambda_s}$ and $b_s^- = -3\sqrt{\lambda_s}$

2.1.2 Multilinear regression model building

Multilinear regression models were developed to correlate the shape model parameters b_s with patient characteristics. These patient characteristics included gender, age, height, and weight.

Multilinear regression models are based on the assumption that there is a linear relationship between the explanatory variables (patient characteristics) and the dependent variables (shape model parameters b_s). Additionally, problems might arise if the explanatory variables are highly correlated with each other. This might affect the model coefficients and p -values since it becomes more difficult to estimate the relationship between each explanatory variable and the dependent variable *independently* because these explanatory variables change in unison. To test these assumptions and to check whether multilinear regression models are suitable to use, correlations between the variables of the training subjects were first studied as well as the variance inflation factors.

2.1.2.1 Pre-processing

The categorical variable gender was converted to a 0/1 (0= female; 1=male) encoding to be used in the regression models. All independent variables were standardized (*i.e.*, centred and normalized to have a unit variance) except for gender. This was done since the centring of variables reduces multicollinearity [55]. Additionally, normalization allows for a more straightforward interpretation of the regression coefficients.

2.1.2.2 Training

Next, separate multilinear regression models were trained to predict each of the shape model parameters using the patient characteristics as explanatory variables. Standard multilinear regression models were used, *i.e.*:

$$b_s = w_{s0} + w_{s1} \cdot \text{Gender} + w_{s2} \cdot \text{Age} + w_{s3} \cdot \text{Weight} + w_{s4} \cdot \text{Height} \quad (10)$$

¹⁰ <https://scikit-learn.org/stable/modules/generated/sklearn.decomposition.PCA.html>

The models were trained in python using the `statsmodels`¹¹ library (version 0.13.2). The final regression coefficients (*i.e.*, $w_{s0} \dots w_{s4}$) were extracted.

2.1.2.3 Assessment & validation

R^2 values were used to check how much variation of the shape model parameters was explained by the independent variables in the regression models. The F -statistic probabilities (p -values) were extracted to assess the models' significance. p -values considering the t -statistic were studied for each coefficient in each regression model to assess how probable each coefficient is.

2.1.3 SSM-to-patient fitting using patient characteristics & orthogonal X-rays

In a second step, a semi-automated SSM fitting algorithm was developed to be able to create a personalized 3D bone shape for a given unseen, fractured patient. This was achieved using patient characteristics and two 2D orthogonal X-ray images of the fractured bone as inputs.

Different methods for patient-specific 3D reconstruction from 2D X-ray images (2D/3D reconstruction) have been previously developed. Reyneke *et al* (2019) [80] reviewed the state-of-the-art in 2D/3D reconstruction. There are two main strategies to achieve the reconstruction. The first class relies on the establishment of correspondences (feature matching) and minimization of the geometric distance between features detected on the (projected) SSM realization and X-ray images by optimizing the shape parameters of the SSM [81]. Most recent studies employ a second strategy which relies on a statistical shape and appearance model (SSAM), which is a voxelized extension of an SSM where intensity values are also present in the model [61]. Simulated X-ray images or digitally reconstructed radiographs (DRRs) can then be obtained using ray-casting [81]. Next, the shape and appearance parameters are optimized such that the score of a similarity measure which compares the pixel intensities of the DRRs and X-rays is maximized [80]. Since the shape model developed in this research does not include intensity values, only the first strategy is suitable.

The developed SSM-to-patient fitting algorithm consisted of three main sub-steps which are depicted in **Figure 8**. First, the 3D shape was initialized using the multilinear regression models correlating patient characteristics with the shape parameter values of the SSM training shapes. Next, the initialized shape was morphed along the principal components to fit two orthogonal X-rays of the fractured tibia. This was done by iteratively optimizing the shape parameters such that projections of the SSM realization had the same bounding box dimensions as measured on the (pre-processed) X-rays of the patient. After that, the shape parameters were further iteratively refined such that the distances between the contours of the projections of the SSM realization and the contours of the X-rays of the patient were minimal.

¹¹ <https://www.statsmodels.org/stable/index.html>

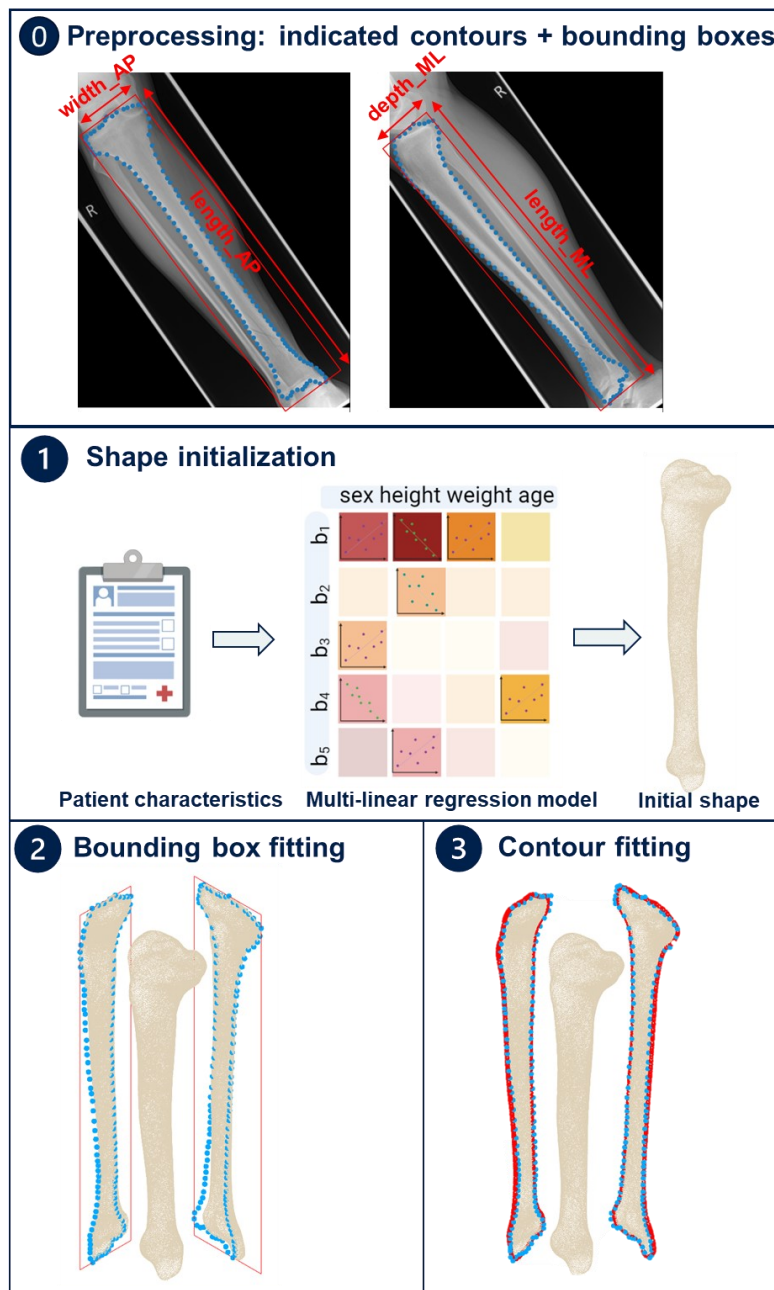


Figure 8: Overview of the main steps of the SSM-to-patient fitting algorithm. Blue dots (0,2,3): indicated contour points on the X-rays of the given patient, Red boxes (0,2): automatically computed bounding boxes using the indicated contour points of the given patient (0) and projections of the SSM realization (2) respectively, Red contours (3): automatically computed contours of the projections of the SSM realization. *Note:* X-rays are from the test case of the patient with a spiral diaphyseal tibial fracture.

The taken steps are detailed in the following sections and were implemented in python, mainly relying on the libraries `pydicom`¹², `Open3D`¹³, `numpy`¹⁴, `scipy`¹⁵ and `concavehull`¹⁶.

¹² <https://pydicom.github.io/>

¹³ <http://www.open3d.org/>

¹⁴ <https://numpy.org/>

¹⁵ <https://scipy.org/>

¹⁶ <https://github.com/senhorsolar/concavehull>

2.1.3.1 Assessment & validation

To test the accuracy of the SSM-to-patient fitting algorithm, *i.e.*, its ability to predict the tibia geometry of a previously unseen patient, two cases were used.

A test case of the patient with a spiral diaphyseal tibial fracture was used to assess whether the algorithm is able to predict the intact 3D geometry of a non-displaced (or reduced) fractured tibia based on patient characteristics and X-rays. The characteristics of this patient are summarized in the first row of **Table 1** (*i.e.*, case “FRACTURED”). The pre-operative and post-operative X-rays of this patient are shown in **Figure 9**.

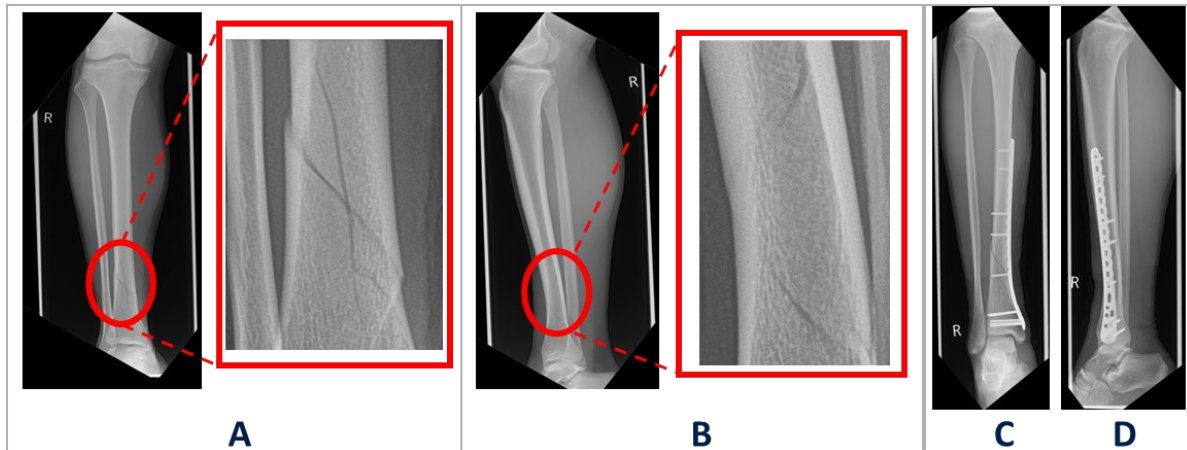


Figure 9: Preoperative (A-B) and postoperative (C-D) X-rays of the fractured tibia patient case used to test the success of the workflow. A: frontal view; preoperative, B: lateral view; preoperative, C: frontal view; postoperative, D: lateral view; postoperative.

The performance of the fitting algorithm on this patient case was assessed by: (1) computing the differences in bounding box dimensions of the true and projected reconstructed bone after bounding box fitting and (2) computing the Hausdorff distances between the patient X-ray contours and the contours of the projected reconstructed bone after contour fitting. However, the true 3D shape of the test case was not known since CT scans for this test case were not available.

Therefore, the performance of the developed algorithm was further assessed by reconstructing the 3D shape of an intact segmented 3D tibia bone, that was not included in the SSM nor the regression models. The CT scan for this validation case was collected from the New Mexico Decadent Image Database [39] and the right tibia was segmented according to the segmentation methods outlined in section 2.1.1.2. The patient characteristics of this validation case are summarized in the second row of **Table 1** (*i.e.*, case “INTACT”).

The shape parameters were initialized using the developed regression models and a 3D shape was reconstructed using the SSM and equation (5). The reconstructed shape was compared to the true segmented 3D shape by computing the Hausdorff distances. These Hausdorff

distances were compared with the Hausdorff distances between the mean shape and the true shape to demonstrate the added value of the regression models. Subsequently, the other fitting steps (*i.e.*, bounding box fitting and contour fitting) were performed. Because no X-rays of this case were available, DRRs were first generated using 3D Slicer (see *Appendix C*). The obtained DRRs of this validation case are shown in **Figure 10**. Bounding box fitting and contour fitting were performed based on these DRRs and the final reconstructed 3D shape was compared to the true segmented 3D shape by computing the Hausdorff distances.



Figure 10: Digitally reconstructed radiographs (DRRs) generated using the computed tomography (CT) scans of the intact validation case.

Table 1: Characteristics of the cases used to test the success of the workflow.

Case	Gender	Age [years]	Weight [kg]	Height [cm]	Fracture type	Fixation
FRACTURED	Male	22	86	184	42A1, non-displaced, right	Locking Compression Plate Low Bend Medial Distal Tibia Plate 3.5 mm (239 mm), DePuy Synthes, Zichwil, Switzerland) ¹⁷
INTACT	Female	44	110	170	-	-

2.1.3.2 Pre-processing: patient X-rays

Contours of the tibiae were obtained by manual indication on two orthogonal patient X-rays acquired in anteroposterior (AP) and mediolateral (ML) views. **Figure 11** shows the manually indicated contours for the fractured patient case. Contours obtained for the intact validation case can be found in *Appendix C*. Contour extraction was achieved through a custom-made script in python that loads the Digital Imaging and Communications in Medicine (DICOM) images and requires the user to manually click on points that are part of the bone contours (see **Figure 11**). Special attention had to be given to the contours around the epiphyses; the most outer contours were indicated since these were also extracted from the projected SSM realizations in subsequent steps. The coordinates of the clicked points were extracted and

¹⁷

http://synthes.vo.llnwd.net/o16/LLNWMB8/INT%20Mobile/Synthes%20International/Product%20Support%20Material/legacy_Synthes_PDF/DSEM-TRM-1115-0544-2_LR.pdf

scaled to the physical coordinate system of the image plane using the *PixelSpacing* attribute¹⁸ specified in the DICOM.

The length, width, corner points, and centre of the bounding boxes of extracted contours were automatically computed by PCA of the contour points.

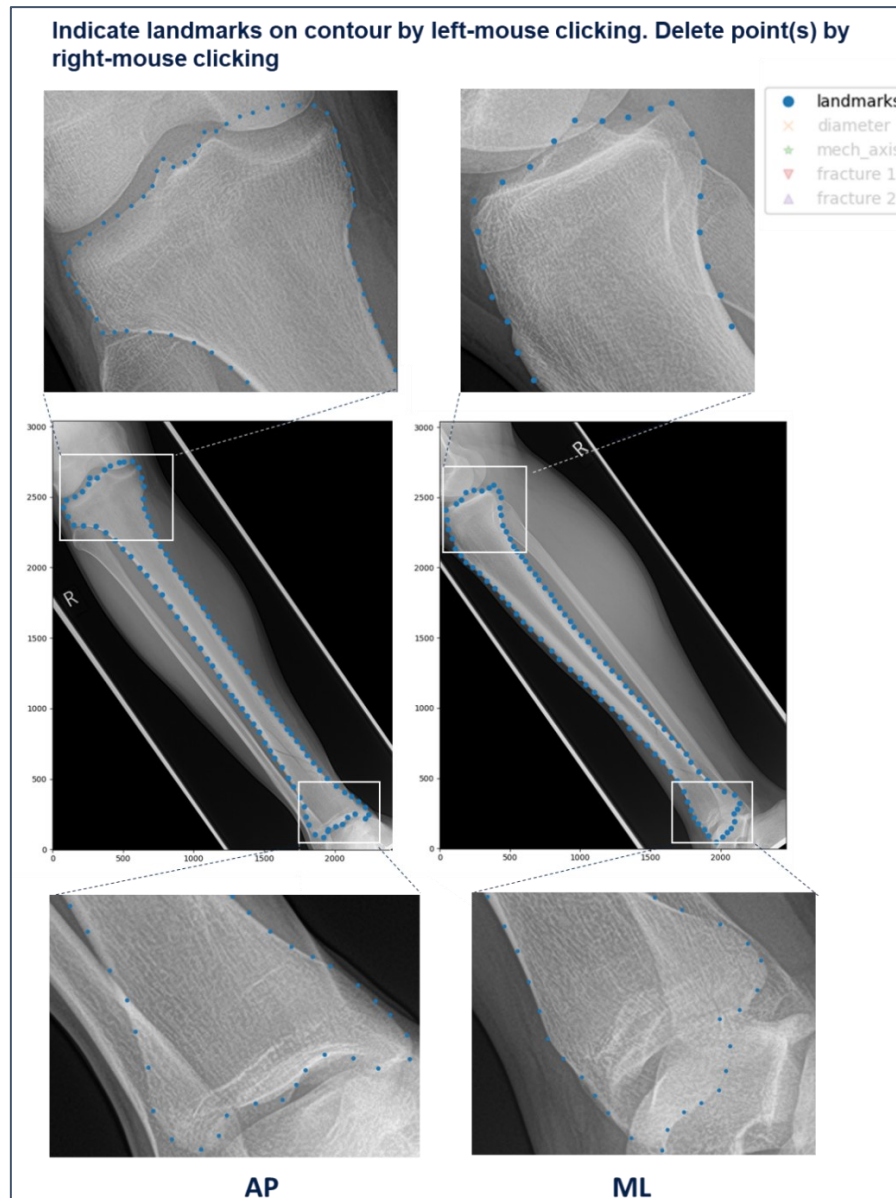


Figure 11: Custom-made GUI that requires the user to indicate the contour points on the AP and ML X-rays. AP: anteroposterior, ML: mediolateral. *Note:* X-rays are from the test case of the patient with a spiral diaphyseal tibial fracture.

¹⁸ <https://dicom.innolitics.com/ciods/rt-dose/image-plane/00280030>

2.1.3.3 Pre-processing: SSM realizations

2.1.3.3.1 Coordinate system

To avoid misalignment between different tibia shapes (*i.e.*, different realizations of the 3D SSM and its projections), a reliable repeatable coordinate system was mathematically defined first. The principal axes of the 3D tibiae were computed using oriented bounding boxes (based on PCA of the convex hull of the shape¹⁹). The first principal axis was aligned with the positive z-axis, such that the positive z-direction points from inferior to superior. For left and right tibiae, the x-axis was aligned with the second principal axis, such that the positive x-direction points from lateral to medial. Finally, the last principal axis was aligned with the positive y-axis, such that the positive y-axis points from anterior to posterior. Subsequently, the shapes were translated such that the most anterior, lateral, and inferior corner points of the bounding boxes of the 2D projections of the shapes coincided with the centre of the coordinate system (see **Figure 12**).

2.1.3.3.2 2D projections of SSM realizations

To perform the SSM-to-patient fitting, 2D projections of the 3D SSM realizations were made in each iteration of the fitting algorithm. The assumed projection setup is depicted in **Figure 13** and was based on reported radiographic positioning of the tibia in clinical practice (see **Figure 14**) [56], [57]. The focal spot size of the X-ray source (*i.e.*, the origin of the X-rays used to produce the radiograph) was assumed to be infinitely small (*i.e.*, a pinhole). The distance between the X-ray source and the detector (source-detector distance) was assumed to be 100 cm as is standard in X-ray imaging of the tibia [56]. An initial educated guess for the distance between the centroid of the tibia and the imager (object-imager distance, see **Figure 13**) in anteroposterior view was set to 9 cm for the test case, considering the usual position of the tibia in an X-ray set-up and a typical thickness of the calf (see **Figure 14**). The object-imager distance in mediolateral view was computed using the ratio of the measured bone lengths from the two X-rays (see *Appendix B* for details).

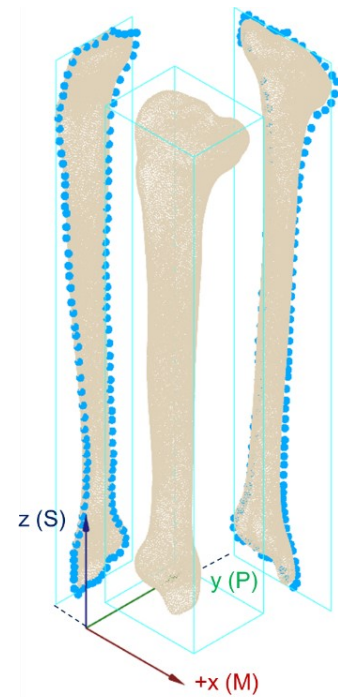


Figure 12: Definition of the repeatable coordinate system with respect to the 3D tibia instance and its projections. x-axis = 2nd principal axis. y-axis = 3rd principal axis. z-axis = 1st principal axis. Origin: most inferior, lateral, anterior point of the 2D projections of the 3D shape.

¹⁹ http://www.open3d.org/docs/latest/python_api/open3d.geometry.OrientedBoundingBox.html

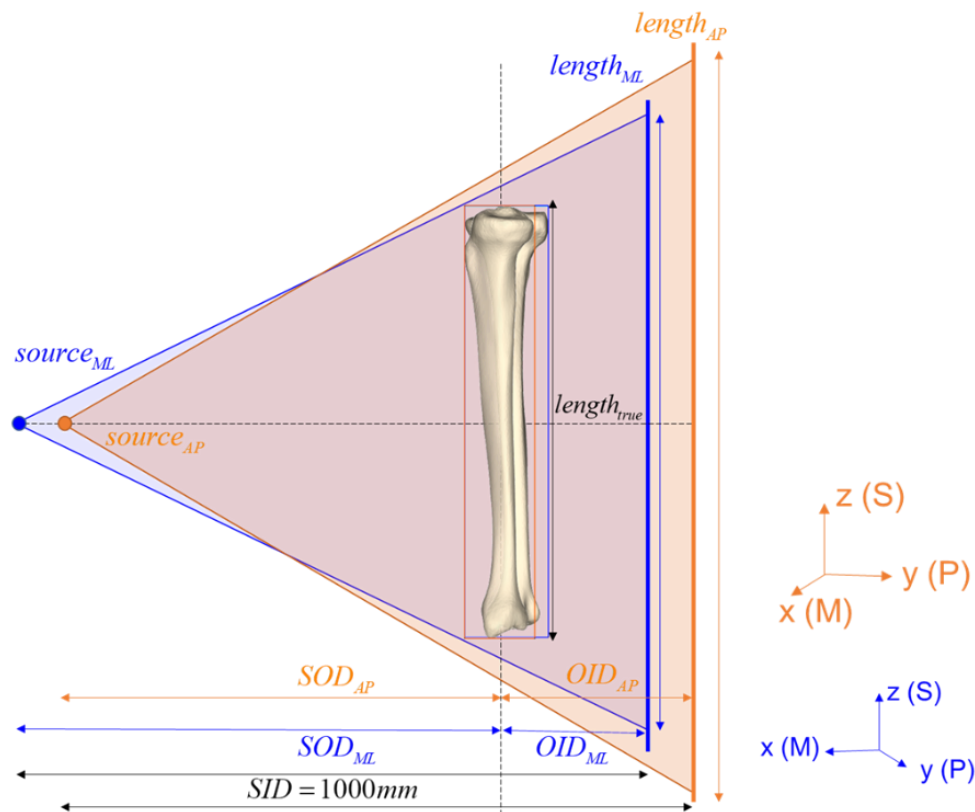


Figure 13: Assumed X-ray projection setup for anteroposterior (AP) in orange and mediolateral (ML) projections in blue. SOD: source-object-distance, OID: object-imager-distance, SID: source-imager-distance, S: superior, P: posterior, M: medial.

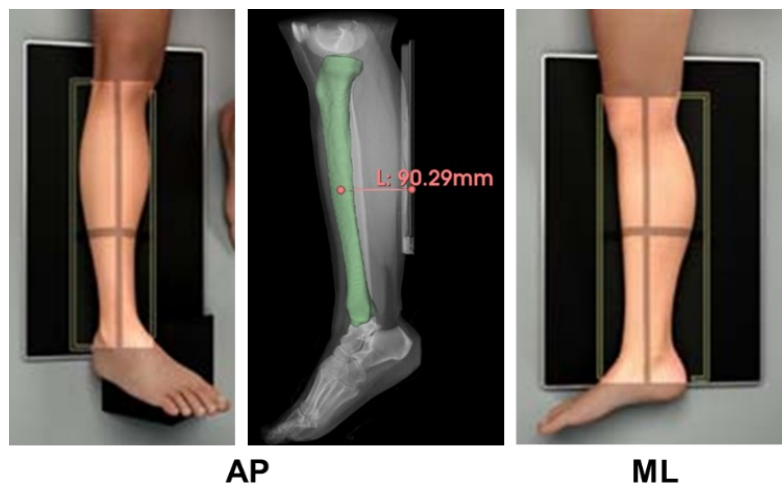


Figure 14: Positioning of the leg for tibia anteroposterior (AP) and mediolateral (ML) X-ray imaging of the tibia in clinical practice. *Notes:* the pictures on the left and right are adapted from [57] and the picture in the middle was generated using the CT scan and tibia segmentation of the intact validation case.

Planar projections of the 3D SSM shape realization (*i.e.*, point cloud) onto anteroposterior and mediolateral planes were established using the perspective transform of a set of points as depicted in **Figure 15**. Equations were adapted from Pyakurel (2020) [58] and can be found in *Appendix B*.

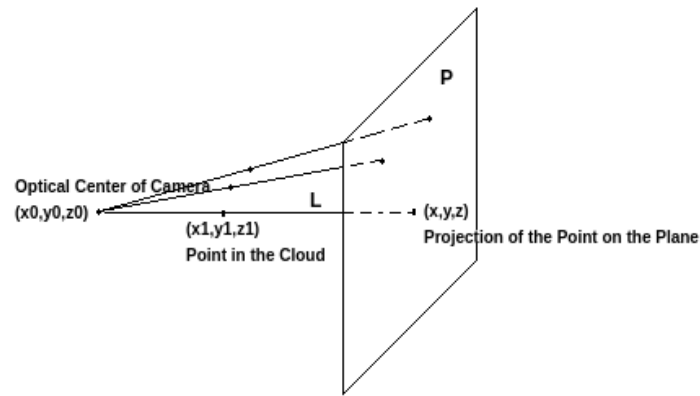


Figure 15: Projection of a point in a point cloud onto a plane. *Note:* From [58]

2.1.3.3.3 Contour extraction from 2D projections SSM realization

To automatically extract the contours of the 2D projections of the SSM realizations in each iteration, concave hulls were automatically computed. The concave hull of a geometry is a concave polygon that encloses the vertices of the input geometry. For the computation of concave hulls enclosing the 2D SSM projections, the `concavehull` library²⁰ in python was used with a chi factor of 0.01. This library uses an implementation of a paper by Duckham *et al* (2008) [59].

2.1.3.4 SSM-to-patient fitting algorithm

Using the pre-processing steps as described in the sections above, the SSM-to-patient fitting algorithm included the following steps (see **Figure 8**). More details on the used equations can be found in *Appendix B*.

1. Initialization of the shape parameters b_s using the multilinear regression models described in the previous section (see section 2.1.2).
2. Optimize shape parameters b_s such that anteroposterior and mediolateral projections of the SSM realization have equal bounding box dimensions as anteroposterior and mediolateral patient X-ray contours. To achieve this, the following steps were performed in each iteration:
 - a. Position SSM realization in a repeatable coordinate system as depicted in **Figure 12** with neutral pose in X-ray setup as depicted in **Figure 13**,
 - b. Project SSM realization in anteroposterior and mediolateral planes,
 - c. Compute bounding box dimensions of anteroposterior and mediolateral projections using PCA,
 - d. Minimize the difference in the bounding box dimensions of the projected SSM realizations and the X-ray images.
3. Refine shape parameters b_s and pose \mathbf{T} (*i.e.*, position in the X-ray setup) such that the distances between the concave hulls of anteroposterior and mediolateral projections of the transformed SSM realization and the anteroposterior and mediolateral X-ray

²⁰ <https://github.com/senhorsolar/concavehull>

contours are minimal. To achieve this, the following steps were performed in each iteration:

- a. Position SSM realization in the repeatable coordinate system as depicted in **Figure 12** with pose \mathbf{T} in the X-ray setup as depicted in **Figure 13**,
- b. Project SSM realization in the anteroposterior and mediolateral planes,
- c. Compute the concave hull points of the anteroposterior and mediolateral projections of the transformed SSM projections,
- d. Optimize b_s and \mathbf{T} such that the root-mean-square of Euclidian distances between the anteroposterior and mediolateral concave hull points and the anteroposterior and mediolateral X-ray contour points is minimized.

Optimization was performed using Powell optimizers from the `scipy` library²¹ in python. Bounds were defined as $-3\sqrt{\lambda_s} \leq b_s \leq 3\sqrt{\lambda_s}$ and default settings were used for convergence conditions, the number of iterations and function evaluations (*i.e.*, 'xtol': 0.0001, 'ftol': 0.0001, 'maxiter': None, 'maxfev': None).

2.2 Step 2: Development of a patient-specific fractured 3D tibia model based on the intact 3D bone shape and orthogonal X-rays

As part of **objective 2** of this study, a methodology was developed to automatically introduce the patient-specific fracture lines as detected on two orthogonal patient X-rays into the intact 3D bone shape. For this purpose, a method was first developed to obtain the approximate 3D fracture line coordinates from the 2D X-rays, which were introduced into the 3D intact shape in a next step. The fracture line coordinates were obtained by manual indication on the patient's frontal X-ray. These projected fracture line coordinates were then back-projected to the coordinate system of the intact 3D tibia bone (from **Figure 12**). They were introduced into the intact 3D tibia bone of the previous step by polyhedron cropping. The fracture fragments were post-processed and a callus geometry was created to surround the fracture region. These steps were taken for the test case of the patient with a spiral diaphyseal tibial fracture. An overview of these steps is shown in **Figure 16** and the steps will be detailed in the following sections.

²¹ <https://docs.scipy.org/doc/scipy/reference/optimize.minimize-powell.html#optimize-minimize-powell>

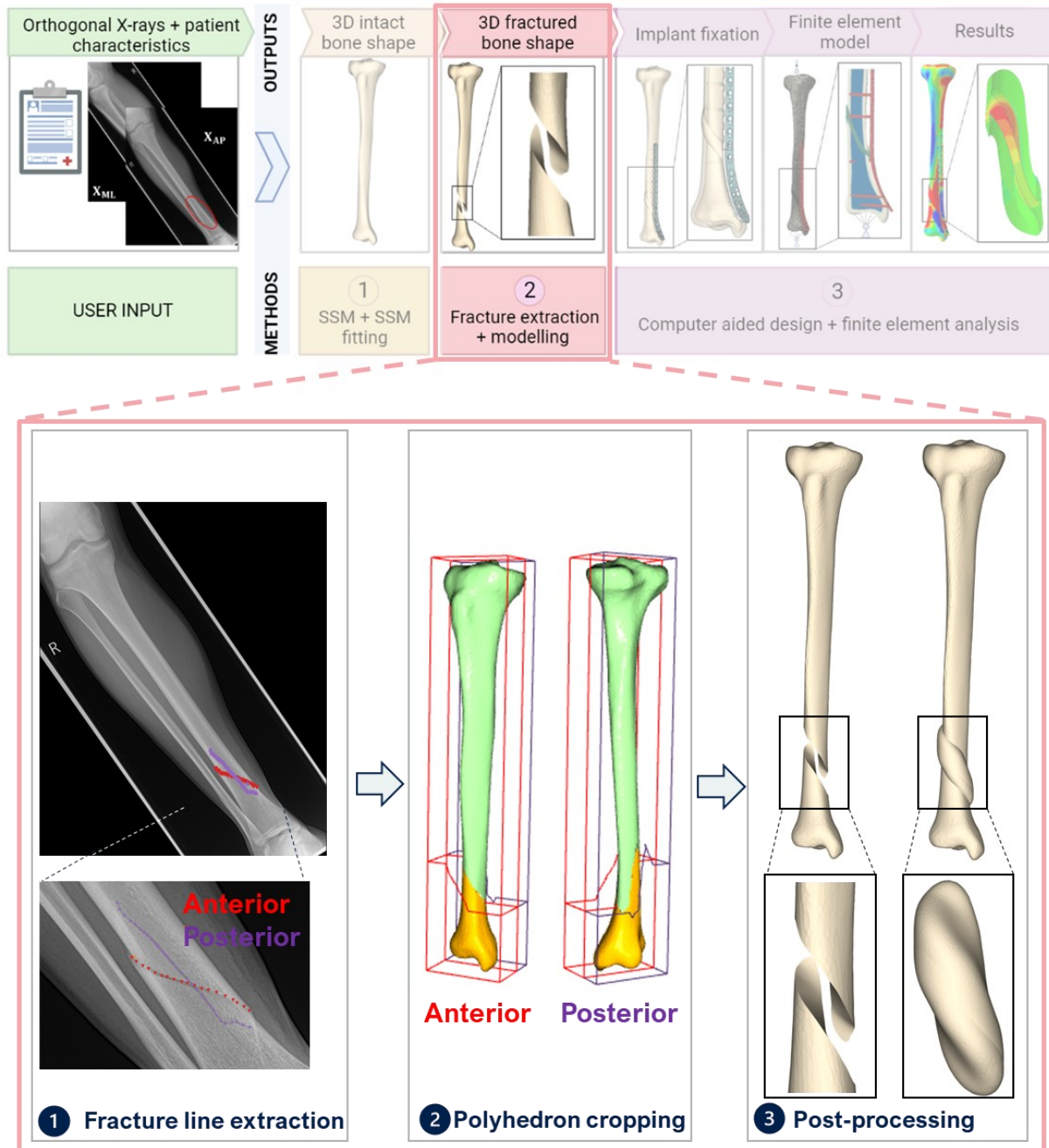


Figure 16: Overview of steps taken to achieve fracture line extraction from X-rays and modelling of the fracture lines into the intact 3D bone shape. *Note:* X-rays are from the test case of the patient with a spiral diaphyseal tibial fracture.

2.2.1 Extracting approximate 3D fracture line coordinates using orthogonal X-rays

Fracture lines were obtained from the frontal X-ray by manual indication in a similar manner as the retrieval of the contours in section 2.1.3.2, *i.e.*, by requiring the user to manually click on points that are part of the fracture lines (see **Figure 17**). Only the frontal X-ray was used to introduce the fracture into the intact 3D model since the lateral X-ray added very limited additional information regarding the fracture line (see **Figure 9** and **Figure 17**). Additionally, two points representing the outer edges of the tibial diaphysis at the level of the fracture were also indicated on both the frontal and lateral X-rays.

Similarly to the processing of the X-ray contour coordinates, the coordinates of the clicked fracture and diameter points were extracted and scaled to the physical coordinate system of the image plane using the *PixelSpacing* attribute²² specified in the DICOM.

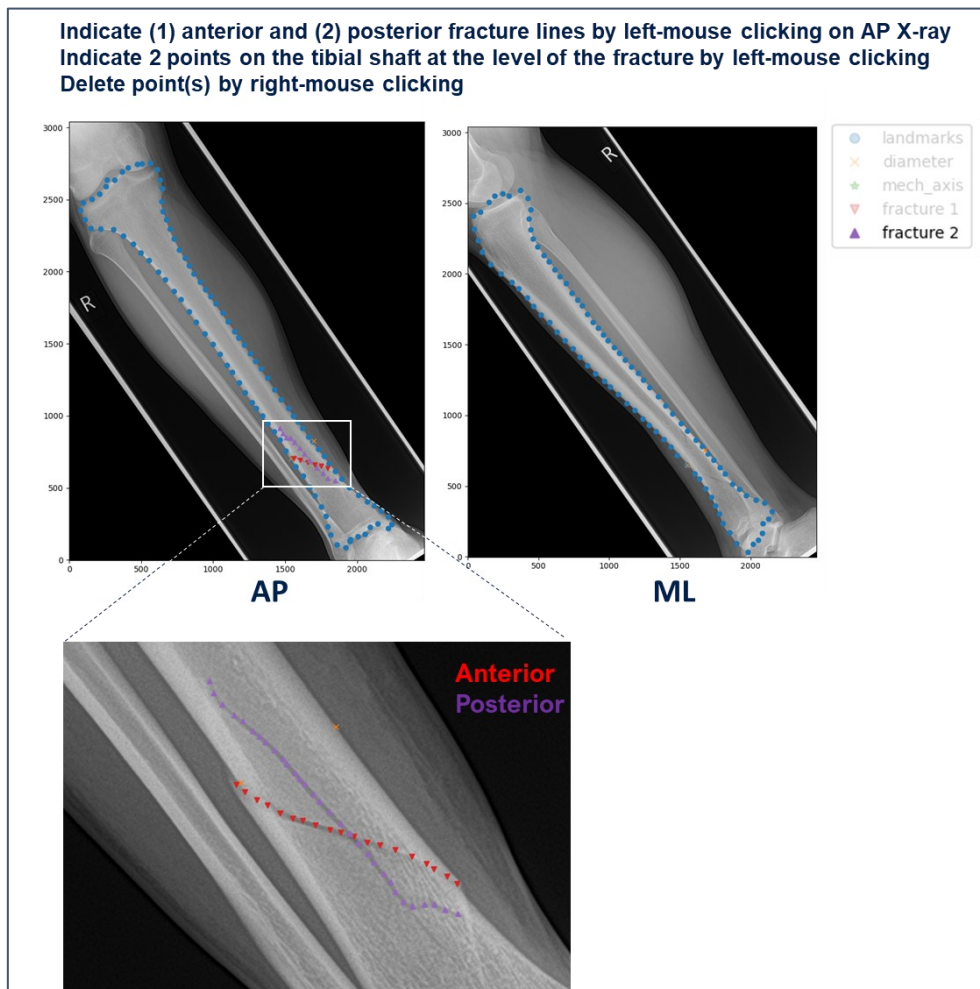


Figure 17: Custom-made GUI that requires the user to indicate the fracture line points on the AP X-ray and the shaft diameter on AP and ML X-rays. AP: anteroposterior, ML: mediolateral, fracture 1 (red): anterior fracture line, fracture 2 (purple): posterior fracture line, diameter (orange x): two points representing the outer edges of the tibial diaphysis at the level of the fracture. *Note:* X-rays are from the test case of the patient with a spiral diaphyseal tibial fracture.

2.2.2 Modelling the 3D fracture lines in the intact tibia model

2.2.2.1 Back-projection

To be able to introduce the obtained fracture lines into the intact tibia model, they were first transformed to the coordinate system of the anteroposterior and mediolateral SSM projections (x and z for anteroposterior, y and z for mediolateral) as depicted in **Figure 12**. Details on the computation of the required transformations can be found in *Appendix B*. Next, the projected anterior and posterior fracture line coordinates were back-projected to their unprojected

²² <https://dicom.innolitics.com/ciods/rt-dose/image-plane/00280030>

position in 3D space. This was done using inverse projection geometry as detailed in *Appendix B*.

2.2.2.2 Polyhedron construction & cropping

Using the back-projected fracture line coordinates and the bounding box of the intact 3D bone shape, polyhedrons were automatically constructed that were used to crop the intact 3D bone shape into two fracture fragments. The constructed polyhedrons for the test case are shown in **Figure 18**. The anterior fracture line was used to crop the point cloud until halfway across the tibia shaft at the level of the fracture in the y-direction, while the posterior fracture line was used for the posterior half. Details on the used equations can be found in *Appendix B*.

2.2.2.3 Postprocessing bone fragment geometry

The bone fracture fragments were exported as STL files in their original position in the coordinate system shown in **Figure 12** (by inversely transforming with transformation \mathbf{T}^{-1}). Additionally, the unclipped intact 3D bone shape was exported as an STL file in the same coordinate system.

Next, the bone fracture fragments were post-processed in Autodesk Meshmixer²³ (Version 3.5.474, Autodesk, Inc., California, USA). The fracture lines were smoothed to prevent meshing issues in a later stage (see **Figure 19**). Additionally, the fracture fragment meshes were closed, since the clipping in the previous step creates a hole in the mesh (see **Figure 19**). Additionally, the inner cortical bone surface was artificially created since only the cortical outer surface of the bone was reconstructed using the SSM. In line with the work from Macleod (2014) [60], a uni-cortical thickness of 5 mm was considered for a healthy tibia. The inner cortical bone surface was reconstructed by offsetting the outer cortical bone surface of the tibia by -5 mm in the direction normal to the bone surface (see **Figure 20**). All the interior bone space embedded within the cortical bone was assumed to be occupied by bone marrow. Furthermore, a callus geometry was created in Meshmixer, using a callus index of 1.15 in line with the work of Miramini *et al* (2016) [61] following the study of Horn *et al* (2011) [62] who measured the callus size of a group of patients with tibial fractures fixation with locking plates. The callus index is defined as the callus diameter divided by the bone diameter. The bone diameter of the test case was measured to be approximately 26 mm at the level of the fracture, so to create the callus, the bone surface around the fracture region was selected and extruded in all directions by

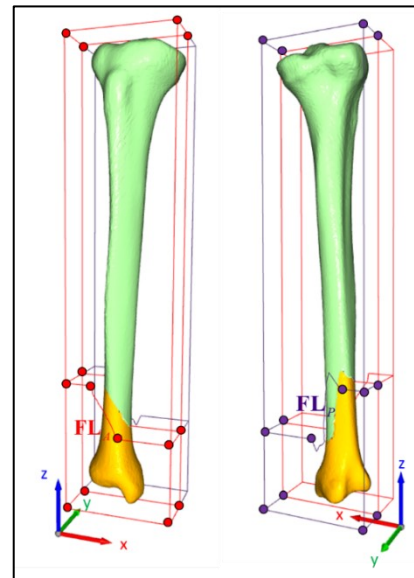


Figure 18: Constructed polyhedrons used to clip intact 3D bone shape into two bone fracture fragments. \mathbf{FL}_A : anterior fracture line, \mathbf{FL}_P : posterior fracture line.

²³ <https://meshmixer.com/>

2 mm in the direction normal to the surface (see **Figure 21**). The taken postprocessing steps in Meshmixer are detailed in *Appendix D*.

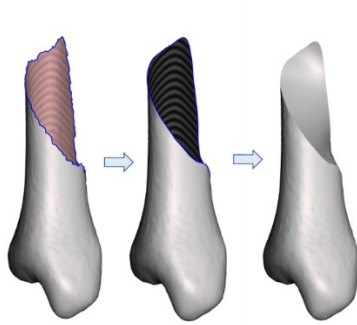


Figure 19: Postprocessing of the fracture fragment geometry - smoothing & closing.

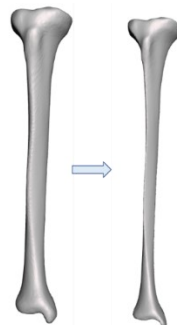


Figure 20: Reconstruction of the inner cortical bone surface: off-set outer cortical surface by -5 mm.



Figure 21: Reconstruction of the callus geometry: extrude surface around the fracture lines by 2 mm.

Finally, the STL files of the fracture fragments, the callus, and the reconstructed intact inner and outer cortical bone surfaces were imported into SOLIDWORKS (Student Edition 2022, Dassault Systèmes, France). The geometries were converted to 3D non-uniform rational B-spline (NURBS) representations, which are more efficient to assemble and easier to remesh [63]. Furthermore, a NURBS representation simplifies the introduction of defects and screw holes. Additionally, this representation allows for the extraction of the fracture surface as a B-spline surface. This is beneficial to be able to make the reconstructed fracture parametric (*e.g.*, changing the angle or height of the fracture surface), and to reconstruct a fracture gap with a uniform thickness. All bone geometries were assembled in SOLIDWORKS, and a uniform fracture gap of 4 mm was created using the extracted fracture surface. Boolean operations were used to create bone marrow and cortical bone fragment geometries. The taken steps are detailed in *Appendix E* and the final bone geometries are shown in **Figure 22**. All geometries were exported as solid part files (.SLDPRT).

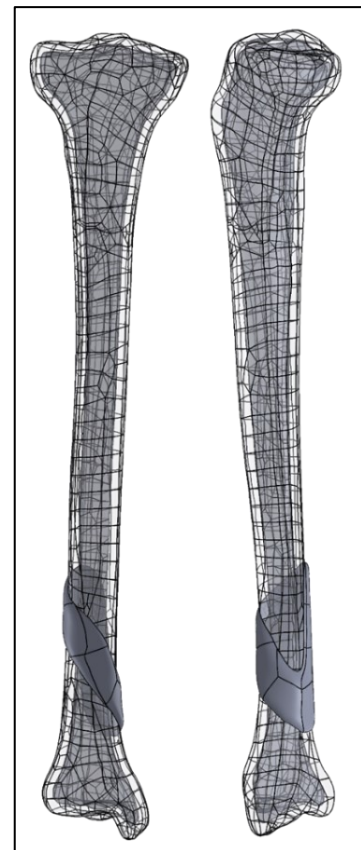


Figure 22: Cortical bone fragments, bone marrow and callus geometries after postprocessing in SOLIDWORKS. Left: frontal Right: lateral.

2.3 Step 3: FE analysis of the fixated fractured tibia

As part of **objective 3** of this study, FE models of the fixated fractured tibia were developed using the automatically created geometries from the previous steps (see **Figure 23**). For this purpose, fixated assemblies were first established in SOLIDWORKS. Next, FE models were built and analysed in Abaqus/CAE (version 2020,

ABAQUS Inc, Dassault Systèmes, France). These steps were taken for the test case of the patient with a spiral diaphyseal tibial fracture and are detailed in the sections below.

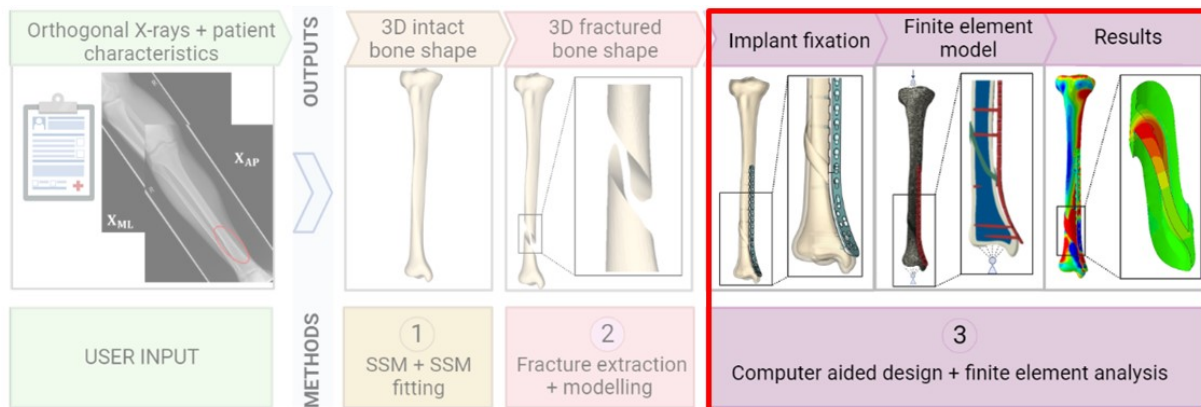


Figure 23: Step 3 of the workflow, *i.e.*, finite element (FE) analysis of the fixated fractured tibia.

2.3.1 Assembling bone fracture geometries & fixation device

The fracture gap of the test patient was stabilized with a stainless-steel right distal medial locking plate of 239 mm (LCP Low Bend Medial Distal Tibia Plates 3.5 mm, DePuy Synthes, Zichwil, Switzerland)²⁴ [64]. The implant geometry was drawn in SOLIDWORKS using computer-aided design (CAD) tools and a physical copy of the implant as a reference. The drawing was validated using a segmented micro-CT scan of the implant which became available in a later stage, by computing Hausdorff distances between the drawn and scanned plate (see *Appendix E*).

The locking screws that were used to fixate the plate had a shaft diameter of 3.5 mm and a head diameter of 5 mm. Screw lengths are available between 10–65 mm with a 5 mm increment. Simplified threadless screws were designed in SOLIDWORKS such that they fitted neatly within the plate in a fixed-angle construct as per the manufacturer’s guidelines (parallel to the x -axis, *i.e.*, the joint surfaces). This is imperative since the direction of the locking screws is determined based on the design of the plate [64].

All CAD parts were exported as solid parts (.SLDPRT) and imported into a new SOLIDWORKS assembly (.SLDASM). Plate placement was done in SOLIDWORKS according to the manufacturer’s recommended surgical technique, using the postoperative X-rays of the patient case as a reference. To achieve this, the head of the plate was centred on the medial malleolus, and the plate was translated and rotated until (limited) contact along the shaft was achieved. The simulated postoperative scenario is depicted in **Figure 24** and had a plate working length of 52 mm. Assemblies were exported as STEP files to be used for FE model construction.

²⁴

http://synthes.vo.llnwd.net/o16/LLNWMB8/INT%20Mobile/Synthes%20International/Product%20Support%20Material/legacy_Synthes_PDF/DSEM-TRM-1115-0544-2_LR.pdf

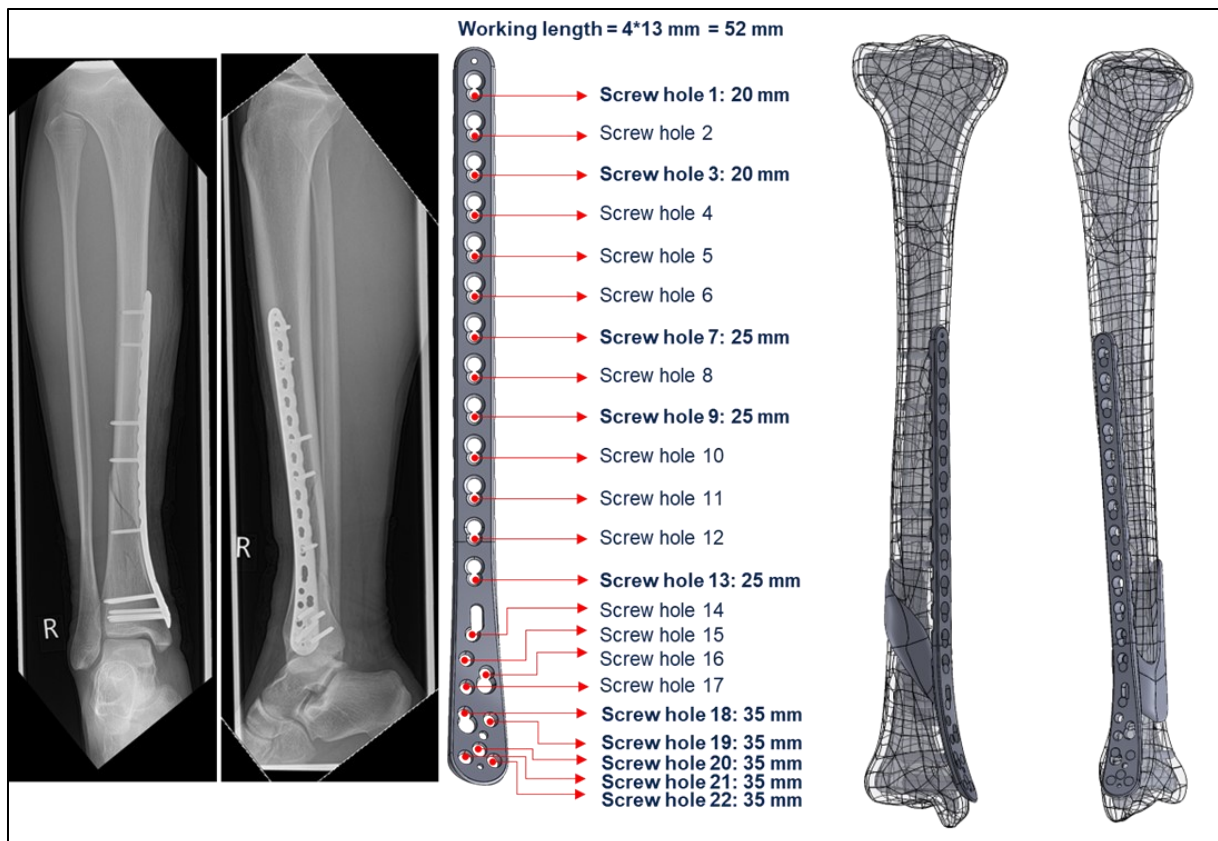


Figure 24: Assembly of the stabilized fracture of the test case of the patient with a spiral diaphyseal tibial fracture according to postoperative X-rays (scenario 1/5). Bold text: used screw holes.

2.3.1.1 Sensitivity analysis

Apart from the true clinical postoperative fixation scenario, four alternative fixation scenarios were simulated. It has been previously shown that the most important parameters to vary include the number and location of screws, the plate (working) length and plate and screw stiffness [60]. The screw orientation does not have a significant influence [65]. Therefore, four alternative configurations were considered which are depicted in **Figure 24** and **Figure 25**. In scenario 2, the 5th screw was moved from screw hole 13 to screw hole 14, leading to an increase in working length of 13 mm (new working length: 65 mm). In scenario 3, the 4th screw was moved from screw hole 9 to screw hole 8 leading to an additional increase in working length of 13 mm (new working length: 78 mm). In scenario 4, a shorter plate of 213 mm was used, while maintaining the original postoperative screw configuration. This shorter plate is also available in clinical practice. Lastly, a fixation scenario (scenario 5) with a magnesium plate rather than a stainless-steel plate was considered by manipulation of the material properties (see section 2.3.2.3). The true clinical postoperative screw configuration from **Figure 24** was considered for this scenario.

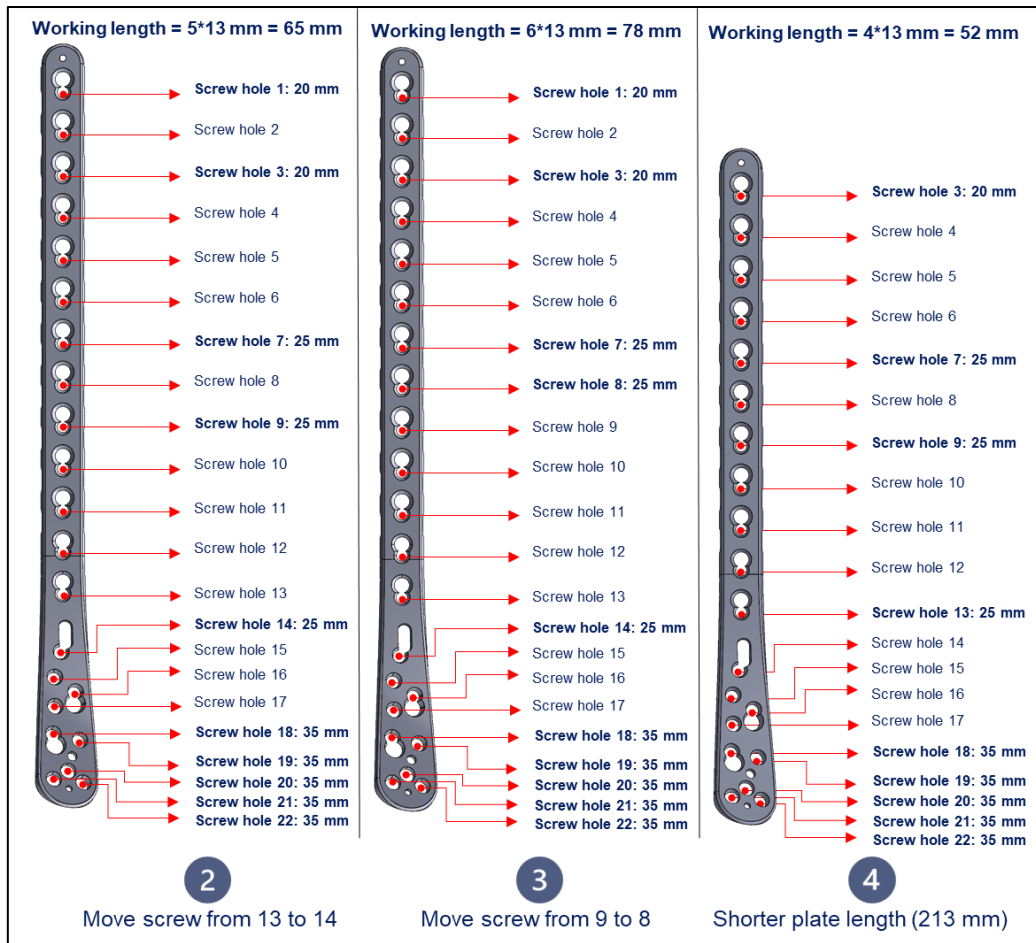


Figure 25: Alternative fixation scenarios considered for biomechanical analysis. Bold text: used screw holes.

2.3.2 FE model building & analysis

The FE models of the fractured tibia were built and analysed in Abaqus/CAE (version 2020, ABAQUS Inc, Dassault Systèmes, France). The model of the clinical postoperative scenario is shown in **Figure 26**. The steps taken to build the models are detailed in the sections below.

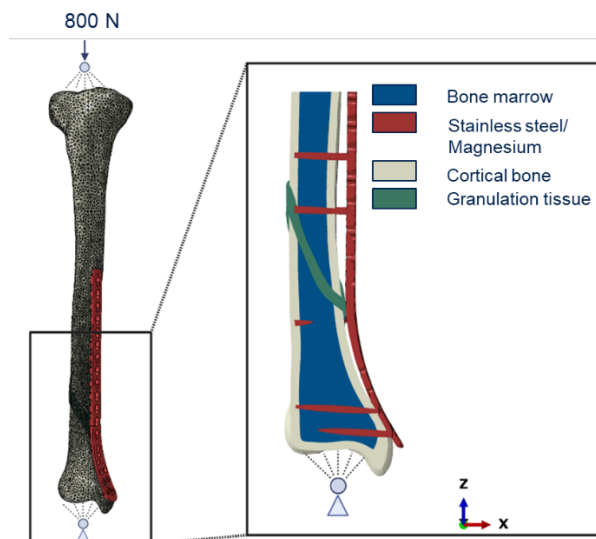


Figure 26: FE model of the fixated fractured tibia (scenario 1/5) including boundary conditions, loads and materials. Models of the other scenarios were equivalent.

2.3.2.1 Geometry + Assembly

The 3D assemblies (.STEP files) created in the section above (2.3.1) were imported in Abaqus/CAE. The International System of Units (SI Units) was adopted, *i.e.*, all distances and lengths are measured in millimetres, forces in Newton and stresses in N/mm² (*i.e.*, MPa). Since it concerns an asymmetrical geometry, no symmetry conditions were imposed. The coordinate system as depicted in **Figure 12** was used, *i.e.*, the x-axis running from lateral to medial, the y-axis from anterior to posterior and the z-axis from inferior to superior. The final geometry (for the true clinical postoperative scenario) is depicted in **Figure 26** and contains the plate, 10 screws, and upper and lower cortical fracture fragments filled with bone marrow with a fracture gap of 4 mm. A homogeneous callus with a callus index of 1.15 [61], [62] as described in section 2.2.2.3 was simulated. Similar to previous studies [60], [66], the fibula was ignored as it only transmits up to 6.4-16.7% of the load transmitted in the lower leg and is often fractured along with the tibia [67].

Geometries were all further processed and assembled in Abaqus/CAE using the steps detailed in *Appendix F*. The bone fragment and callus geometries were merged to form one single part consisting of different sections. This was done for two main reasons: (1) to establish compatible meshes between these parts and (2) to prevent having to use (relatively) computationally expensive tie constraints between these parts.

2.3.2.2 Meshing

The geometries were meshed in Abaqus/CAE using 10-node tetrahedral elements (C3D10). This type of element is most appropriate for complex curved geometries. Additionally, they can be used with adaptive mesh refinement which is convenient for establishing a fine mesh in the callus region (the region of interest) and a coarser mesh further away from the callus.

The meshing of the merged bone geometry was achieved using the Virtual Topology toolset in Abaqus combined with Face Partitioning. Edges in the callus region were seeded using an approximate element size of 1.5 mm. This mesh size was determined based on literature [60], [68], [69]. Proximal and distal edges far away from the callus region were seeded using an approximate element size of 5 mm. A smooth transition between the different regions was realized using biased seeding and the mesh was refined around the screw holes using an approximate edge length of 1 mm. The entire merged bone geometry was meshed with 528321 elements, with 80550, 265947 and 181824 elements for the callus, cortical bone and bone marrow respectively. The 239- and 213-mm locking plates were meshed with 118506 and 104771 elements respectively, using a global edge length of 0.9 mm. The screws were meshed with a total of 10468 elements using a global edge length of 1.5 mm. Mesh sizes of the screw holes, screws and plate were determined considering the applied tie constraints (see 2.3.2.4), which calls for a finer mesh grid spacing of slave surfaces as compared to master surfaces [70]. The number of elements and edge lengths used for each part are summarized in **Table 2** and the meshes for the different geometries are shown in **Figure 27**.

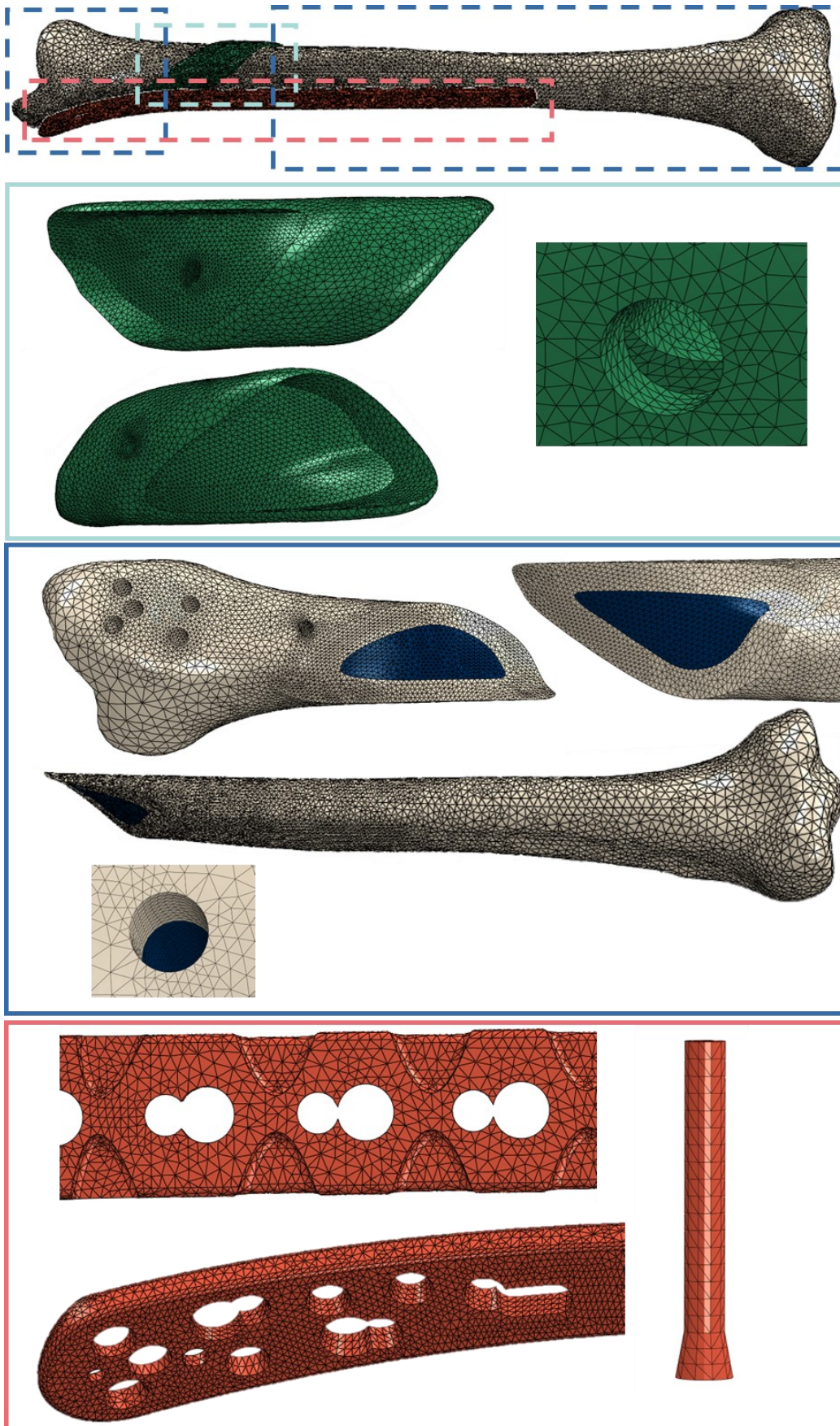


Figure 27: Meshes of the different geometries. Green: callus, Blue: bone fragments (white: cortical bone, blue: bone marrow, Red: locking plate and screws).

Table 2: Summary of the used number of elements and element sizes of each part.

PART	# ELEMENTS	EDGE LENGTH (mm)
Merged bone	528321	Varying
Callus	80550	+ - 1.5
Cortical bone	265947	1.5 - 5
Trabecular bone	181824	1.5 - 5
Plates		0.9
239 mm	118506	-
213 mm	104771	-
Screws	10468	1.5
20 mm (2x)	695 (2x)	-
25 mm (3x)	835 (3x)	-
35 mm (5x)	1228 (5x)	-

2.3.2.3 Materials

All materials were modelled using homogeneous, isotropic, linear elastic material models. Material properties were taken from the literature and can be found in **Table 3**. The callus was modelled as granulation tissue to simulate the early stages of bone healing [71]. Two different material properties were assigned to the osteosynthesis devices: the traditional stainless steel alloy 316L [64] and the biodegradable magnesium alloy WE43. WE43 has been previously proposed to be suitable for osteosynthesis thanks to its resorbability, biocompatibility, osteogenic properties, and favourable elastic modulus [72].

Table 3: Material properties assigned to the bone tissues and implants.

Part	Material	Elastic modulus (E) [MPa]	Poisson ratio (ν) [-]	Reference
Cortical bone fragments	Cortical bone	17000	0.3	[18][71]
Medullary cavity (cortical bone filling)	Bone marrow	2	0.167	[18][71]
Callus (until 6 th week)	Granulation tissue	0.2	0.167	[18][71]
Plate + screws (stainless steel)	Stainless steel (316L)	200.000	0.3	[73]
Plate + screws (magnesium)	Magnesium alloy (WE43)	44.200	0.27	[72]

2.3.2.4 Interactions/constraints

The connection between the different bone fragments and the callus was modelled as fully merged (see section 2.3.2.1) which is similar to applying a tie constraint [70]. The threadless screw shafts were tied to the screw hole surfaces within the bone. Locking screw connections with the plate were also modelled using tie constraints. The contact between the bone and the plate was not modelled since it was assumed that these parts never come into contact. The constraints and selected surfaces for the constraints are shown in **Figure 28**.

2.3.2.5 Boundary conditions

To prevent rigid body motions, the model degrees of freedom were constrained using boundary conditions. Joint rotations were implemented by constraining the articular surfaces of the tibia to single points in space considered to be the centres of the joints. This was done using coupling constraints. It was assumed that these joints act as pin supports that allow rotation, while translation is fixed in all directions. For the most superior articular surface (*i.e.*, the knee joint), translation was only fixed in the x and y directions, allowing translation in the axial z -direction. The applied boundary conditions and selected surfaces for these boundary conditions are shown in **Figure 28**.

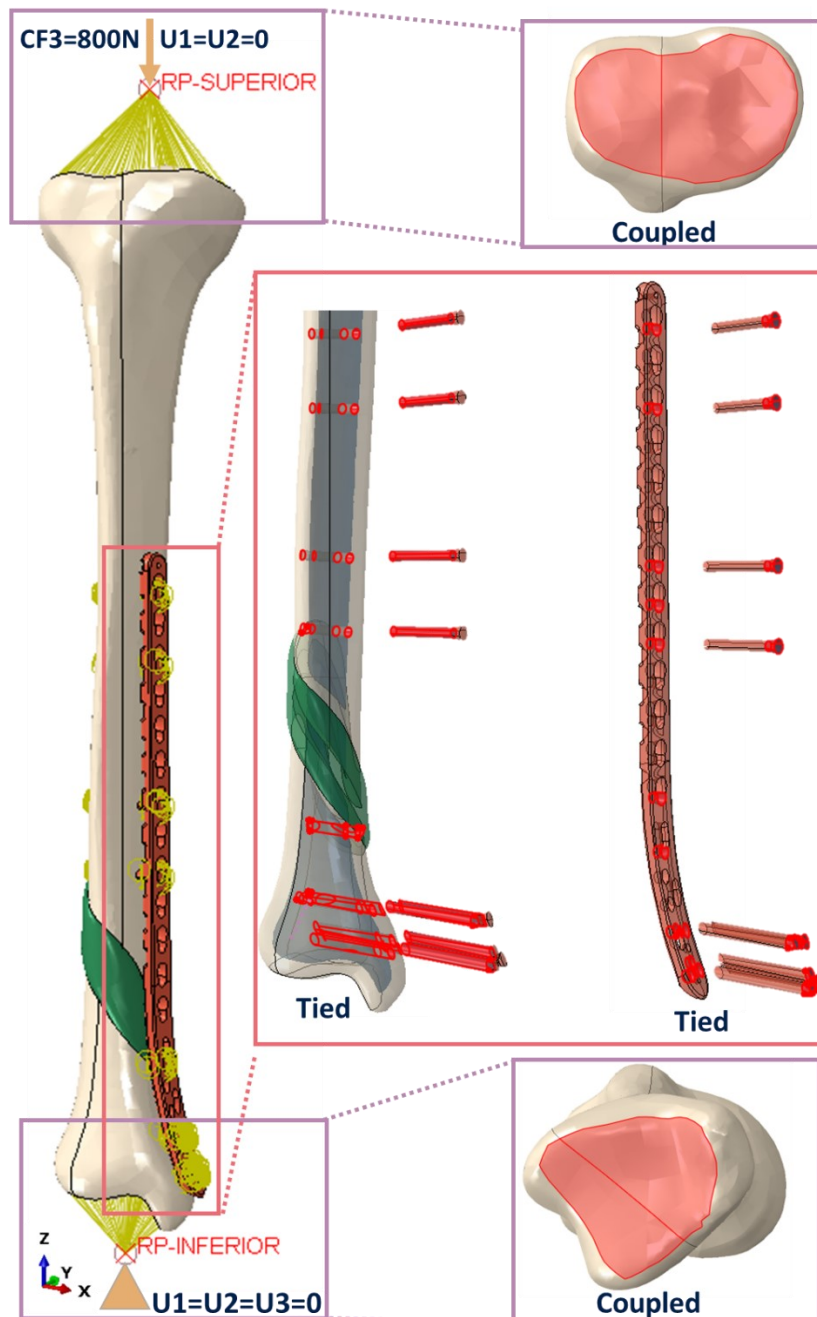


Figure 28: Applied constraints, boundary conditions and loads in the developed FE model(s). *Note:* Scenario 2 is depicted here, the other scenarios are equivalent. U: displacement, CF: concentrated force.

2.3.2.6 Loads

Loads acting on the tibia are primarily due to external loading by weight-bearing and muscle forces [22]. To the authors' knowledge, the physiological loading associated with daily activities of fractured human tibiae is not precisely known. However, tibia fractures are usually treated postoperatively with (partial) weight bearing until about 8 weeks after surgery [11], [15], [74]–[77]. Daily activities such as gait, which are associated with loads up to 470% of the body weight [22], [78], are not recommended in this phase. In the immediate postoperative period, it was therefore assumed that loads reach up to 100% of the body weight, based on different studies by *inter alia* Joslin *et al* (2008) [34] and Vijayakumar *et al* (2006) [75] that either measured or simulated tibial axial forces after tibial fractures.

For the patient test case, the FE simulation was therefore conducted with a resultant compression load of up to 800 N, considering the patient weight, ramped over 1 second. The load was applied as a concentrated force to a single reference point in space assumed to be the centre of the knee joint along the axial axis (see **Figure 28**). This axis corresponds to the anatomical axis of the tibia (see **Figure 3** in section 1.2.2.1) which is parallel to the mechanical axis in the frontal plane (but slightly angled in the sagittal plane). This direction was maintained throughout the analysis (it did not follow nodal rotation). This was done since the dominant loading direction during weight bearing on the tibia is axial [22] and the muscle forces generally also act axially [15].

2.3.2.7 Analysis step

A static, linear FE analysis was conducted. For the prescribed quasi-static boundary conditions and loads, solving for a static equilibrium is most suitable. Additionally, small deformations and deflections are to be expected based on the low-magnitude loading scenario and material properties. Therefore, a linear analysis was deemed appropriate. A standard explicit direct equation solver was used using Full Newton solution techniques, which is computationally the most efficient.

2.3.2.8 Post-processing

The analysis was conducted to determine the mechanical environment in the fracture zone, *i.e.*, within the callus region, since mechanical strains have been previously shown to influence healing outcomes (see section 1.2.1) [79]. Both the minimum and maximum principal strains within the callus were studied. Strains were quantified while excluding outliers²⁵. Furthermore, IFMs, *i.e.*, displacements of the fracture fragments, were studied since this outcome is often reported in *in vitro* and *in vivo* studies where it is not possible to directly assess tissue strains. IFMs were determined by defining three node pairs (medial, central, and lateral), where each pair contains one node on the proximal fragment and one on the distal fragment, in line with recommended reporting methods for mechanical testing of internal fixation devices [80]. The node pairs are shown in **Figure 29A**. Axial (local x) and shear (local

²⁵ Fences were used to cordon off outliers from the data. Upper fence = $Q2 + (1.5 * IQR)$
Lower fence = $Q1 - (1.5 * IQR)$. IQR: interquartile range, *i.e.*: $IQR = 75th (Q2) - 25th (Q1)$ percentile

y) displacements were assessed in local coordinate systems defined by the node pairs (*i.e.*, relative to the fracture lines) since this is most relevant for healing [61], [81]. Since the strains and displacements are expected to vary throughout the callus from the near cortex closest to the implant to the far cortex furthest from the implant [80], a path was created along this direction and used to quantify the strains along this path (see **Figure 29B**)

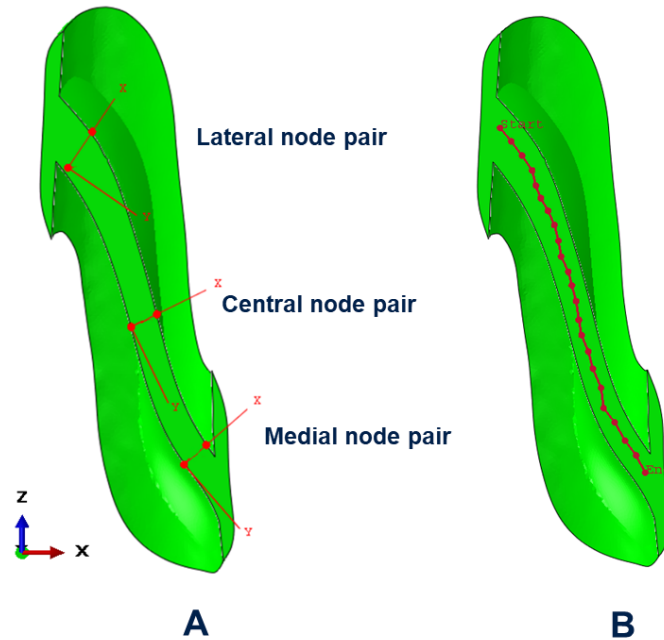


Figure 29: The defined node pairs, local coordinate systems and path used for post-processing of the finite element analysis. A: node-pairs and local coordinate systems. B: path. Constant y -coordinate in the global coordinate system ($y = 45$ mm).

3 RESULTS

In this chapter, results from the developed SSM, multilinear regression models, SSM-to-patient fitting methodology, and FE analyses are summarized.

3.1 Tibial SSM

A tibial SSM was built to be able to reconstruct patient-specific intact 3D tibia models. In this section, results from this SSM are discussed.

3.1.1 Training data acquisition

The final dataset used to build the SSM consisted of 25 individuals (15 male, mean age: 60 ± 5 ; 10 female, mean age: 52 ± 7). The univariate and multivariate distributions of their subject characteristics are depicted in **Figure 30** and **Figure 31**, respectively. Inspection of the multivariate distributions revealed a significant (Pearson) correlation between the height and age of the subjects (male: $r = .57$, $p < .05$; female: $r = .68$, $p < .05$).

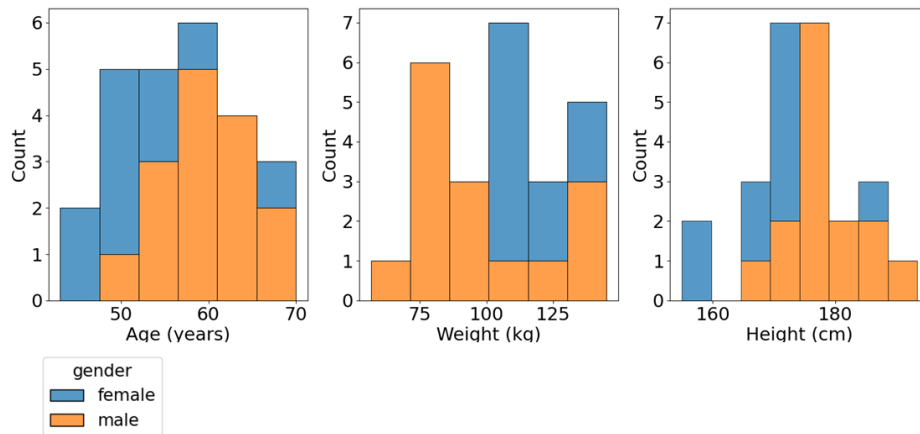


Figure 30: Univariate distributions of characteristics of the subjects used for the SSM.

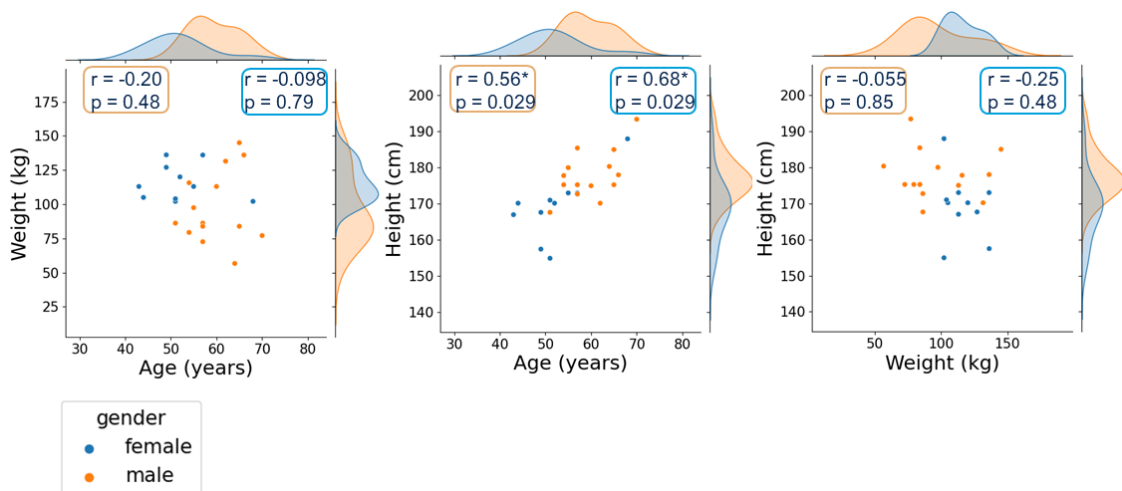


Figure 31: Multivariate distributions of characteristics of the training subjects used for the SSM. p : p -value, r : Pearson correlation coefficient, *: significant correlation.

3.1.2 Segmentation

Inspection of the exported STL files of the segmented tibiae revealed some step artefacts (see **Figure 32**).

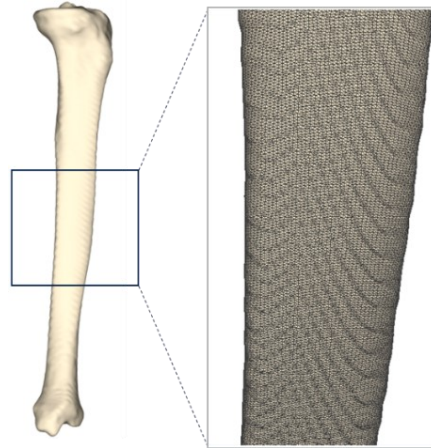


Figure 32: Inspection of mesh quality after segmentation and triangulation. The detail shows step artefacts.

3.1.3 Automated pre-alignment performance

The pre-alignment using the ICP registration algorithm achieved automated registration in 3.86 seconds and the result is shown in **Figure 33A-B**. The average fitness - which measures the number of inlier correspondences divided by the number of points in the target - was 0.99991. The average root-mean-squared error (RMSE) of all inlier correspondences was 3.30 mm.

3.1.4 Initial estimated means

The initial estimated mean that was computed from the pre-aligned tibiae (**Figure 33B**) using signed distance functions is shown in **Figure 33C**. It can be observed that the distal malleoli are missing because of differences in the length of the shapes and the lack of available correspondences. The mean that was computed using by averaging the coordinates of the initial morphed training shapes is shown in **Figure 33D**.

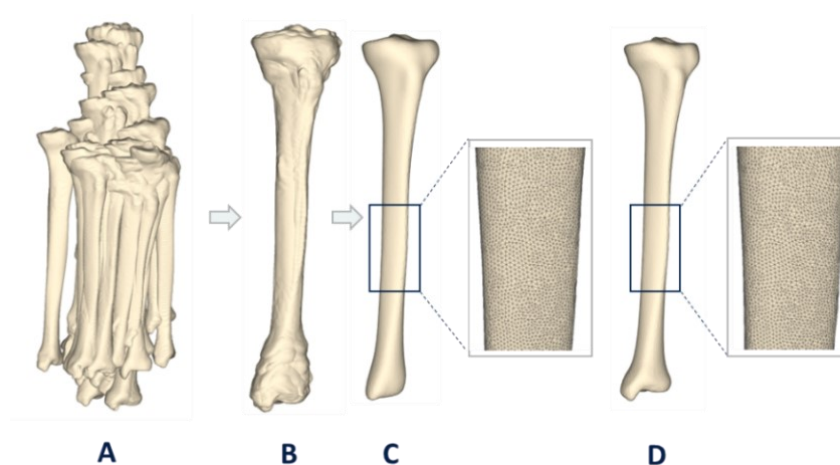


Figure 33: Shape alignment and estimation of the mean shape. A: unaligned tibiae. B: pre-aligned tibiae. C: Initial estimated mean computed using signed distance functions of pre-aligned tibiae without correspondences. D: second estimated mean computed by averaging the coordinates of the initial morphed training shapes. The details show that step artefacts are smoothed out.

3.1.5 Establishing correspondences: morphing performance

Automated morphing was achieved in under 8 minutes per tibia sample. Using the initial estimated mean from **Figure 33C**, the average mean Hausdorff distance between the morphed samples and the target samples was 0.103 mm (± 0.00709 mm) with an average maximum distance of 2.77 mm (± 1.24 mm), typically located in the lateral malleolus. Such a typical morphing result using the initial mean is shown in **Figure 34A**. Using the second estimated mean from **Figure 33D**, the average mean Hausdorff distance between the morphed sample and the target sample was 0.102 mm (± 0.00606 mm) with an average maximum distance of 1.54 mm (± 0.676 mm). A typical morphing result using this mean is shown in **Figure 34B**.

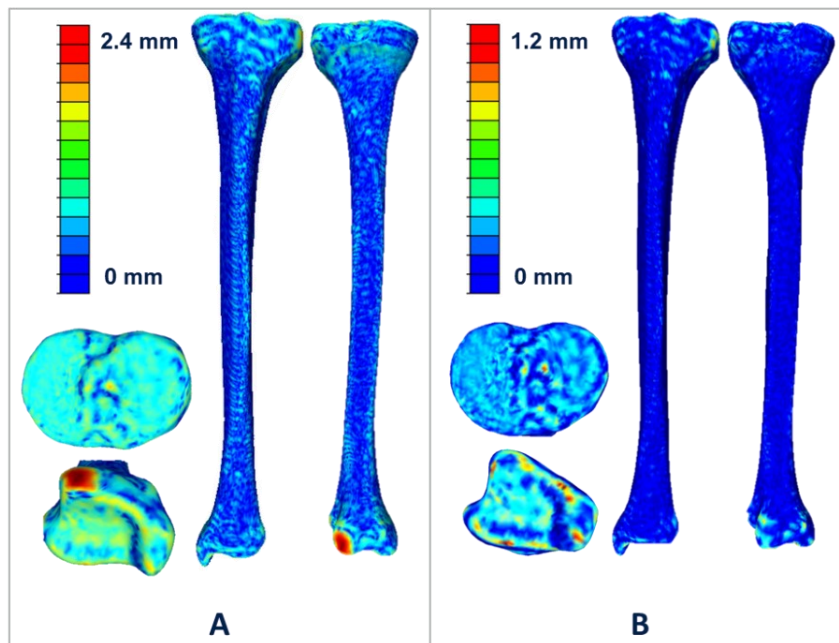


Figure 34: Hausdorff distance of original mesh (target) compared to the morphed mesh of one subject. A: morphed using the initial mean. B: morphed using the second mean.

3.1.6 Principal component analysis

The captured variation in the training population is shown in **Figure 35**. The first five PCs were retained ($c = 5$) since together, they captured 90% of the shape variation in the training population.

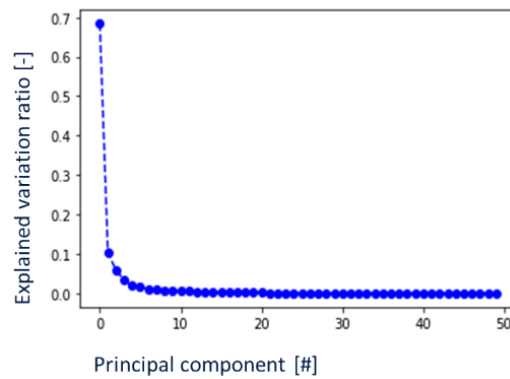


Figure 35: Captured variation per principal component (PC). All the PCs up to an accumulated captured variance of 0.9 were retained, *i.e.*, 5 PCs.

The shape variation represented by these five PCs is depicted in **Figure 36** and **Figure 37**.

The changes observed along the PCs were (mainly) in:

- PC1: the length of the tibia
- PC2: the anterior border along the tibia shaft and in the distal and proximal epiphyses
- PC3: the distal and proximal epiphyses
- PC4: the medial malleolus, and along the tibia shaft
- PC5: the tibial tuberosity and diameter of the tibia

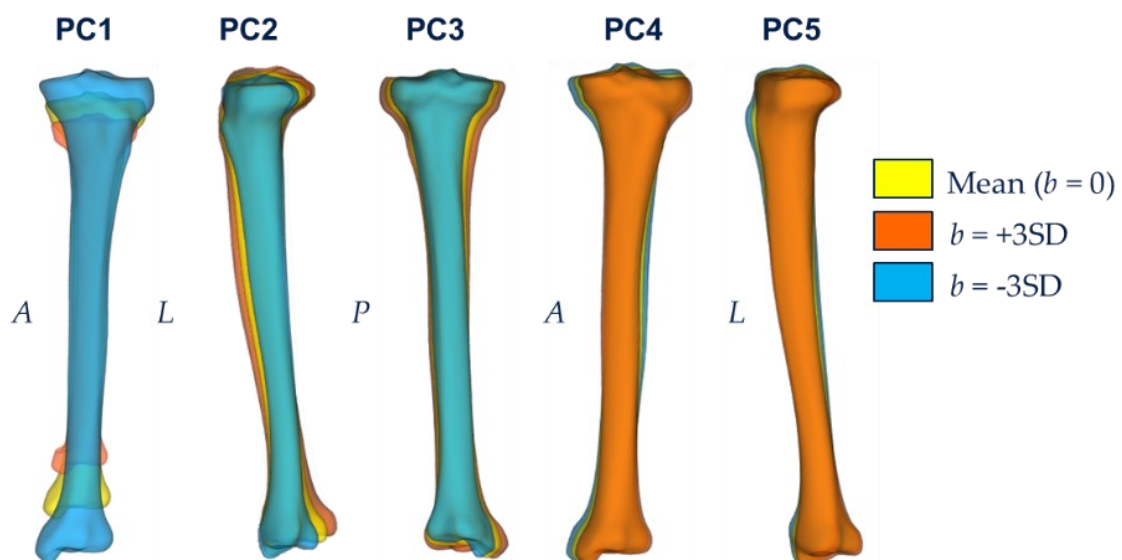


Figure 36: Mean tibia shape and shape variations described by the first five PCs. PC: principal component (=shape mode), SD: standard deviation, A: anterior, L: lateral, P: posterior.

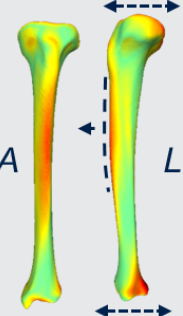
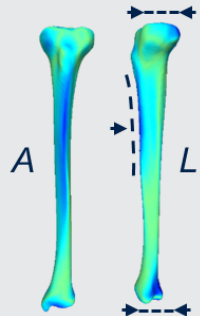
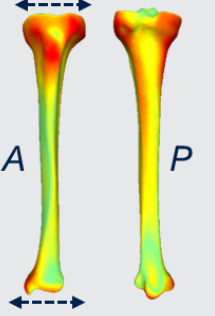
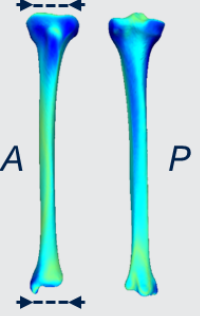
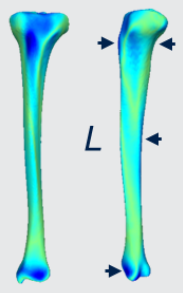
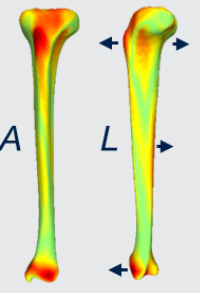
PC	+3SD	-3SD	Scale	Description
1				Changes in the length of the tibia
2				Changes in the anterior border along the tibia shaft and in the distal and proximal epiphyses
3				Changes in the distal and proximal epiphyses
4				Changes in the medial malleolus and along the tibia shaft
5				Changes in the tibial tuberosity and diameter of the tibia

Figure 37: Distance maps between the tibial shape at the extremities (+3SD or -3SD) and the mean tibial shape. PC: principal component (= shape mode), SD: standard deviation. A: anterior, L: lateral, P: posterior, arrows: direction of shape change.

3.2 Multilinear regression models

Pearson correlations between patient characteristics (*i.e.*, gender, age, weight, and height) and shape model parameters of the training subjects are shown in **Figure 38**. Significant correlations were found between the first mode of variation and all the patient characteristics. For the second mode of variation, significant correlations were found with gender and weight. The third mode was found to be significantly correlated to gender and the fourth mode to weight. No significant correlations were found regarding the fifth mode of variation.

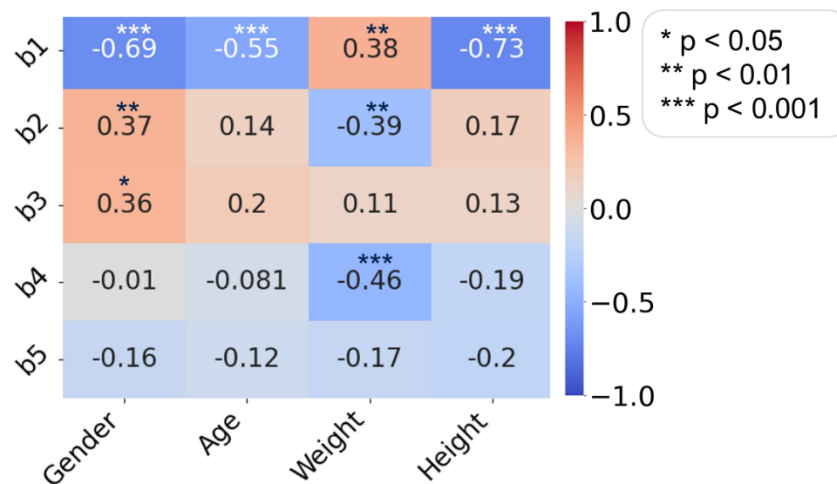


Figure 38: Pearson correlation coefficients (r) between patient characteristics and shape model parameters (b_s) in the training population. Significant correlations are indicated with *.

To correct for multicollinearity caused by correlations between the explanatory variables (*i.e.*, the patient characteristics), variables were centred. The variation inflation factors after these operations are listed in **Table 4**.

Table 4: Variance inflation factor (VIF) after centring to assess multicollinearity between the explanatory variables.

Explanatory variable	VIF
Gender	1.19
Age	2.22
Weight	1.15
Height	2.29

Training of the multilinear regression models resulted in the regression coefficients summarized in **Table 5**. R^2 -values indicated that 68% of the variation in the first shape model parameter (b_1) could be explained by the patient characteristics. For the other shape parameters, this was considerably less (21%, 21%, 36% and 15% for b_2 , b_3 , b_4 , and b_5 respectively). The p -values considering the F -statistic indicated that each regression model is significant except for the regression model predicting the last shape model parameter (b_5).

Table 5: Regression coefficients (w) of the multilinear regression models relating patient characteristics to shape model parameters (b_s).

	b_1	b_2	b_3	b_4	b_5
w_0	474.19	-108.92	-147.89	38.86	41.43
w_{gender}	-790.32	181.52	246.48	-64.76	-69.06
w_{age}	13.47	-0.45	-0.041	6.77	3.95
w_{weight}	1.56	-4.24	3.23	-4.93	-1.99
w_{height}	-58.54	-1.94	-0.98	-10.08	-5.24
R^2	0.68	0.21	0.21	0.36	0.14
p -value	< .001	.030	.029	< .001	.147

3.3 SSM-to-patient fitting

To test the accuracy of the developed SSM-to-patient fitting algorithm, *i.e.*, its ability to predict the tibia geometry of a previously unseen patient, two cases were used: a fractured patient case and an intact validation case. The fitting accuracy for these two cases is summarized in the sections below.

3.3.1 Fractured patient case

The initial bounding box dimensions of the projected shape that was reconstructed using the patient characteristics of the fracture case (see **Table 1** in section 2) are summarized in **Table 6**. The bounding box dimensions after the first optimization step (*i.e.*, optimization of the shape parameters b_s with respect to the bounding box dimension difference) are also listed in **Table 6**. Successful fitting was achieved with a maximum error of 0.1 mm of the bounding box depth in the mediolateral plane. A higher error (3.8 mm) of the length of the fitted mediolateral projection was determined since the optimization function does not take this parameter into account. The optimization was terminated successfully after 816 function evaluations and five iterations in 4.7 seconds.

Table 6: Bounding box dimensions of the contours as measured on X-ray compared to bounding box dimensions of the projected reconstructed shapes of the fractured patient case. AP: anteroposterior, ML: mediolateral.

	Length _{AP} [mm]	Width _{AP} [mm]	Length _{ML} [mm]	Depth _{ML} [mm]
True (X-rays)	435.6	87.3	430.5	71.4
Projected initial shape	459.3	93.2	457.3	78.2
Difference	23.7	5.9	26.8	6.8
Projected bounding box fitted shape	435.6	87.3	434.3	71.5
Difference	0.0	0.0	3.8	0.1

Refinement of shape parameters b_s and pose T such that the distances between the concave hulls of the projections of the transformed SSM realization and indicated contour points were minimal, was achieved successfully after 2481 function evaluations and nine iterations in 23 seconds. **Figure 39** shows the fit of the (2) bounding box-optimized and (3) contour-optimized

shapes as compared to the X-ray contours. The maximum distances between the indicated contours and the contours of the projected bounding box fitted shapes were 14.3 mm and 7.53 mm for anteroposterior and mediolateral projections respectively. The mean distances between the indicated contours and the contours of the projected shapes were 5.67 mm and 4.54 mm for anteroposterior and mediolateral projections respectively. The maximum distances between the indicated contours and the contours of the projected contour-fitted shapes were 4.44 mm and 4.20 mm for anteroposterior and mediolateral projections respectively. The mean distances between the indicated contours and the contours of the projected shapes were 1.53 mm and 1.54 mm for anteroposterior and mediolateral projections respectively. The largest distances were found in the medial malleolus of the tibia.

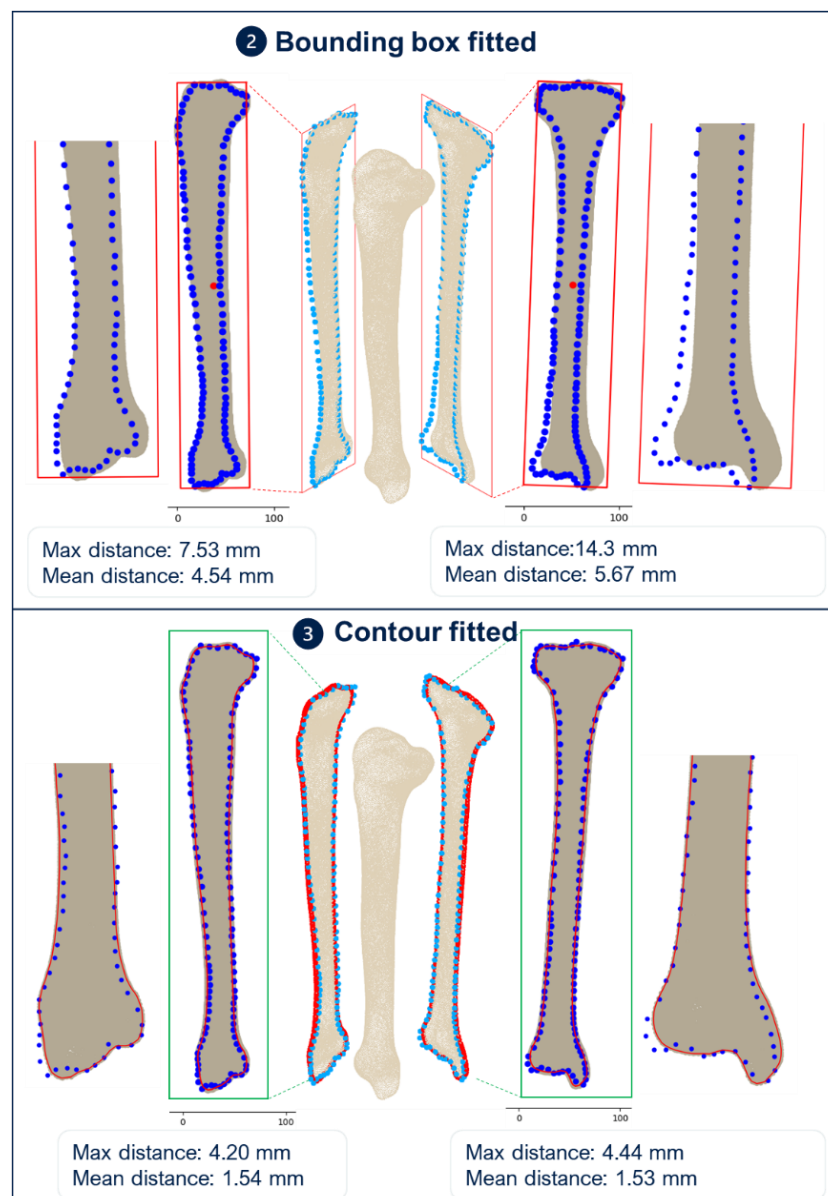


Figure 39: Fit of (2) bounding box optimized and (3) contour fitted SSM shape realization as compared to the anterolateral (AP) and mediolateral (ML) X-ray contours of the fractured patient case. Beige: optimized SSM shape realization. Red boxes: bounding boxes. Red lines: concave hulls. Blue dots: contours as indicated on AP and ML X-rays. Distances are measured between the indicated contour points and the concave hulls of the projected shape realization.

3.3.2 Intact validation case

The initial bounding box dimensions of the projected shape that was reconstructed using the patient characteristics of the validation case (see **Table 1** in section 2) are summarized in **Table 7**. The bounding box dimensions after the first optimization step (*i.e.*, optimization of the shape parameters b_s with respect to the bounding box dimension difference) are also listed in **Table 7**. It can be observed that successful fitting was achieved with a maximum error of 4.6 mm. The optimization was terminated successfully after 522 function evaluations and three iterations in 3.2 seconds.

Refinement of shape parameters b_s and pose \mathbf{T} such that the distances between the concave hulls of the projections of the transformed SSM realization and indicated contour points were minimal, was achieved successfully after 2876 function evaluations and 10 iterations in 25.4 seconds. Distances between the contours of the projections of the contour-fitted shape and the indicated contour points are summarized in **Table 8**. Contour distances of the bounding box fitted shape (so before contour fitting) are also reported. Mean contour distances decreased from 2.04 mm to 1.23 mm and from 1.70 mm to 1.20 mm in the anteroposterior and mediolateral planes respectively after contour fitting as compared to bounding box fitting. **Figure 40** shows the accuracy of the reconstructed shape of the validation case in 3D. For each fitting step, Hausdorff distances and overlay plots between the reconstructed 3D shape and the true 3D shape are shown. The mean distance in 3D after all fitting steps was 0.81 mm with a maximum distance of 4.22 mm. The highest distances were found on the lateral tibial plateau and tibiotalar articular surface.

Table 7: Bounding box dimensions of contours as measured on X-ray compared to bounding box dimensions of projected reconstructed shapes of intact validation case. AP: anteroposterior, ML: mediolateral.

	Length_{AP} [mm]	Width_{AP} [mm]	Length_{ML} [mm]	Depth_{ML} [mm]
True (X-rays)	373.2	76.5	380.4	67.6
Projected initial shape	406.6	79.7	410.1	64.6
Difference	33.4	3.1	29.7	3
Projected bounding box fitted shape	373.1	76.9	375.8	65.1
Difference	0.1	0.4	4.6	2.5

Table 8: Distances between concave hulls of reconstructed shape as compared to contours as indicated on X-rays of intact validation case. AP: anteroposterior, ML: mediolateral.

	AP contour distance [mm]		ML contour distance [mm]	
	<i>Mean</i>	<i>Max</i>	<i>Mean</i>	<i>Max</i>
Bounding box fitted shape	2.04	5.17	1.70	7.20
Contour-fitted shape	1.23	6.18	1.20	5.69

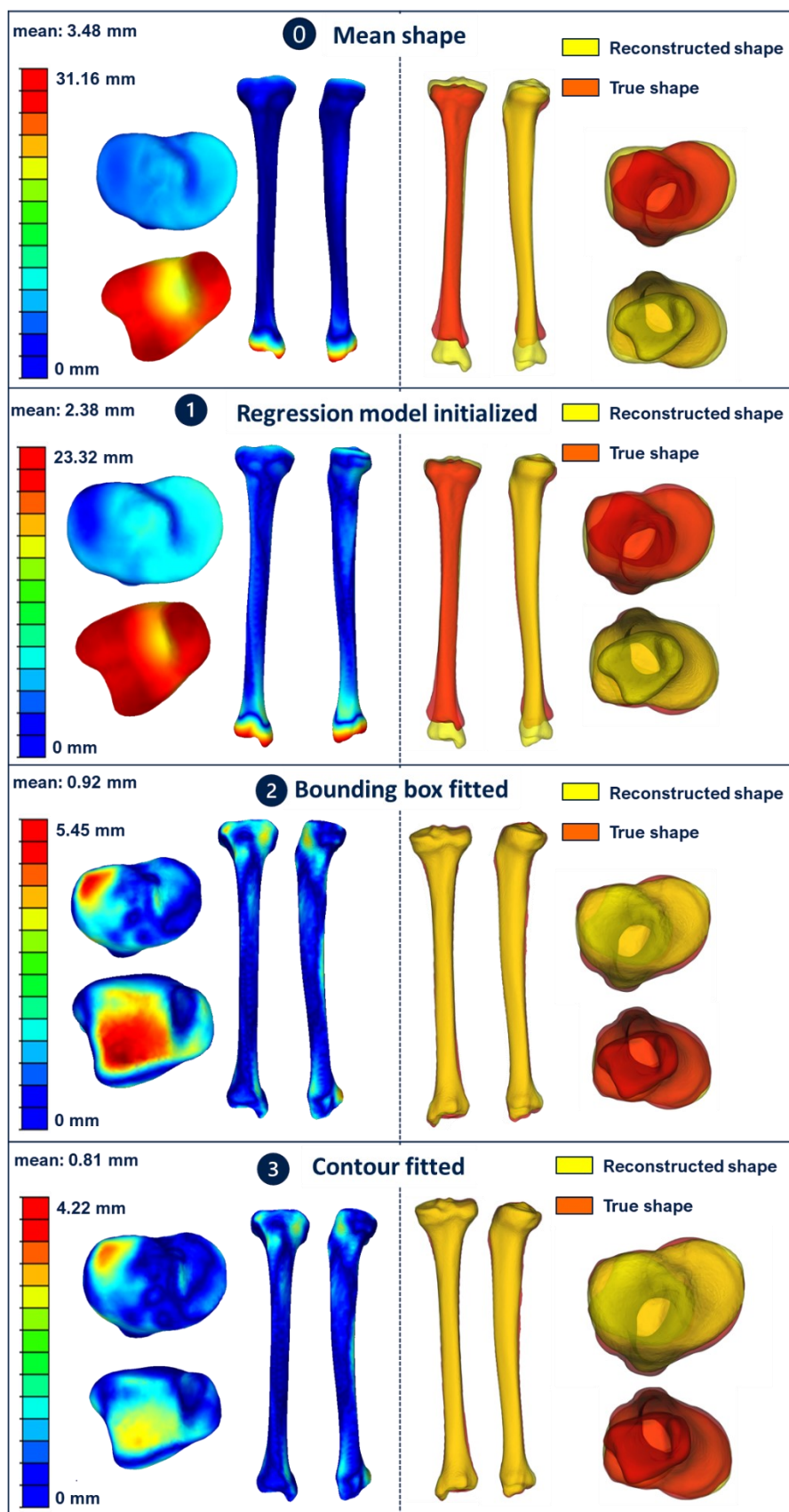


Figure 40: Reconstructed shapes using (0) the mean of the SSM, (1) multilinear regression, (2) bounding box fitting and (3) contour fitting as compared to the true segmented 3D shape for the intact validation case. Left column: Hausdorff distances of the reconstructed shape to the true shape. Right column: Overlay of the reconstructed shape and the true shape.

3.4 FE analysis

The spiral diaphyseal tibia fracture of the fractured patient case, fixated with a locking plate of two different materials, two different lengths and three different screw positions, was investigated. This was done by developing FE models of these cases and running FE analyses. In the following sections, results from these models and analyses are discussed.

3.4.1 Mechanical strains and motions within the fracture region

The maximum absolute principal strain distribution in the fixated fractured bone - and specifically in the callus - for the real clinical postoperative fixation scenario (scenario 1), is shown in **Figure 41**. The tibia was predicted to be under bending in the region proximal to the fracture, with tension on the anteromedial side and compression on the posterolateral side (**Figure 41**). Strains within the cortical bone were predicted to be between -0.045% and 0.017%. Strains within the callus were higher, between -10% and +2.2%.

3.4.1.1 Sensitivity analysis

Screw positions, plate length and plate/screw material were altered in scenarios (2), (3), (4) and (5) respectively and the differences in mechanical strains within the callus were quantified. The strain distributions were similar in the different scenarios (**Figure 41**), however, considerably different strain ranges were determined. The maximum absolute principal strain maps of these scenarios can be found in *Appendix G*. Boxplots of the quantified minimum and maximum principal strain distributions within the callus for the five different investigated scenarios are shown in **Figure 42A** and **Figure 42B** respectively.

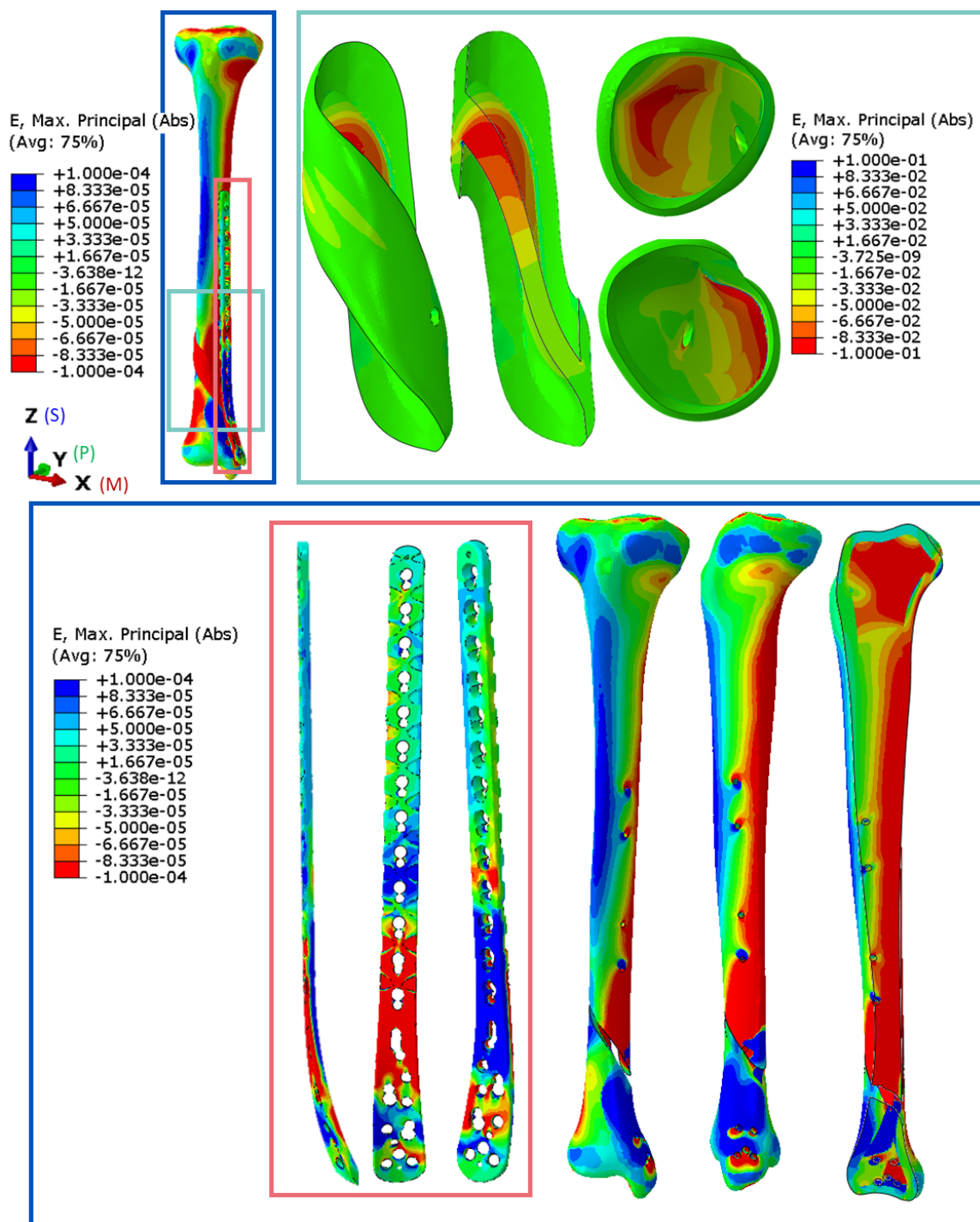


Figure 41: Maximum absolute principal strain [-] distribution of the fixated fractured tibia. Green box: callus region. Blue box: tibia bone region. Pink box: locking plate.

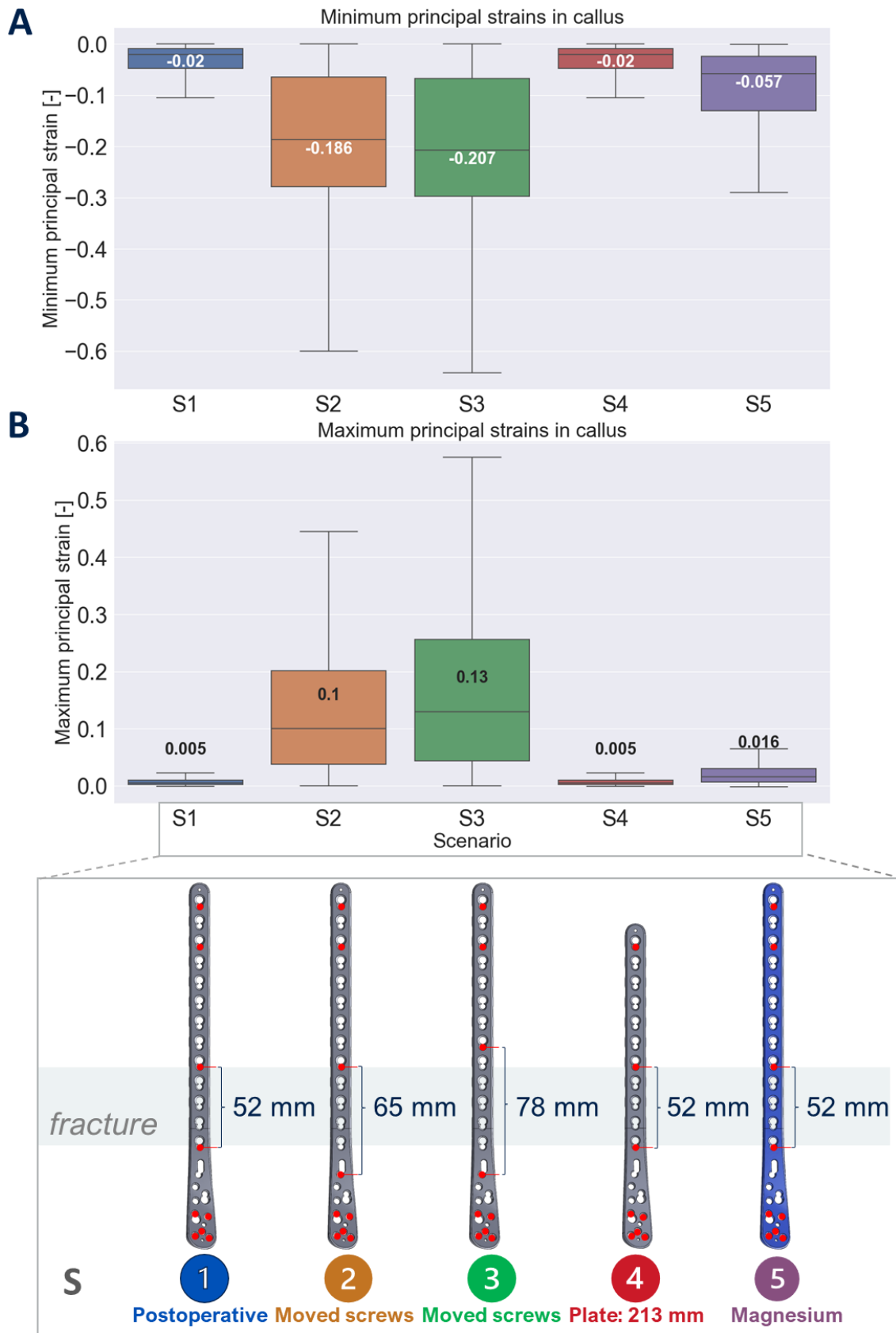


Figure 42: Boxplots of the minimum (A) and maximum (B) principal strains [-] within the callus for the five different fixation scenarios (S1-S5). Lower and upper box boundaries: 25th (Q1) and 75th (Q2) percentiles respectively, making up the interquartile range (IQR). Line inside box + number: median. Lower and upper error lines: $Q1 - 1.5 \cdot IQR$ and $Q2 + 1.5 \cdot IQR$ respectively.

It can be observed that the minimum principal (compressive) strains of the true clinical postoperative scenario (S1) and of the case with a fixation with a shorter plate length (S4) were between 0 and 10%. The compressive strains of scenarios with a larger working length (S2 and S3) were between 0 and 60% and 0% and 64% respectively. Simulation of fixation with a magnesium plate (S5) resulted in compressive strains between 0 and 29%. The maximum principal (tensile) strains of scenarios 1 and 4 were between 0 and 2.2% while the tensile strains of scenarios 2 and 3 were between 0 and 45% and 57%, respectively. The tensile strains of scenario 5 were between 0 and 6.5%.

The quantified minimum principal strains and maximum principal strains along the path defined within the callus region going from the fixator side (medial) to the lateral side are shown in **Figure 43** and **Figure 44**, respectively.

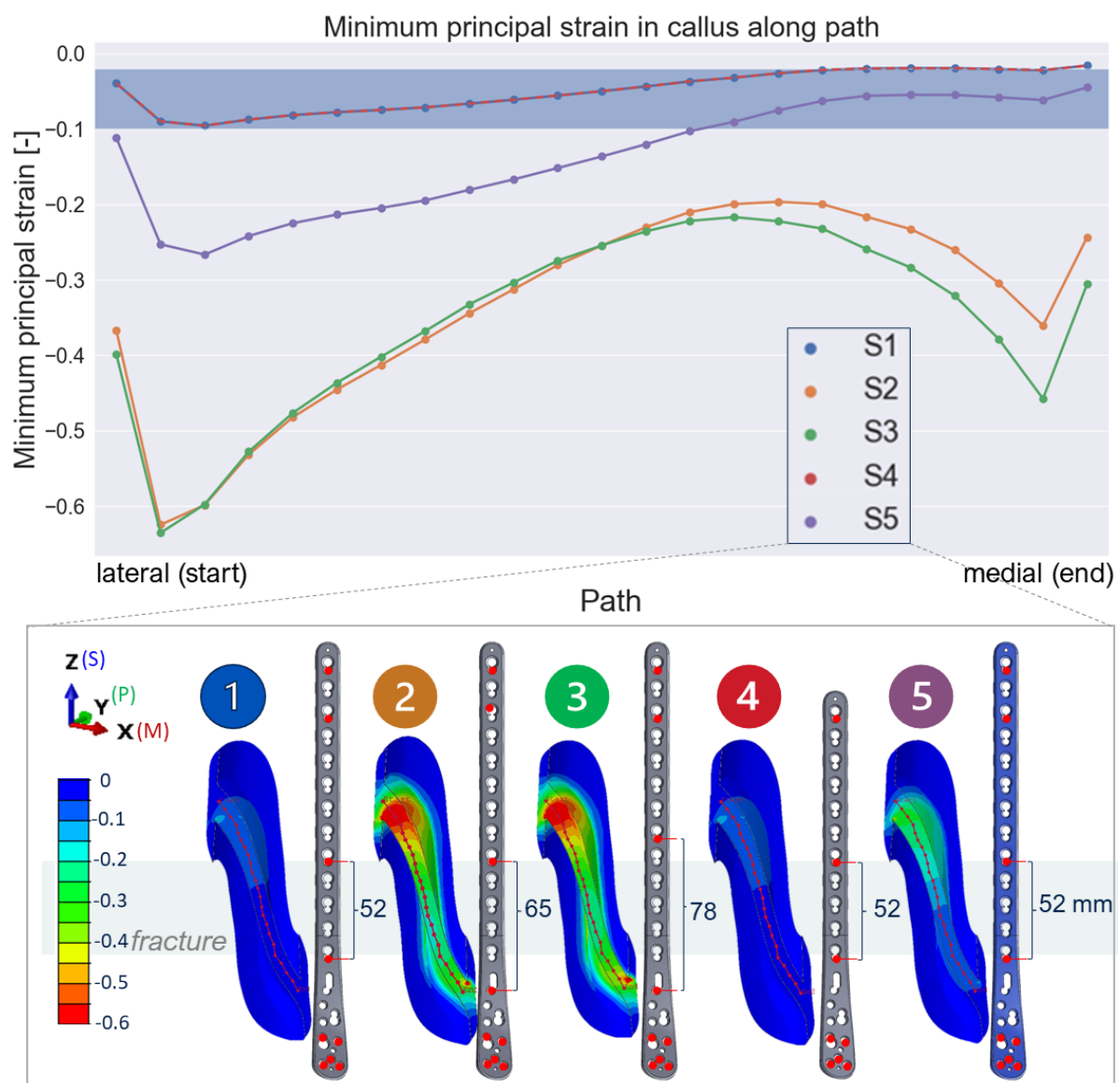


Figure 43: Minimum principal strains [-] found along the path in the callus for the five different fixation scenarios. The path runs from lateral to medial, *i.e.*, from far-cortex to near-cortex relative to the plate. Shaded region: reported optimal strain range for bone formation [13]. *Notes:* the scale of the callus is larger compared to the plate for visualization purposes; lines of S1 and S4 overlap.

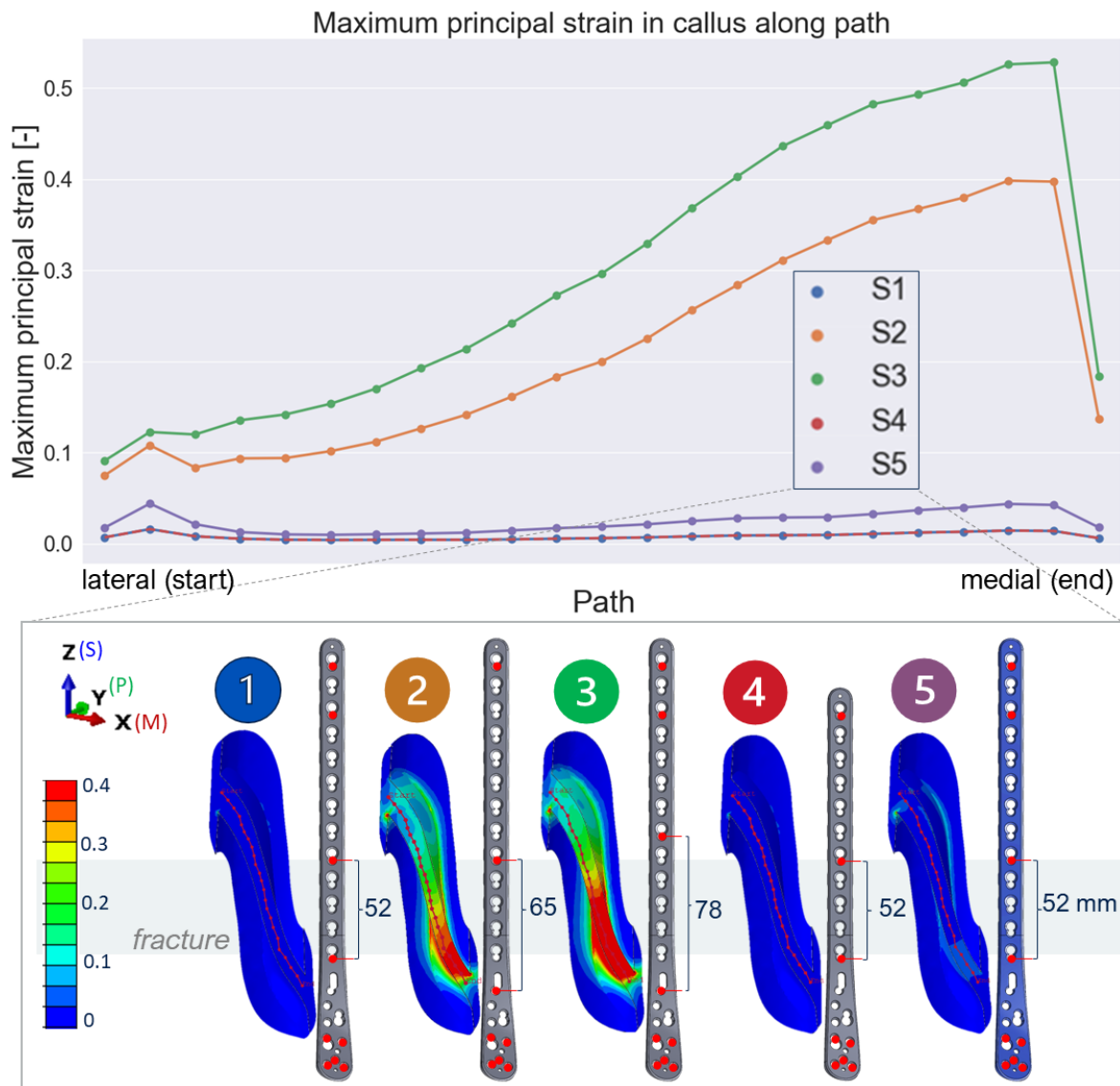


Figure 44: Maximum principal strains [-] found along the path in the callus for the five different fixation scenarios. The path runs from lateral to medial, *i.e.*, from far-cortex to near-cortex relative to the plate. *Notes:* the scale of the callus is larger compared to the plate for visualization purposes; lines of S1 and S4 overlap.

It can be observed in **Figure 43**, that compressive strains decrease for all scenarios along the path from lateral to medial. Plate length did not considerably influence the strains within the callus. Similar strains were determined for the true clinical postoperative fixation scenario (S1) and the scenario with a shorter plate length (S4). From **Figure 44**, it can be observed that tensile strains increase along the path from lateral to medial for the scenarios with a longer working length (S3 and S4). For the other scenarios, predicted tensile strains are low (0-6.5%) and do not exhibit changes along the callus path.

The relative motions in the axial (local U1) and shear (local U2) directions between the defined node pairs for the different scenarios are shown in **Figure 45A** and **Figure 45B** respectively.

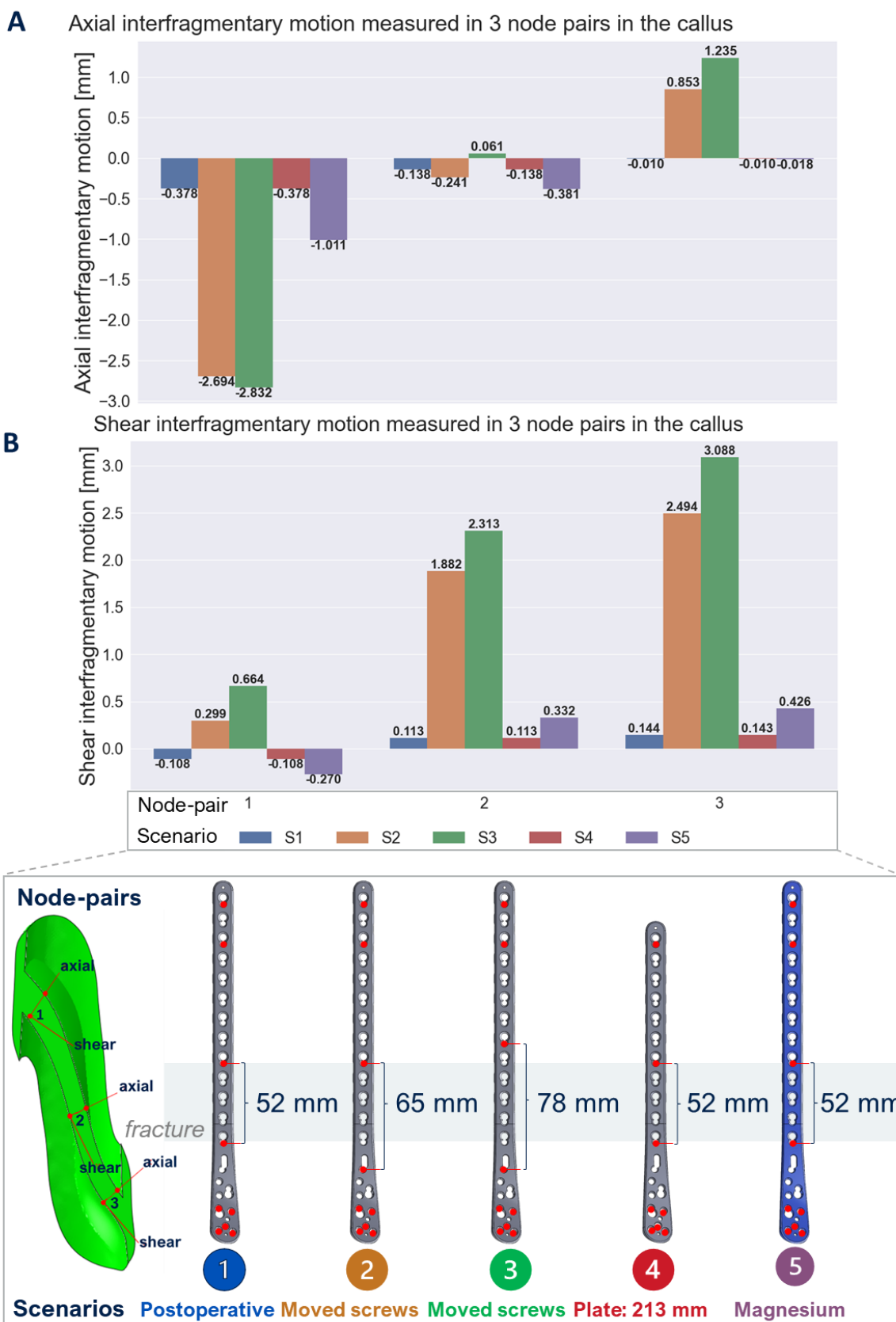


Figure 45: Relative interfragmentary motions (IFMs) (mm) in the axial (A) and shear (B) directions between three node pairs in the callus region for the five different scenarios. The motions are quantified in the local coordinate systems defined by the node pairs, *i.e.*, relative to the fracture lines.

Compressive axial IFMs of up to -0.38 mm were predicted for the true clinical postoperative fixation scenario (S1) (**Figure 45A**). Shear motions of up to 0.14 mm were predicted for this scenario (**Figure 45B**). This scenario was predicted to have the smallest axial and shear IFMs. A strong influence of screw positioning on both the axial and shear IFMs was determined. Highest axial (-2.83 mm) and shear (3.09 mm) motions were predicted for the plate with the highest working length (78 mm) (S3). In the two scenarios with a larger working length (S2 and S3), tensile axial motions were predicted for the most medial node pairs nearest to the plate, while this was not the case for the other scenarios. For the plate with the highest working length (78 mm) (S3), a tensile axial motion was also predicted for the central node pair. For the other scenarios, higher compressive axial IFMs were predicted in the node pairs far from the plate (*i.e.*, most laterally). Shear motions were predicted to decrease for node pairs further from the plate for all scenarios. For all scenarios, except for the scenarios with a higher working length, the direction of the shear IFM was reversed in the most lateral node pair (node pair 1) as compared to the central and medial node pairs.

4 DISCUSSION

In this study, a (semi-)automated workflow was established for the development of 3D patient-specific FE models of long bone fractures based on 2D X-ray images. The developed methodology was able to reconstruct the 3D geometry of a fractured tibia bone based on two orthogonal X-rays and patient characteristics (age, gender, weight, and height). This was done by developing methods to (1) generate an estimate of the patient-specific intact 3D bone shape using statistical shape modelling, (2) automatically model the patient-specific fracture lines into this shape, and (3) develop patient-specific FE models of the fixated tibia. It was shown that screw location considerably influences the mechanical strains within the healing region, which is known to influence healing outcomes. Fixation material had little effect on the predicted mechanical strains. Such knowledge could ultimately be incorporated into the pre-operative planning of bone-fracture fixation surgery to support clinical decision-making regarding the optimal osteosynthesis for the individual patient in order to prevent implant failure and non-union development.

It was shown to be feasible to develop these models using only limited clinical imaging data available in clinical practice (*i.e.*, X-rays). The automated reconstruction of patient-specific 3D geometrical models of the fractured bone based on 2D X-ray images eliminates the need to acquire preoperative thin-slice CT scans. This has the potential to reduce radiation exposure for the patient. Additionally, this approach fits better within the current clinical routine of bone fracture management where a thin-slice CT scan of the whole fractured bone is not made.

In the following sections, the presented methods and results will be discussed in more detail. For each step, results are discussed, as well as the assumptions and limitations of the methods taken to acquire these results.

4.1 Tibial SSM

An SSM of the tibia was established based on 50 segmented training shapes (*i.e.*, 25 subjects). While some step artefacts were present after the segmentation of these shapes, these were smoothed out during morphing and PCA. Pre-alignment, estimation of the mean shape, correspondence establishment using a morphing approach, GPA and PCA of the shapes were automatically achieved using only open-source software.

The distances between the morphed shapes and the original shapes were on average less than 1 mm, and the maximum error was on average 1.5 mm. These errors are not clinically relevant [82], especially considering that they may also be attributed to the smoothing out of segmentation artefacts.

The results from the PCA were in accordance with previously developed SSMs of the tibia. In this study, it was found that the first shape mode of variation was related to the length of the

tibia. Similarly, Tümer *et al* (2019) [40] found this to be related to the second shape mode. This difference in component order may be attributed to the fact that Tümer *et al* (2019) [40] scaled the tibiae prior to PCA. The second mode of variation of the tibia was found to be related to changes in the anterior border along the tibia shaft and the lateral and medial condyles and malleoli. Tümer *et al* (2019) [40] found the same variation to be related to the first shape mode. The third shape mode was found to be related to changes in the epiphyses in accordance with Tümer *et al* (2019) [40].

4.2 Multilinear regression models

Regarding correlations with patient characteristics, gender was found to be related to changes in the condyles of the tibia (2nd shape mode), which is in line with work from Bellemans *et al* (2010) [83], Wise *et al* (2016) [84] and Brzobohatá *et al* (2015/2016) [85][86]. Additionally, it was found that the length of the tibia was strongly correlated with all patient characteristics including gender, which is also in line with work from Bellemans *et al* (2010) [83] and Bruce *et al* (2022) [87].

However, no Bonferroni adjustment for multiple comparisons was done in the current study. Furthermore, the correlations were not sufficient to be able to predict a patient-specific tibial geometry accurately. On a test case not included in the SSM and regression models, errors of more than 20 mm were found when attempting to reconstruct the tibial geometry based on patient characteristics. Even though one case is not sufficient to assess the models' performance, it does demonstrate how (in-)accurate the reconstruction can be for a specific patient.

Regarding the training cohort, the sample size and the number of females involved in the dataset were limited. The small dataset could affect the statistical power of the models. Additionally, the chosen age range could affect the generalizability of the model, especially considering that the age of the test case of the patient with a spiral diaphyseal tibial fracture was not within the age of the cohort used to train the SSM and multilinear regression models. Furthermore, there were significant correlations between the patient characteristics height and age (male: $r = .57$, $p < .05$; female: $r = .68$, $p < .05$) in the training cohort. This correlation should not exist in an adult population and is likely a coincidental result of using a limited age-selected training cohort. Even though collinearity was corrected for using standardization of the variables, this could still impact the estimation of the multilinear regression coefficients. In future studies, a larger training population should be used.

Another limitation of the developed SSM is that only the outer cortical surface was included. Therefore, patient-specific trabecular bone geometries could not be established using the model. In this study, the cortical thickness was assumed to be uniform throughout the tibia and the space in between was assumed to be filled with bone marrow. Since the study aimed to predict the strains within the callus, it can be assumed that cortical thickness will not have a strong influence on the predicted strains. However, this remains to be investigated.

Additionally, bone density distribution and therefore heterogeneous bone material properties were not included in the model. Including bone density in the statistical shape model could simplify the automated 2D/3D registration of the SSM to two orthogonal X-rays. Future studies should therefore aim for the development of an SSAM which takes into account patient-specific bone density distribution as well.

4.3 SSM-to-patient fitting

Nevertheless, in this study, it has been shown that it is feasible to estimate the 3D shape of a patient-specific intact tibia based on the SSM, patient characteristics and two orthogonal X-rays. An important condition is that the X-rays of the fractured tibia are not displaced (*i.e.*, like the clinical test case), such that the contours of the bone are continuous and correspond to intact tibia contours. For the clinical fractured tibia case, 3D reconstruction was achieved in under 30 seconds with a mean contour distance of less than 2 mm for both frontal and lateral X-ray views. Maximum distances reached up to 4.44 mm in the regions around the distal epiphysis. It should however be noted that this error could also be attributed to the fact that the X-rays of the test case concern a fractured tibia which might not be perfectly reduced. Additionally, it should be pointed out that the true 3D tibial shape of this clinical test case is not known because the CT scans were not available. Therefore, the estimated geometries of this case could only be assessed in 2D based on the X-rays and not in 3D. Additional validation was therefore performed using a CT scan of an intact tibia, that was not previously used as training data for the SSM and multilinear regression models. For this test case, the 3D shape was reconstructed based on the DRRs of the CT scans. The reconstructed 3D shape had a mean error (*i.e.*, Hausdorff distance) of less than 1 mm. The maximum error reached up to 4.22 mm, in the regions around the proximal and distal epiphyses.

Future work should include fractured patient cases that have preoperative CT scans of the fractured tibia available. Additionally, the developed fitting algorithm requires assumptions about the X-ray setup used to acquire the X-rays. It is assumed that the X-ray planes are exactly orthogonal. Additionally, the source-imager-distance and source-object distance are required. These parameters are usually not available in the DICOM files but could be stored during acquisition.

4.4 Fracture line modelling

The fracture lines were extracted from the X-rays manually and introduced into the intact 3D tibia shape automatically using polyhedron cropping. Fracture lines were only extracted from the frontal X-rays, disregarding the additional data that could be collected from the lateral X-rays to improve the 3D fracture line estimation. Future studies should assess whether this might improve the 3D fracture line estimation using a test case where the true fracture lines in 3D space are known. In the current study, this was not yet possible due to the unavailability of this data.

Furthermore, the developed polyhedron cropping methodology requires assumptions regarding the depth of the fracture line in the anteroposterior direction, since this information is lost during X-ray projection. During back-projection, it was assumed that the depth of the fracture lines is constant for anterior and posterior fracture lines. However, in reality, this is not true since the tibia is approximately cylindrical. To solve this limitation in future studies, the projected fracture line coordinates could iteratively be matched to points on the 3D tibia surface.

For now, the postprocessing of the fracture fragment geometries was done manually through the GUI of Meshmixer since it was only required for one test case. However, this step could also be automatized using the scripting Application Programming Interface (API) for Autodesk Meshmixer²⁶.

4.5 FE models & analysis

FE analysis of the fixated fractured bone of the test case predicted compressive strains within the fracture region in the range of 0-10% with a median value of 2%. This range has previously been reported in the literature to be optimal for bone formation [11], [13], [88]. Increasing the plate working length by changing the screw positions led to much higher compressive strains (almost 10 times as high). This is in line with previous studies [60], [63], [89]. Additionally, large tensile strains were also found in these scenarios, which were negligible in the other scenarios (<1% for the true clinical scenario and <2% for the scenario with a magnesium plate). It has been proposed that delayed healing and non-union might occur when the strains are over a certain threshold (*i.e.* 10%) [88]. These results suggest that having an excessive plate working length might result in such complications. Therefore, the current workflow allows for an informed decision on the appropriate locking plate fixation configuration and has the potential to minimize the negative impact of excessive strains on bone healing. Decreasing the plate length, while keeping the same screw configuration, had no impact on the biomechanical conditions within the fracture gap. Currently, used fixation plates are made of titanium or stainless steel, which are not resorbable, creating the need for a second surgery to remove the plate in some cases. Ideally, plates should be resorbable, and magnesium has been suggested as an alternative to conventional titanium and stainless-steel alloys [72]. Changing the material properties of the plate to magnesium, which has a lower elastic modulus, did result in a three-fold increase of the strains in the callus. This could be beneficial in scenarios where the bone is subjected to lower loads. However, in the current simulated postoperative scenario, the true clinical postoperative fixation scenario was predicted to be most appropriate.

To the author's knowledge, the mechanical environment within the fracture region after osteosynthesis of a spiral tibial fracture has not been investigated in previous studies. However, the found IFMs and strains of the clinical postoperative fixation scenario are comparable to values reported in previous *in silico*, *in vitro* and *in vivo* studies of transverse

²⁶ <https://github.com/meshmixer/mm-api>

and oblique fractures. In the current study, axial compressive IFMs up to 0.38 mm and compressive strains up to 10% were found for the true clinical postoperative fixation scenario where the fractured bone was fixated with a working length of 52 mm. Shear IFMs of 0.11 mm were found for this scenario. Kenwright *et al* (1998) [11] reviewed studies that measure IFMs throughout healing in patients with tibial diaphyseal fractures treated by external skeletal fixation and found similar results up to seven weeks after fracture. Similarly, Miramini *et al* (2016) [61] simulated and measured axial and shear IFMs *in silico* and *in vitro* of oblique (45 degrees) tibia fractures fixated with plates with a working length of 30 mm. They found displacements of approximately 0.24 mm and 0.14 mm in axial and shear directions respectively for loads up to 200 N. Duda *et al* (2002) [15] also simulated and measured IFMs in tibiae with transverse defects and found axial displacements of 0.27 and 0.29 mm, respectively, for loads up to 500 N. They found simulated inter-fragmentary axial strains up to 25% under physiological loading of up to 2070 N. Loads in the current study were different (*i.e.*, 800 N). However, the strains and motions scale linearly with the applied load since a linear analysis was conducted. Considering this, the strains and motions are comparable to these studies [15], [61]. Duda *et al* (2002) [15] also found that an increase in working length led to a considerable reduction in implant loading and increased loading of the bone, in line with the results presented here. It should be noted that in the current study, some very high strains were found along the edges of the callus, which were marked as outliers. These strains can likely be considered numerical artefacts, *e.g.*, due to the merging of nodes and steep geometrical edges.

Additionally, the distribution of the strains and IFMs throughout the callus (*i.e.*, from the lateral cortex to the medial cortex near the plate) is comparable to previously reported studies [61], [90], [91]. In this study, it was found that compressive strains on the lateral edge of the callus (far from the plate) are up to five times as high as compared to strains on the medial edge of the callus (near the plate). Tan *et al* (2021) [91] also found a five-fold increase in strains across the callus using FE analyses of a fixated transverse fractured tibia. For the axial IFMs, this effect was even more pronounced, with an observed increase of almost 40 times. Miramini *et al* (2016) [61] reported similar results in their FE simulation of fixated oblique tibia fractures. Among fractures of 30 degrees, they observed an increase in axial IFMs across the callus of approximately seven-fold for a load of 200 N. For steeper fractures of 45 degrees, they found that the axial IFM turned into a tensile motion for node pairs nearest to the plate. In the current study, this effect was only found for the scenarios with an increased working length. For the fixation scenarios with the true clinical working length in the current study, the difference from lateral to medial was not found for the tensile strains, which were in general very small throughout the callus (<1%). For fixation scenarios where larger working lengths were simulated, high tensile strains were found on the medial side of the callus (near the plate). Tensile strains near the plate were also observed by Miramini *et al* (2016) [61] and Duda *et al* (2002) [15].

To conclude, FE results show that the current models are informative to assess the healing potential of the fixated fractured bone and results are in line with previous studies. However,

the FE models were simplified as compared to physiological reality to decrease the complexity of the simulations. Simplifications and limitations of the models are discussed in the following sections.

4.5.1 Geometries and meshing

First of all, it should be noted that no mesh convergence analysis was performed. Since this study deals with challenging complex geometrical features around the fracture zone, a relatively coarser mesh could not be generated. Therefore, a mesh sensitivity analysis could not be run. However, previous studies have performed mesh convergence analyses [60], [69], and the number of elements used in this work was shown to be appropriate to model tibial locking plate fixation and assess fracture gap biomechanics [60].

Furthermore, physical screw geometries were used rather than beam elements with multi-point constraints [63], [92]. It has been reported that such simplified models have a strong impact on the local stress and strain environment within the assembly [60], [63], [92]. Since screws are passing through the fracture zone of the clinical test case, this was deemed undesirable.

Lastly, the effects of the fracture gap size were not investigated. It has been previously reported a larger fracture gap leads to decreased strains in the fracture zone [61], [88]. In the current study, a relatively large fracture gap size (*i.e.*, 4 mm) was simulated which is easier to mesh.

4.5.2 Materials

Homogeneous, isotropic, linear elastic material models were used, which have previously been shown to be reasonable for modelling tibial fracture gap biomechanics [60]. Since only short-term quasi-static loading was considered, this was deemed reasonable. However, for long-term predictions, fatigue effects may play a role. Furthermore, using an SSAM that includes bone density as well, would allow for the assignment of heterogeneous patient-specific material properties.

4.5.3 Interactions & boundary conditions

Interactions between the different parts of the FE models were modelled using tie constraints. The threadless screw shafts were tied to the screw hole surfaces within the bone, with the rationale that there are negligible motions at these interfaces during sub-failure conditions [19], [52], [90], [93]. This has been previously reported to not significantly influence gap strain predictions [87]. Locking screw connections with the plate were also modelled using tie constraints as is done in most previous studies [60], [69], [92]–[94]. The contact between the bone and the plate was not modelled since it was assumed that these parts never come into contact. This assumption has been made in multiple validated previous studies [60], [95]. More complex frictional contacts have also been previously proposed [94], [96] but since this led to convergence issues and increased simulation times, this was omitted in the current study. Additionally, locking plate/screw systems do not require contact between the plate and the bone since the loads are mostly carried by the screws and fragments are stabilized by the

locking mechanism between the screws and plate [32], [33]. Additionally, small deformations of the tibia were expected and predicted in the postoperative loading scenario.

To prevent rigid body motions, the articular surfaces were constrained to single points in space considered to be the centres of the joints. It was assumed that these joints act as pin supports that allow rotation, while translation is fixed in all directions (except for translation in the axial direction for the knee joint). This is a common assumption for the fractured tibia [15], [60], [63], [97]. Even though the pin condition allows unlimited rotation, while *in vivo* transverse rotations do not exceed ± 3 degrees [98], it is unlikely that the loads present in the immediate postoperative period cause enough deformation to exceed allowable movements at the joints [60]. In the simulated scenarios, the rotation at the joints did indeed not exceed 0.6 degrees. It has also been previously proposed to constrain the bone by fixation of both translations and rotations at both ends of the bone. However, this has been previously reported to lead to an underestimation of the natural deformation of the bone through bending [80].

4.5.4 Loading

To the author's knowledge, the exact postoperative loading conditions that act on the tibia after fracture fixation surgery are not known. To quantify the loads acting on the tibia during daily activities, both *in vivo* measurements, as well as inverse dynamic models, have been previously deployed by different authors. However, how these loads are altered in case of a fracture is controversial and dependent on many factors such as postoperative rehabilitation plans, assist devices and patient compliance [94]. Additionally, internal loads generated by muscle forces are almost impossible to control and hard to measure [63].

Ideally, individualized accurate forces would be deduced using full-body musculoskeletal models, including ligaments, tendons, and muscles [99], [100]. This should be considered for future studies. However, in the current study, the resultant load was assumed to act purely axial and was idealized as a single concentrated point force applied to the tibia plateau. St. Venant's principle provides the foundation for this idealization – *i.e.*, even though this idealization will not be valid for regions near the load application point, it should be valid for the fracture region within the diaphysis [97]. Furthermore, previous studies by Duda *et al* (2002) [15] and Braun *et al* (2021) [99] have included individualized joint forces and muscle forces and predicted comparable strains in the fracture region.

4.6 Future outlook

The aforementioned limitations should be addressed in future studies. Additionally, future studies should consider addressing the following general limitations of the proposed workflow.

In the current study, only the immediate postoperative period was simulated. Thus, the effects of stiffening of the callus were not considered. Future studies could couple the developed FE models with agent-based bone healing models to incorporate these stiffening effects [20], [101]. Using the FE models, volumetric strains and octahedral shear strains could be calculated

according to Claes and Heigele [35] and Shefelbine [14]. These strains could subsequently be used in mechanical stimulus equations to predict tissue differentiation and used to adjust the initial material properties of the FE model [101], [102]. In this way, the longer-term fracture healing and cell differentiation pattern could be assessed.

Furthermore, the proposed methods are currently only suitable to model non-displaced fractures, since displaced fractured bones are not part of the SSM. To make the established workflow suitable to model displaced fractured bones, the extracted contours should first be reduced to their original anatomical position on the X-rays before further processing. Another option is to split the developed SSM into fracture fragments, and use these partial SSMs to reconstruct the 3D fragments in line with work from *e.g.* Schumann *et al* (2016) [103] and Gong *et al* (2009) [104]. Subsequently, the reconstructed displaced bone fragments could also be automatically reduced to their anatomical position, either using ICP methods or fracture line matching [9], [10], [105]–[110].

Additionally, the workflow is not fully automated yet – manual indications of bone contours and fracture lines are required to construct the 3D geometries. Furthermore, the workflow requires assumptions regarding the X-ray setup used to acquire the X-ray images. These limitations could be addressed by using an SSAM for pose and shape optimization (rather than an SSM) and by employing *e.g.*, canny edge or active snake algorithms for fracture line detection [111], [112].

Lastly, the obtained fractured bone geometries and FE results of the tested patient case are not yet validated in the current study. In future studies, a larger test dataset should be used to validate the success of the workflow. For these test cases, CT scans should also be available such that the true 3D bone fragment geometries are known. Additionally, IFMs and/or healing outcomes of the test cases could be used for validation of the FE results.

5 CONCLUSIONS

In this study, a semi-automated computational simulation workflow was established to determine the mechanical environment of a fixated tibial fracture based on 2D X-ray images and patient characteristics. Currently, such a biomechanical analysis is lacking in the preoperative planning of tibial fracture fixation surgeries, which have high revision and non-union rates of up to 15% and 23% respectively [5], [9]. The established workflow consisted of three main steps, *i.e.* (1) estimation of the intact 3D bone shape based on two orthogonal X-rays and patient characteristics using an SSM of the tibia, (2) modelling of the fracture lines as detected on the X-rays in the intact 3D bone shape, and (3) FE analysis of the fixated fracture using the automatically created geometries. The main findings of this study can be summarized as follows:

- An SSM of the healthy tibia was established based on CT scans of 25 subjects (15 male, age = 60 ± 5.5 ; 10 female, age = 51 ± 7.1) and the first five shape modes captured 90% of the total shape variation in the training cohort. Significant correlations were found between the first shape mode, which described shape changes in the tibial length, and patient gender ($r = .69$; $p < .001$), age ($r = .55$; $p < .001$), weight ($r = .38$; $p < .001$), and height ($r = .73$; $p < .001$), in line with previous studies [40], [83]–[86].
- Based on patient characteristics and two orthogonal X-rays, the intact shape of an unfractured unseen tibia could be reconstructed with a mean error of 0.81 mm and a maximum error of 4.22 mm. The highest reconstruction errors were found on the lateral tibial plateau and tibiotalar articular surface.
- FE analysis of an axially loaded (800 N) tibia with a spiral diaphyseal fracture fixated with a locking plate, predicted compressive strains in the fracture region in a range reported to be optimal for bone formation (0-10%; median: 2%) [13]. The magnitude of the compressive strains was predicted to increase further away from the fixation plate as compared to nearer to the plate. A strong effect of screw positioning around the fracture zone was determined: increasing the fixation working length by 13 mm increased the predicted compressive strains by more than 10 times. Additionally, the callus tissue near the plate was predicted to be under tension in this scenario. Increasing the flexibility of the locking plate by using a magnesium plate, lead to an increase of the compressive strains by 185%. Such excessive strains could lead to a high level of fibrous tissue formation and potentially delay healing or non-union [61]. These results were in line with results reported in previous studies [11], [15], [61], [90], [91].

Such a workflow could potentially be used to predict the healing potential of the fracture considering the chosen osteosynthesis and patient-specific weight-bearing input. This might allow for better informed preoperative planning of bone fracture fixation surgery. It was shown to be feasible to develop such models using readily available clinical imaging data that

is routinely collected prior to bone fracture fixation. While the presented results are in line with previously reported studies, further validation of the established workflow is warranted. Furthermore, future work should focus on fully automating the suggested workflow.

6 APPENDICES

Appendix A: Segmentation methods in 3D Slicer

To segment the tibia bones from the acquired CT scans, the following steps were taken in 3D Slicer²⁷ (Version 4.11):

1. Load DICOMs,
2. Thresholding: min (~266) – max (~3000) Hounsfield Units,
3. Manual separation from femur/tibia/talus using erase functions,
4. Islands - Keep selected island,
5. Smoothing - closing: fill holes - kernel size 1-2-3-4 mm,
6. Manual closing of bone borders using paint function,
7. Smoothing - fill holes - kernel size 1-2-3-4 mm,
8. Logical operators – invert,
9. Islands - Keep largest island,
10. Logical operators – invert,
11. Smoothing - median - kernel size 1-2-3-4 mm.

²⁷ <https://www.slicer.org/>

Appendix B: SSM-to-patient fitting and fracture line back-projection

SSM projection

To perform the SSM-to-patient fitting, 2D projections in anteroposterior (AP) and mediolateral (ML) planes were made of the 3D SSM realizations in each iteration of the fitting algorithm. In this section, the used equations to generate these projections are detailed. The assumed projection setup is depicted in **Figure B-3**.

An initial educated guess for the distance between the centroid of the tibia and the imager (object-imager distance (OID)) in AP view was set to 9 cm for the test case, considering the usual position of the tibia in an X-ray set-up and a typical thickness of the calf. Using the ratio of the measured bone lengths from AP and ML X-rays and the assumed X-ray projection setup, an initial educated guess for the OID in ML view was computed using:

$$\begin{aligned}
 SID &= SOD_{AP} + OID_{AP} = SOD_{ML} + OID_{ML} = 1000mm \\
 OID_{AP} &= 90mm \\
 r_{SOD} &= length_{AP} / length_{ML} \\
 OID_{ML} &= SID - \left(\frac{SID \cdot length_{true}}{length_{ML}} \right) \\
 &= SID - \left(\frac{SID \cdot \frac{SOD_{AP} \cdot length_{AP}}{SID}}{length_{ML}} \right) \\
 &= SID - (SOD_{AP} \cdot r_{SOD}) \\
 &= 1000 - (910 \cdot r_{SOD})
 \end{aligned} \tag{B1}$$

Where SID is the source-imager-distance, SOD is the source-object-distance and r is the ratio of measured bone lengths. Planar projections of the 3D SSM shape realization (*i.e.*, point cloud) onto AP and ML planes were established using the perspective transform of a set of points that is depicted in **Figure B-1**. Equations were adapted from Pyakurel (2020) [58].

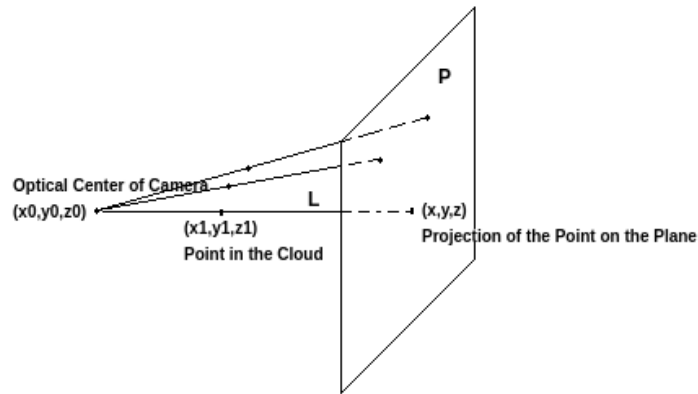


Figure B-1: Projection of a point in a point cloud onto a plane. *Note:* From [58].

The plane P is defined by the general plane equation $Ax + By + Cz + D = 0$. **Figure B-1** shows that the projection of a point (x_1, y_1, z_1) onto the plane P is the intersection between the plane

P and the line L which passes through the optical centre (x_0, y_0, z_0) and the given point. This line L is given by:

$$\begin{aligned} x &= x_1 + at \\ y &= y_1 + bt \\ z &= z_1 + ct \end{aligned} \quad (\text{B2})$$

with a, b, c the direction cosines of the line L , given by:

$$\begin{aligned} a &= \cos\alpha = \frac{x_1 - x_0}{\sqrt{(x_1 - x_0)^2 + (y_1 - y_0)^2 + (z_1 - z_0)^2}} \\ b &= \cos\beta = \frac{y_1 - y_0}{\sqrt{(x_1 - x_0)^2 + (y_1 - y_0)^2 + (z_1 - z_0)^2}} \\ c &= \cos\gamma = \frac{z_1 - z_0}{\sqrt{(x_1 - x_0)^2 + (y_1 - y_0)^2 + (z_1 - z_0)^2}} \end{aligned} \quad (\text{B3})$$

with α, β, γ the angles of the lines passing through each of the points. Solving for t at the intersection between L and P gives us:

$$\begin{aligned} A(x_1 + at) + B(y_1 + bt) + C(z_1 + ct) + D &= 0 \\ \Rightarrow t &= -\frac{Ax_1 + By_1 + Cz_1 + D}{aA + b/b + cC} \end{aligned} \quad (\text{B4})$$

Plugging this into equations (B2) gives us:

$$\begin{aligned} x &= x_1 - a \cdot \frac{Ax_1 + By_1 + Cz_1 + D}{aA + b/b + cC} \\ y &= y_1 - b \cdot \frac{Ax_1 + By_1 + Cz_1 + D}{aA + b/b + cC} \\ z &= z_1 - c \cdot \frac{Ax_1 + By_1 + Cz_1 + D}{aA + b/b + cC} \end{aligned} \quad (\text{B5})$$

For AP projections of the point cloud PCD , the plane parameters A, B, C, D and the optical centre (x_0, y_0, z_0) were set to:

$$\begin{aligned} A_{AP} &= 0 \\ B_{AP} &= -1 \\ C_{AP} &= 0 \\ D_{AP} &= \text{centroid}(PCD) \cdot y + \text{OID}_{AP} \\ x_{0,AP} &= \text{centroid}(PCD) \cdot x \\ y_{0,AP} &= D - \text{SID} \\ z_{0,AP} &= \text{centroid}(PCD) \cdot z \end{aligned} \quad (\text{B6})$$

For ML projections of the point cloud PCD , the plane parameters A, B, C, D and the optical centre (x_0, y_0, z_0) were set to:

$$\begin{aligned}
 A_{ML} &= -1 \\
 B_{ML} &= 0 \\
 C_{ML} &= 0 \\
 D_{ML} &= \text{centroid}(PCD).x - OID_{ML} \\
 x_{0,ML} &= D + SID \\
 y_{0,ML} &= \text{centroid}(PCD).y \\
 z_{0,ML} &= \text{centroid}(PCD).z
 \end{aligned} \tag{B7}$$

To perform the SSM-to-patient fitting, the following figures and equations were used:

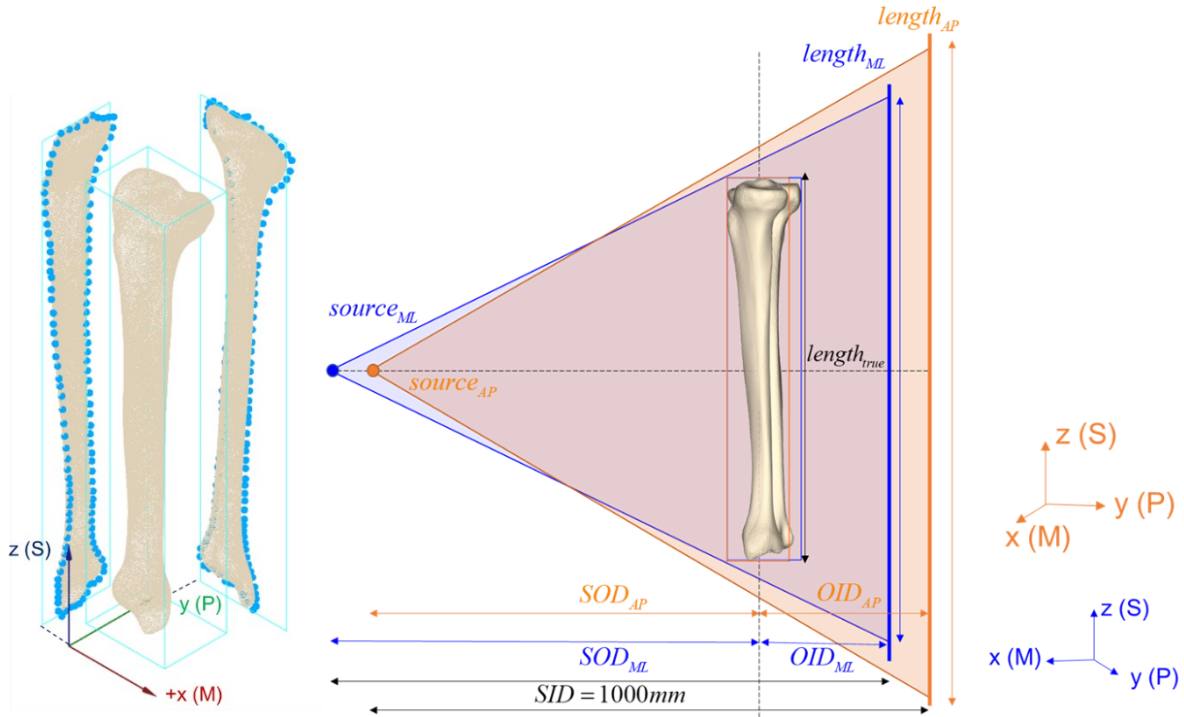


Figure B-2: Definition of the reliable, repeatable coordinate system with respect to the 3D tibia instance and its projections. x-axis = 2nd principal axis. y-axis = 3rd principal axis. z-axis = 1st principal axis. Origin: most inferior, lateral, anterior point of 2D projections of 3D shape.

Figure B-3: Assumed X-ray projection setup for anteroposterior (AP) in orange and mediolateral (ML) in blue. SOD: source-object-distance, OID: object-imager-distance, SID: source-imager-distance, S: superior, P: posterior, M: medial.

1. Initialization of the shape parameters b_s using the multilinear regression models described in section 2.1.2 using equation (10).
2. Optimize shape parameters b_s such that AP and ML projections of the SSM

realization $\mathbf{x}_1 = \bar{\mathbf{x}} + \sum_{s=1}^c b_s \phi_s$ have equal bounding box dimensions as AP and ML X-ray contours \mathbf{X}_{AP} and \mathbf{X}_{ML} . To achieve this, the following steps were performed in each iteration:

- a. Position SSM realization in the repeatable coordinate system as depicted in **Figure B-2** with neutral pose in X-ray setup as depicted in **Figure B-3** using equations (B1),
 - b. Project SSM realization in AP and ML planes using equations (B5) and parameters (B6) and (B7) for AP and ML projections respectively, *i.e.*, $proj_{AP}(\mathbf{x}_{b_s})$ and $proj_{ML}(\mathbf{x}_{b_s})$,
 - c. Compute bounding box dimensions of AP and ML projections using PCA, *i.e.*, $BB_{dim}(proj_{AP}(\mathbf{x}_{b_s}))$ and $BB_{dim}(proj_{ML}(\mathbf{x}_{b_s}))$,
 - d. Minimize cost function:

$$\min_{b_s} |BB_{dim}(\mathbf{X}_{AP}) - BB_{dim}(proj_{AP}(\mathbf{x}_{b_s})) + BB_{dim}(\mathbf{X}_{ML}) - BB_{dim}(proj_{ML}(\mathbf{x}_{b_s}))| \quad (B8)$$
3. Transform AP and ML X-ray contours to coordinate system as depicted in **Figure B-2** using bounding boxes and assumed X-ray setup as depicted in **Figure B-3**:
 - a. Input coordinates: x and z for AP, y and z for ML X-ray contours
 - b. Translations: align bounding box centres, *i.e.*:

$$\begin{aligned} \mathbf{t}_{AP} &= -\mathbf{BB}_{center}(\mathbf{X}_{AP}) + \mathbf{BB}_{center}(proj_{AP}(\mathbf{x}_1)) \\ \mathbf{t}_{ML} &= -\mathbf{BB}_{center}(\mathbf{X}_{ML}) + \mathbf{BB}_{center}(proj_{ML}(\mathbf{x}_1)) \end{aligned} \quad (B9)$$

- c. Rotation: align first principal components of bounding boxes of AP and ML X-ray contours with bounding boxes of AP and ML projections of SSM realization, *i.e.*:

$$\begin{aligned} \theta_{AP} &= \cos^{-1}(BB_1(\mathbf{X}_{AP}) \cdot BB_1(proj_{AP}(\mathbf{x}_1))) \\ \theta_{ML} &= \cos^{-1}(BB_1(\mathbf{X}_{ML}) \cdot BB_1(proj_{ML}(\mathbf{x}_1))) \end{aligned} \quad (B10)$$

- d. y and z coordinates for AP and ML respectively:

$$\begin{aligned} y_{AP} &= centroid(\mathbf{x}_1) \cdot y + OID_{AP} \\ z_{ML} &= centroid(\mathbf{x}_1) \cdot z + OID_{ML} \end{aligned} \quad (B11)$$

4. Refine shape parameters b_s and pose \mathbf{T} such that the distances between the concave hulls of AP and ML projections of the transformed SSM realization

$$\mathbf{T}\mathbf{x}_{b_s} = \mathbf{T}(\bar{\mathbf{x}} + \sum_{s=1}^c b_s \phi_s) \text{ and the AP and ML X-ray contours } \mathbf{X}_{AP} \text{ and } \mathbf{X}_{ML} \text{ are minimal.}$$

To achieve this, the following steps were performed in each iteration:

- a. Position SSM realization in the repeatable coordinate system as depicted in **Figure B-2** with pose \mathbf{T} in X-ray setup as depicted in **Figure B-3** using equations (B1)
- b. Project SSM realization in AP and ML planes using equations (B5) and parameters (B6) and (B7) for AP and ML projections respectively, *i.e.*, $proj_{AP}(\mathbf{T}\mathbf{x})$ and $proj_{ML}(\mathbf{T}\mathbf{x}_{b_s})$,

- c. Compute the concave hull points of AP and ML projections of the transformed SSM projections $CH(proj_{AP}(\mathbf{T}\mathbf{x}_{b_s}))$ and $CH(proj_{ML}(\mathbf{T}\mathbf{x}_{b_s}))$ using the `concavehull`²⁸ function with a chi factor of 0.01,
- d. Optimize b_s and \mathbf{T} such that the root-mean-square of Euclidian distances between the AP and ML concave hull points $CH(proj_{AP}(\mathbf{T}\mathbf{x}_{b_s}))$ and $CH(proj_{ML}(\mathbf{T}\mathbf{x}_{b_s}))$ and the AP and ML X-ray contour points \mathbf{X}_{AP} and \mathbf{X}_{ML} is minimized, *i.e.*:
 - i. For each point $\mathbf{p}_{AP,i}^{b_s,\mathbf{T}}$ and $\mathbf{p}_{ML,j}^{b_s,\mathbf{T}}$ in \mathbf{X}_{AP} and \mathbf{X}_{ML} respectively, find the closest point $\mathbf{q}_{AP,i}^{b_s,\mathbf{T}}$ and $\mathbf{q}_{ML,j}^{b_s,\mathbf{T}}$ in $CH(proj_{AP}(\mathbf{T}\mathbf{x}_{b_s}))$ and $CH(proj_{ML}(\mathbf{T}\mathbf{x}_{b_s}))$ respectively using the `Open3D`²⁹ library,
 - ii. Compute Euclidian distances between the matched point pairs $d(\mathbf{p}_{AP,i}^{b_s,\mathbf{T}}, \mathbf{q}_{AP,i}^{b_s,\mathbf{T}})$ and $d(\mathbf{p}_{ML,j}^{b_s,\mathbf{T}}, \mathbf{q}_{ML,j}^{b_s,\mathbf{T}})$,
 - iii. Minimize cost function:

$$\min_{b_s, \mathbf{T}} \sqrt{\frac{\sum_{i,j=1}^{N,M} d(\mathbf{p}_{AP,i}^{b_s,\mathbf{T}}, \mathbf{q}_{AP,i}^{b_s,\mathbf{T}}) + d(\mathbf{p}_{ML,j}^{b_s,\mathbf{T}}, \mathbf{q}_{ML,j}^{b_s,\mathbf{T}})}{N + M}} \quad (\text{B12})$$

Back-projection

To be able to introduce the obtained fracture lines into the intact tibia model, they were first transformed to the coordinate system of the AP and ML projections (x - and z -coordinates for AP, y - and z -coordinates for ML) as depicted in **Figure B-2**. This was done using transformations obtained from the bounding boxes of the AP and ML X-ray contours \mathbf{X}_{AP} and \mathbf{X}_{ML} , and the first SSM shape realization \mathbf{x}_1 retrieved from the bounding box fitting, *i.e.*:

$$\begin{aligned} \mathbf{t}_{AP} &= -\mathbf{BB}_{center}(\mathbf{X}_{AP}) + \mathbf{BB}_{center}(proj_{AP}(\mathbf{x}_1)) \\ \mathbf{t}_{ML} &= -\mathbf{BB}_{center}(\mathbf{X}_{ML}) + \mathbf{BB}_{center}(proj_{ML}(\mathbf{x}_1)) \\ \theta_{AP} &= \cos^{-1}(\mathbf{BB}_1(\mathbf{X}_{AP}) \bullet \mathbf{BB}_1(proj_{AP}(\mathbf{x}_1))) \\ \theta_{ML} &= \cos^{-1}(\mathbf{BB}_1(\mathbf{X}_{ML}) \bullet \mathbf{BB}_1(proj_{ML}(\mathbf{x}_1))) \end{aligned} \quad (\text{B13})$$

Their y - and x -coordinates for AP and ML points respectively, were obtained from the assumed X-ray setup outlined in section 2.1.3.3.2 using:

$$\begin{aligned} y_{AP} &= \mathit{centroid}(\mathbf{x}_1).y + \mathit{OID}_{AP} \\ z_{ML} &= \mathit{centroid}(\mathbf{x}_1).z + \mathit{OID}_{ML} \end{aligned} \quad (\text{B14})$$

Next, the projected anterior and posterior fracture line coordinates were back-projected to their unprojected position in 3D space. This was done using inverse projection geometry (see

²⁸ <https://github.com/senhorsolar/concavehull>

²⁹ http://www.open3d.org/docs/latest/tutorial/Basic/icp_registration.html

Figure B-4). However, during 3D/2D projection, depth information (the y -coordinate in the case of AP projection) is lost. The depth (*i.e.*, y -coordinates) of the anterior fracture line was therefore assumed to be equal to the y -coordinate of the most anterior edge of the tibial diaphysis at the level of the fracture in ML view ($y_{1,A} = \mathbf{d}_{ML}[0]$). For the posterior fracture line, the y -coordinates were set to the y -coordinate of the most posterior edge of the tibial diaphysis at the level of the fracture in ML view ($y_{1,P} = \mathbf{d}_{ML}[1]$).

As can be deduced from **Figure B-4**, the back-projected z -coordinate z_1 is obtained by:

$$z_1 = \frac{z - z_0}{y - y_0} \cdot (y_1 - y_0) + z_0 \quad (\text{B15})$$

Equivalently, the x -coordinate x_1 is obtained using:

$$x_1 = \frac{x - x_0}{y - y_0} \cdot (y_1 - y_0) + x_0 \quad (\text{B16})$$

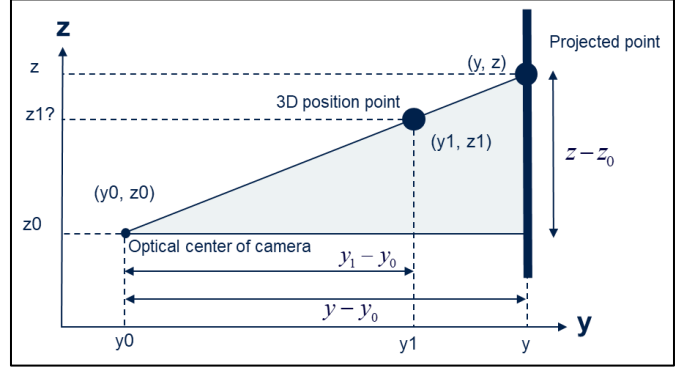


Figure B-4: Inverse projection geometry used for back-projection of AP projected fracture line points. Geometry to obtain x -coordinate is equivalent. y_1 assumed to be known.

Using the back-projected fracture line coordinates \mathbf{FL}_A and \mathbf{FL}_P , and the bounding box $BB(\mathbf{T}\mathbf{x}_{b_s,final})$ of the intact 3D bone shape, polyhedrons were automatically constructed that were used to crop the intact 3D bone shape in two fracture fragments (see **Figure B-5**). The anterior fracture line was used to crop the point cloud until halfway across the tibial shaft at the level of the fracture in the y -direction, while the posterior fracture line was used for the posterior half, *i.e.*:

$$\begin{aligned} y_{A,min} &= BB_{min}(\mathbf{T}\mathbf{x}_{b_s,final}) \cdot y \\ y_{A,max} &= \frac{1}{2}(\mathbf{d}_{ML}[0] + \mathbf{d}_{ML}[1]) \\ y_{P,min} &= \frac{1}{2}(\mathbf{d}_{ML}[0] + \mathbf{d}_{ML}[1]) \\ y_{P,max} &= BB_{max}(\mathbf{T}\mathbf{x}_{b_s,final}) \cdot y \end{aligned} \quad (\text{B17})$$

with \mathbf{d}_{AP} and \mathbf{d}_{ML} points indicated by the user on the outer edges of the tibial diaphysis at the level of the fracture on the AP and ML X-rays respectively. $y_{A,min}$ and $y_{A,max}$ represent the minimum and maximum cropping depth of the anterior fracture line polyhedron while $y_{P,min}$ and $y_{P,max}$ represent the minimum and maximum cropping depth of the posterior fracture line polyhedron.

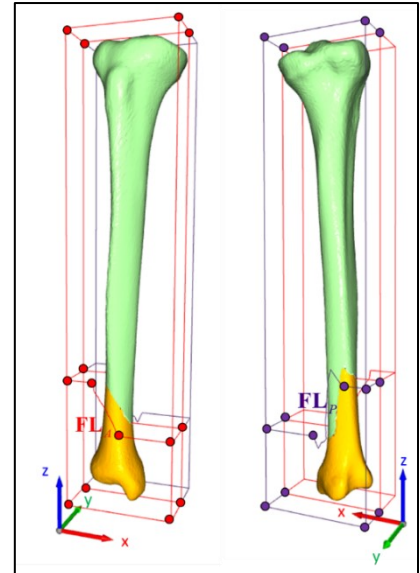


Figure B-5: Constructed polyhedrons used to clip intact 3D bone shape into two bone fracture fragments. \mathbf{FL}_A : anterior fracture line; \mathbf{FL}_P : posterior fracture line.

Appendix C: DRR Generation in 3D Slicer and pre-processing

The performance of the SSM-to-patient fitting algorithm was tested on an intact validation case. Because no X-rays of this case were available, DRRs were first generated using the CT scans of this case using 3D Slicer. This was done by following the steps below:

1. Load CT volume (THIN_BONE_L_EXT.nrrd)
2. Crop volume such that the left tibia is omitted from the CT:
 - a. Crop Volume module
 - b. Input Volume: THIN_BONE_L_EXT
 - c. Input ROI:
 - d. Dimensions: 256, 512, 1494 (only change LR dimensions!)
 - e. Untick interpolated cropping
 - f. Output ROI: THIN_BONE_L_EXT_cropped
3. Segment the right tibia using steps detailed in Segmentation methods in 3D Slicer
4. DRR generation module (all in LPS coordinate system)
 - a. CT Input Volume: THIN_BONE_L_EXT_cropped
 - b. DRR output volume - create new volume as – DRR_frontal
 - c. SAD: 910
 - d. SID: 1000
 - e. View-up-vector: 0,0,1
 - f. Normal vector
 - i. For frontal (from posterior to anterior) 0,-1,0
 - ii. For lateral (from right to left): 1,0,0
 - g. Isocenter position: -113.596, 168.470, -1100
 - h. Resolution: 2466, 3040
 - i. Spacing: 0.14, 0.14
 - j. Image window: 0,0,2465,3039
 - k. Autoscale range: 0, 255
 - l. Threshold below:
 - m. Exposure type: uniform
 - n. Leave other settings as default
5. In python interactor:

```
volumeNode = slicer.util.getNode("DRR_frontal")
voxels = slicer.util.arrayFromVolume(volumeNode)
np.save('DRR_frontal.npy', voxels)
```

```
volumeNode = slicer.util.getNode("DRR_lateral")
voxels = slicer.util.arrayFromVolume(volumeNode)
np.save('DRR_lateral.npy', voxels)
```

The generated DRRs were pre-processed through a custom-made GUI, equivalently to the patient case as detailed in section 2.1.3.2. The pre-processed DRRs are shown in **Figure C-1**.

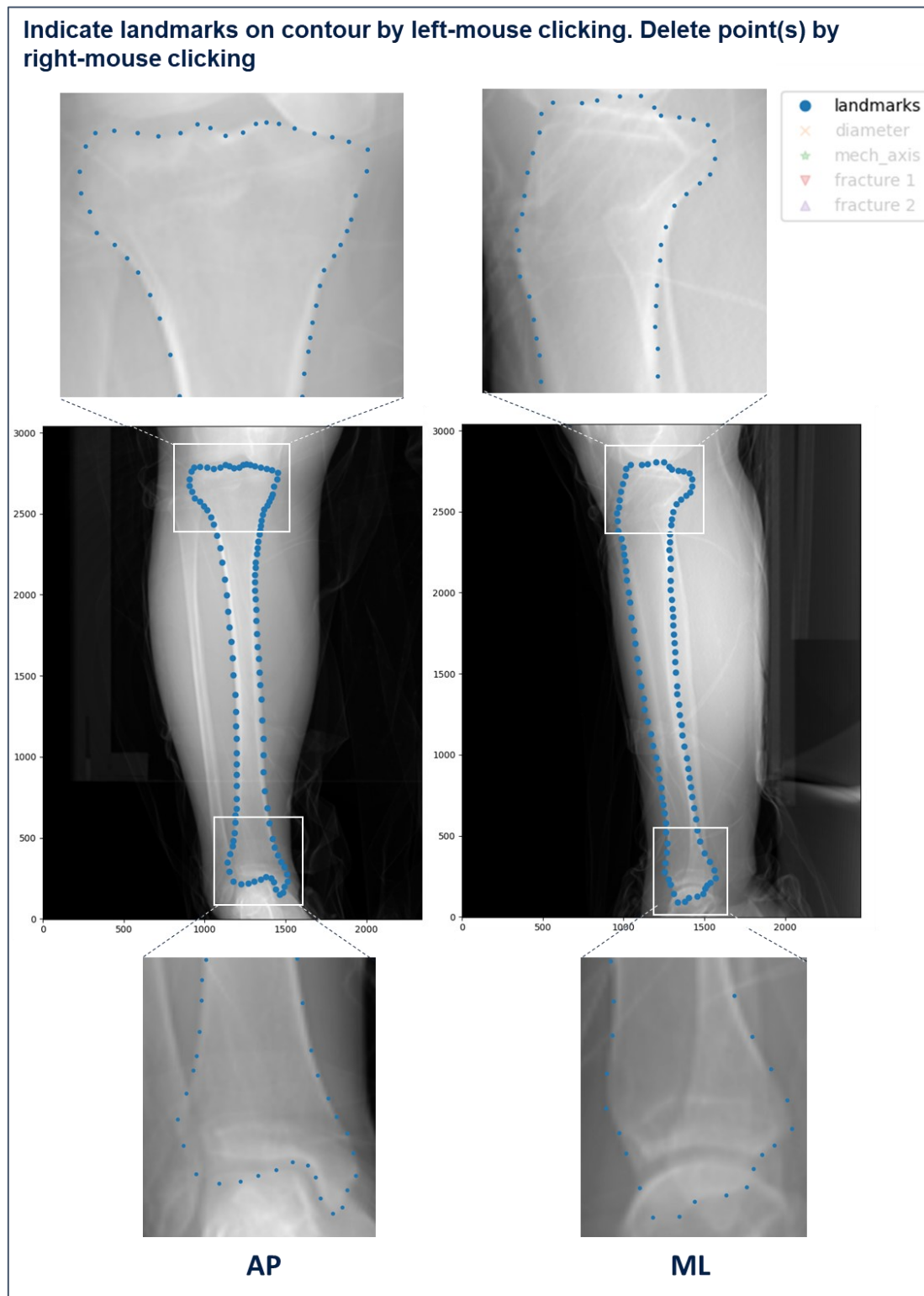


Figure C-1: Custom-made GUI that requires the user to indicate the contour points on the AP and ML X-rays. AP: anteroposterior, ML: mediolateral. X-rays are DRRs acquired from the CT scans of the validation case from the New Mexico database.

Appendix D: Postprocessing in Meshmixer

The bone fracture fragments were post-processed in Autodesk Meshmixer³⁰ (Version 3.5.474, Autodesk, Inc., California, USA).

Fragment postprocessing

The fracture lines were smoothed to prevent meshing issues in a later stage. Additionally, the fracture fragment meshes were closed, since the clipping in the previous step creates a hole in the mesh. This was done using the following steps:

1. Import bone fracture fragment STL file
2. Select all – edit – flip normals
3. Select all – modify – smooth boundary
 - a. Smoothness: 100
 - b. Preserve shape: 100
 - c. Iterations: 30
 - d. Border rings: 2
 - e. Repeat these steps once
4. Inspector – Hole fill mode: flat fill – Small thresh: 0.01 mm – Auto Repair All
5. Export – STL ASCII Format

Bone marrow surface reconstruction

The bone marrow (and thus the inner cortical surface) was reconstructed by offsetting the outer cortical surface of the tibia by -5 mm in the direction normal to the bone surface. This was done using the following steps:

1. Import intact 3D bone shape STL file
2. Select all – edit – flip normals
3. Select all – edit – off-set
 - a. Distance: -5mm
 - b. Accuracy: 50
 - c. Regularity: 25
 - d. Soft Transition: 0mm
4. While mesh is still selected: edit – Separate
5. Select bone marrow mesh – edit – flip normals
6. Export – STL ASCII Format

Callus geometry reconstruction

A callus geometry was created in Meshmixer by selecting the bone surface around the fracture region and extruding this surface in all directions by 2 mm in the direction normal to the surface. To do this, the following steps were taken:

³⁰ <https://meshmixer.com/>

1. Import intact 3D bone shape and fracture fragment STL files
2. Make sure the fracture lines are visible on the intact 3D bone shape
3. Select – Brush mode – size: 25 mm
4. Manually select faces surrounding the fracture lines
5. Modify – optimize boundary
6. Modify – smooth boundary
 - a. Smoothness: 100
 - b. Preserve shape: 100
 - c. Iterations: 30
 - d. Border rings: 2
 - e. Repeat these steps once
7. Edit – separate
8. Hide all other geometries such that just the separated faces are active
6. Analysis – Inspector – Hole Fill Mode: Flat Fill– Small thresh: 0.01 mm – Auto Repair All
7. Edit – Generate face groups – edge angle - angle threshold: 12
8. Select the most superior surface – Edit – Extrude
 - a. Offset: 5 mm
 - b. Harden: 0
 - c. Density: 20
 - d. Direction: y-axis
9. Select all – Deform – Smooth
 - a. Smoothing Type: Shape preserving
 - b. Smoothing: 1
 - c. Smoothing scale: 4
 - d. Constraint Rings: 3
 - e. Repeat these steps once
10. Select all – Edit – Offset
 - a. Distance: 2 mm
 - b. Accuracy: 100
 - c. Regularity: 25
 - d. Soft transition: 0
11. Export – STL ASCII Format

Appendix E: Post-processing & assembly in SOLIDWORKS

The STL files of the fracture fragments, callus and reconstructed intact inner and outer cortical bone surfaces were further post-processed and assembled in SOLIDWORKS (Student Edition 2022, Dassault Systèmes, France).

Convert intact bone geometries to B-spline representations

First, the geometries were converted to 3D non-uniform rational B-spline (NURBS) representations. This was done using the following steps:

1. Import bone STL files as ScanTo3D objects:
 - a. Tools – Add-Ins – tick ScanTo3D
 - b. File – Open – select ScanTo3D Mesh Files – select file – Open
2. Tools – ScanTo3D- surface Wizard
 - a. Select mesh
 - b. Automatic creation
 - c. Surface detail – position slider in the middle
 - d. Update preview
 - e. Play with feature lines until there are no errors
 - i. Edit feature lines
 - ii. Relax feature lines
3. Save as – STEP

Extract fracture surface

To reconstruct a fracture gap with a uniform thickness of 4 mm, the fracture surface was extracted. This was done using the following steps:

1. Import lower fragment STL files as ScanTo3D objects:
 - a. Tools – Add-Ins – tick ScanTo3D
 - b. File – Open – select ScanTo3D Mesh Files – select file – Open
 - c. Tools – ScanTo3D- surface Wizard Select mesh
 - d. Guided creation
 - e. Split plane – None
 - f. Face Identification – move the sensitivity slider until the fracture surface is identified as a sub-mesh (see **Figure E-1**)
 - g. Surface Extraction – click fracture surface
 - h. Face Settings – Bspline

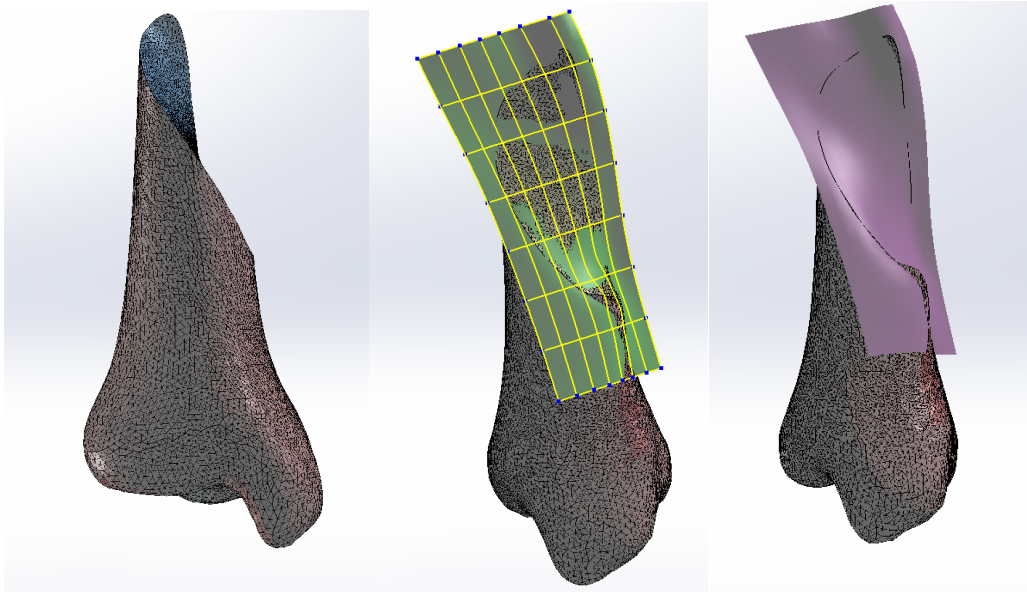


Figure E-1: Identified surfaces by the surface wizard in ScanTo3D in SOLIDWORKS (left) that was extracted and converted to B-spline surfaces (middle/right).

2. Save as – SOLIDWORKS part

Next, the extracted fracture surface (see **Figure E-1**) was used to create fracture fragment geometries with a uniform thickness by performing the steps below:

1. Open extracted fracture surface (BSpline)
2. Offset surface – 4 mm in the positive z-direction (see **Figure E-2**)

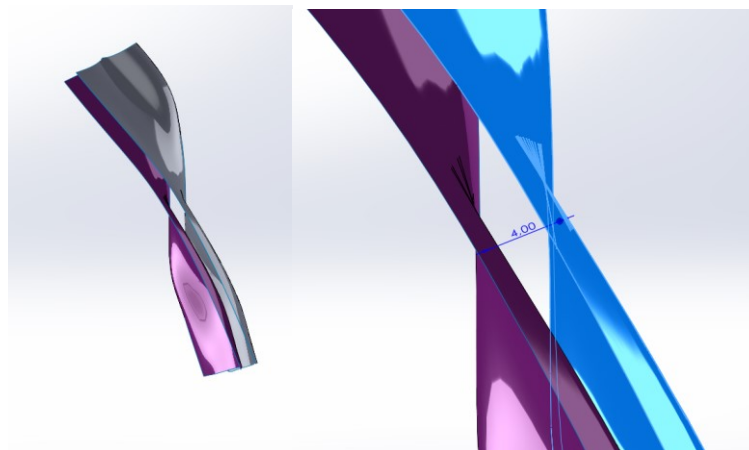


Figure E-2: Surface offset of 4 mm to create a uniform fracture gap.

3. Extend surface – 10 mm
4. Insert – part
 - a. Intact bone (BSPLINE)
 - b. Bone marrow (BSPLINE)
5. Split
 - a. Trim tools: both BSplines fracture surfaces
 - b. Target bodies:

- i. Intact bone
- ii. Bone marrow
- c. Resulting bodies: fracture fragments (upper + lower, cortical + marrow, see **Figure E-3** and **Figure E-4**)

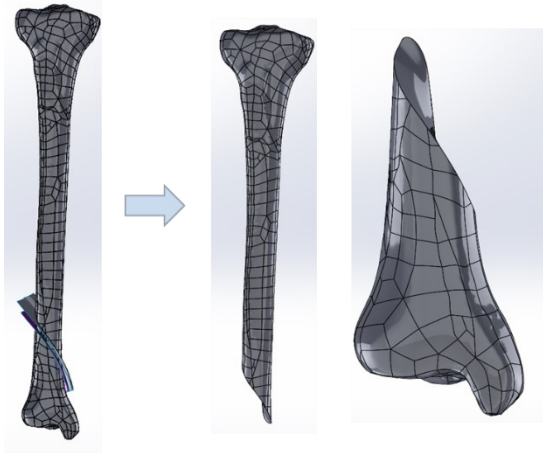


Figure E-3: Post-processed cortical bone fracture fragments.

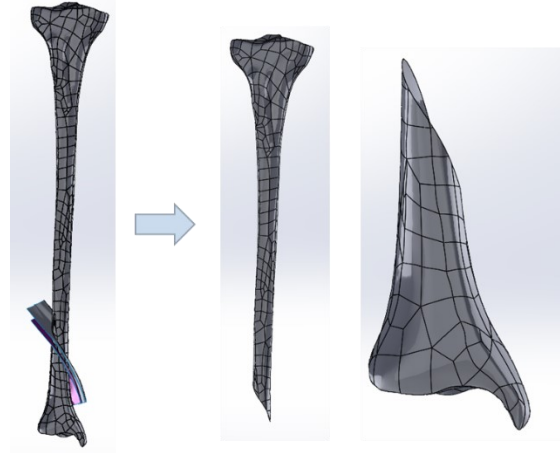


Figure E-4: Post-processed bone marrow fracture fragments.

6. Save bodies as – SOLIDWORKS parts

The locking plate used to fixate the fractured bone was drawn in SOLIDWORKS. This drawing was validated by using a segmented micro-CT scan of the implant. **Figure E-5** shows the Hausdorff distance map of the drawn tibial locking plate as compared to the segmented micro-CT scanned plate. It can be observed that the mean deviation from the scanned plate was 0.41 mm with a max deviation of 2.5 mm around the distal screw holes.

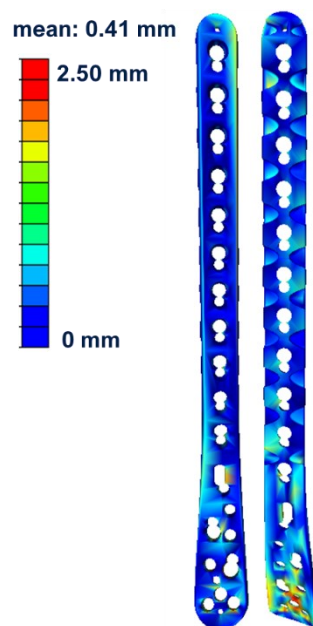


Figure E-5: Hausdorff distance map of drawn tibia locking plate as compared to segmented micro-CT scanned locking plate.

Lastly, the post-processed geometries were assembled, together with the locking plate and screws, according to the manufacturer's recommended surgical technique, using the postoperative X-rays of the patient case as a reference (see section 2.3.1). To do this, the following steps were taken:

1. New SOLIDWORKS Document
2. Assembly
3. Add components:
 - a. Split intact bone + trabecular bone (fix)
 - b. Callus (fix)
 - c. Right LCP tibia (float)
 - d. Screws (float)
4. Mate screws with screw holes using concentric constraints
5. Position plate + screw assembly onto bone using Move Component
6. Save as – STEP

Appendix F: Pre-processing & assembly in Abaqus/CAE

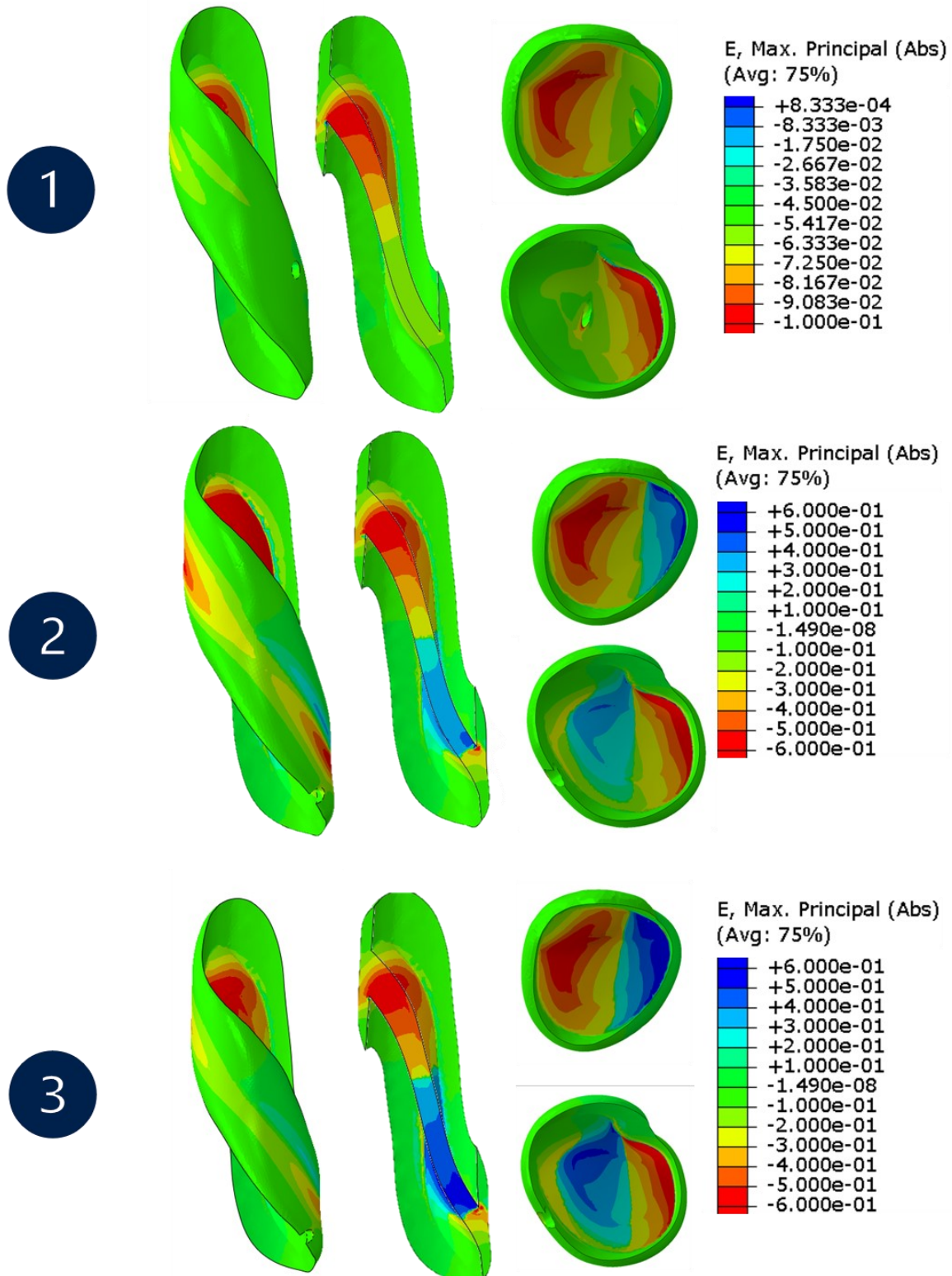
The final assembly was imported into Abaqus/CAE (version 2020, ABAQUS Inc, Dassault Systèmes, France). There, the parts were further processed using the following steps:

1. File – Import – Part – Assembly STEP file
 - a. Import all parts: create individual parts
2. Create sets for each part
3. Assembly:
 - a. Create Instance - Create instances from parts – select all parts
 - b. Merge/Cut Instances:
 - i. Merge: Geometry
 - ii. Intersecting Boundaries: Retain
 - iii. Instances: trabecular + cortical bone fragments
4. Part:
 - a. Select the merged bone part
 - b. Tools – Geometry Edit – Part: Convert to precise – Tighten Gaps
5. Assembly
 - a. Merge/Cut Instances: Merge
 - i. Merge: Geometry
 - ii. Intersecting Boundaries: Retain
 - iii. Instances: merged bone part + callus part
 - b. Merge/Cut Instances: Cut geometry
 - i. Instances: merged bone/callus part + screws
6. Create surfaces
 - a. For merged bone/callus part with screw holes:
 - i. Superior and inferior articular surfaces by selecting appropriate faces
 - ii. Screw hole surfaces (select by angle: 20 degrees)
 - b. For screws:
 - i. Screw head surfaces
 - ii. Screw tail surfaces
 - c. For plate
 - i. Screw hole surfaces
7. Assembly - Tools – Reference Point (2x)
 - a. Superior joint center (femur/tibia): $x = 60, y = 40, z = 450$
 - i. Using centroid of faces superior articular surface: 59.18,39.99,414.63
 - b. Inferior joint center (tibia/talus): $x = 51, y = 40, z = 10$
 - i. Using centroid of faces inferior articular surface: 51.39,39.72,37.85

The rest of the steps taken to build and analyse the models were detailed in section 2.3.2.

Appendix G: Details FE analysis results

In this study, five fixation scenarios were simulated. In scenario 1, the true postoperative fixation configuration was simulated. Screw positions, plate length and plate/screw material were altered in scenarios (2,3), (4) and (5) respectively (details in 2.3.1.1). The maximum absolute principal strain distributions of all these scenarios are shown in **Figure G-1**.



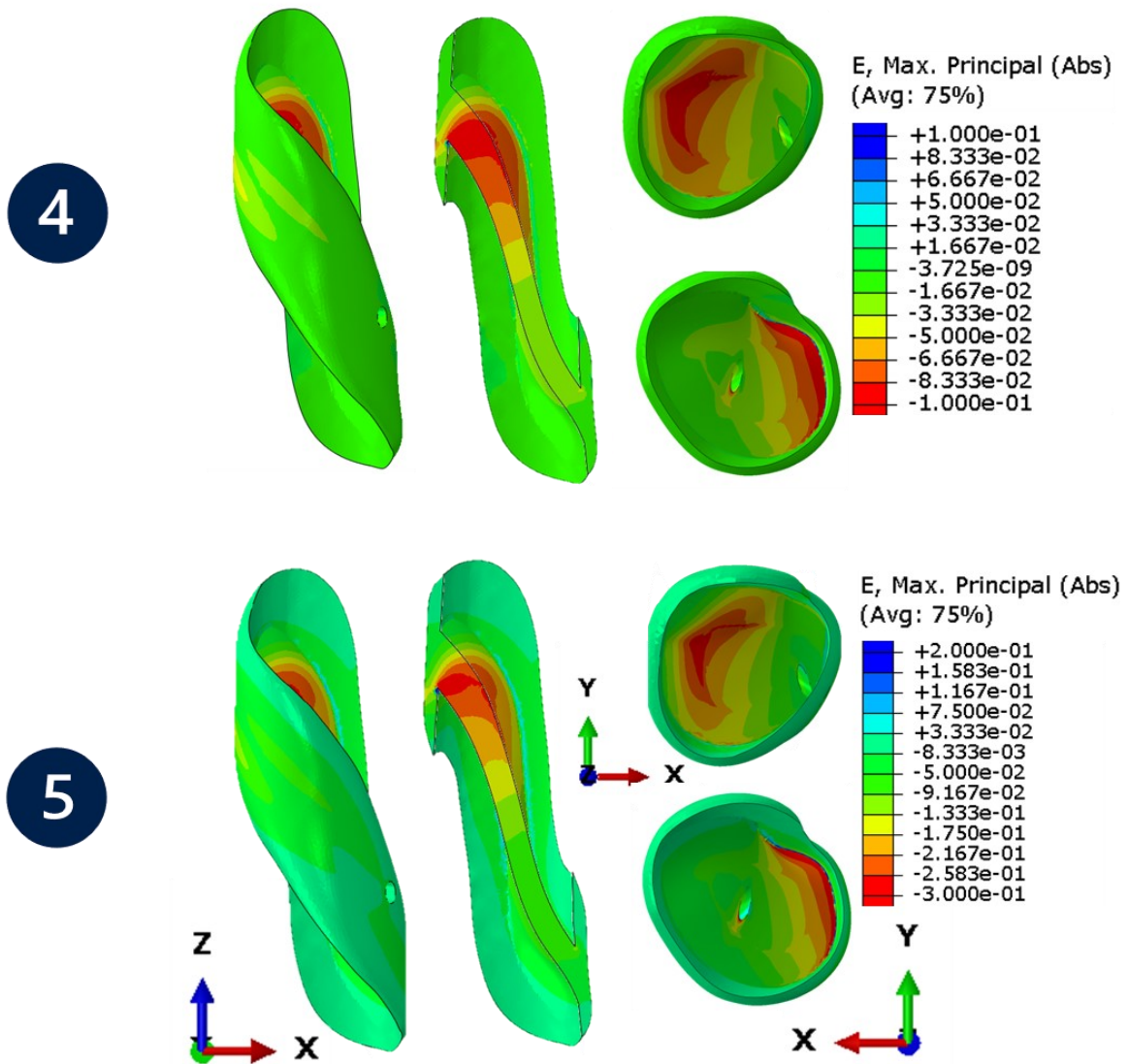


Figure G-1: Maximum absolute principal strain [-] distribution of the callus region within the fixated fractured tibia for the five different fixation scenarios.

7 BIBLIOGRAPHY

- [1] A. M. Wu *et al.*, "Global, regional, and national burden of bone fractures in 204 countries and territories, 1990–2019: a systematic analysis from the Global Burden of Disease Study 2019," *Lancet Heal. Longev.*, vol. 2, no. 9, pp. e580–e592, Sep. 2021, doi: 10.1016/S2666-7568(21)00172-0.
- [2] F. Borgström *et al.*, "Fragility fractures in Europe: burden, management and opportunities," *Arch. Osteoporos.*, vol. 15, no. 1, pp. 1–21, 2020, doi: 10.1007/s11657-020-0706-y.
- [3] C. L. Ekegren, E. R. Edwards, R. de Steiger, and B. J. Gabbe, "Incidence, costs and predictors of non-union, delayed union and mal-union following long bone fracture," *Int. J. Environ. Res. Public Health*, vol. 15, no. 12, p. 2845, 2018, doi: 10.3390/ijerph15122845.
- [4] P. V. Giannoudis, S. Gudipati, P. Harwood, and N. K. Kanakaris, "Long bone non-unions treated with the diamond concept: A case series of 64 patients," *Injury*, vol. 46, pp. S48–S54, Dec. 2015, doi: 10.1016/S0020-1383(15)30055-3.
- [5] S. K. Stewart, "Fracture non-union: A review of clinical challenges and future research needs," *Malaysian Orthopaedic Journal*, vol. 13, no. 2, pp. 1–10, 2019, doi: 10.5704/MOJ.1907.001.
- [6] C. M. Jones and C. E. Schmalbach, "Zygomaxillary Fractures," *Facial Plast. Surg. Clin. North Am.*, vol. 30, no. 1, pp. 47–61, 2022, doi: 10.1016/j.fsc.2021.08.004.
- [7] S. A. Olson, B. Furman, and F. Guilak, "Joint Injury and Post-Traumatic Arthritis," *HSS J.*, vol. 8, no. 1, pp. 23–25, Feb. 2012, doi: 10.1007/s11420-011-9247-7.
- [8] Y. Yoshii, T. Ogawa, A. Shigi, K. Oka, T. Murase, and T. Ishii, "Three-dimensional evaluations of preoperative planning reproducibility for the osteosynthesis of distal radius fractures," *J. Orthop. Surg. Res.*, vol. 16, no. 1, p. 131, 2021, doi: 10.1186/s13018-021-02278-9.
- [9] I. Kovler *et al.*, "Haptic computer-assisted patient-specific preoperative planning for orthopedic fractures surgery," *Int. J. Comput. Assist. Radiol. Surg.*, vol. 10, no. 10, pp. 1535–1546, 2015, doi: 10.1007/s11548-015-1162-9.
- [10] J. Z. Moolenaar, N. Tümer, and S. Checa, "Computer-assisted preoperative planning of bone fracture fixation surgery: A state-of-the-art review," *Front. Bioeng. Biotechnol.*, vol. 0, p. 1950, Oct. 2022, doi: 10.3389/FBIOE.2022.1037048.
- [11] J. Kenwright and T. Gardner, "Mechanical influences on tibial fracture healing," *Clin. Orthop. Relat. Res.*, vol. 355, no. SUPPL., 1998, doi: 10.1097/00003086-199810001-00019.
- [12] D. R. Suárez, "Theories of mechanically induced tissue differentiation and adaptation in the musculoskeletal system," *Ing. y Univ.*, vol. 20, no. 1, Dec. 2015, doi: 10.11144/JAVERIANA.IYU20-1.TMIT.
- [13] S. M. Perren, P. Matter, R. Rüedi, and M. Allgöwer, "Biomechanics of fracture healing after internal fixation," *Surg. Annu.*, vol. 7, pp. 361–390, 1975.
- [14] D. S. Elliott *et al.*, "A unified theory of bone healing and nonunion," *Bone Jt. J.*, vol.

- 98B, no. 7, pp. 884–891, 2016, doi: 10.1302/0301-620X.98B7.36061.
- [15] G. N. Duda, F. Mandruzzato, M. Heller, J. P. Kassi, C. Khodadadyan, and N. P. Haas, “Mechanical conditions in the internal stabilization of proximal tibial defects,” *Clin. Biomech.*, vol. 17, no. 1, pp. 64–72, Jan. 2002, doi: 10.1016/S0268-0033(01)00102-4.
- [16] Y. Matsuura, T. Rokkaku, T. Suzuki, A. R. Thoreson, K. N. An, and K. Kuniyoshi, “Evaluation of Bone Atrophy After Treatment of Forearm Fracture Using Nonlinear Finite Element Analysis: A Comparative Study of Locking Plates and Conventional Plates,” *J. Hand Surg. Am.*, vol. 42, no. 8, pp. 659.e1-659.e9, Aug. 2017, doi: 10.1016/j.jhsa.2017.03.041.
- [17] H. L. Dailey, P. Schwarzenberg, C. J. Daly, S. A. M. Boran, M. M. Maher, and J. A. Harty, “Virtual Mechanical Testing Based on Low-Dose Computed Tomography Scans for Tibial Fracture: A Pilot Study of Prediction of Time to Union and Comparison with Subjective Outcomes Scoring,” *J. Bone Jt. Surg. - Am. Vol.*, vol. 101, no. 13, pp. 1193–1202, Jul. 2019, doi: 10.2106/JBJS.18.01139.
- [18] D. P. Byrne, D. Lacroix, and P. J. Prendergast, “Simulation of fracture healing in the tibia: Mechanoregulation of cell activity using a lattice modeling approach,” *J. Orthop. Res.*, vol. 29, no. 10, pp. 1496–1503, 2011, doi: 10.1002/jor.21362.
- [19] H. J. Kim, S. H. Kim, and S. H. Chang, “Finite element analysis using interfragmentary strain theory for the fracture healing process to which composite bone plates are applied,” *Compos. Struct.*, vol. 93, no. 11, pp. 2953–2962, 2011, doi: 10.1016/j.compstruct.2011.05.008.
- [20] S. J. Shefelbine *et al.*, “Prediction of fracture callus mechanical properties using micro-CT images and voxel-based finite element analysis,” *Bone*, vol. 36, no. 3, pp. 480–488, 2005, doi: 10.1016/j.bone.2004.11.007.
- [21] D. Lacroix and P. J. Prendergast, “Three-dimensional simulation of fracture repair in the human tibia,” *Comput. Methods Biomech. Biomed. Engin.*, vol. 5, no. 5, pp. 369–376, 2002, doi: 10.1080/1025584021000025014.
- [22] T. Wehner, L. Claes, and U. Simon, “Internal loads in the human tibia during gait,” *Clin. Biomech.*, vol. 24, no. 3, pp. 299–302, Mar. 2009, doi: 10.1016/J.CLINBIOMECH.2008.12.007.
- [23] C. Zhang and K. K. McCully, “The Case for Measuring Long Bone Hemodynamics With Near-Infrared Spectroscopy,” *Front. Physiol.*, vol. 11, Dec. 2020, doi: 10.3389/FPHYS.2020.615977.
- [24] K. L. Moore, A. M. R. Agur, and A. F. Dalley, *Essential clinical anatomy*. Wolters Kluwer Health Philadelphia, 2015.
- [25] D. Paley, “Principles of Deformity Correction,” *Princ. Deform. Correct.*, 2002, doi: 10.1007/978-3-642-59373-4.
- [26] R. White and M. Camuso, “AO Surgery Reference: Tibial shaft,” *AO Foundation Surgery Reference*. AO Foundation.
- [27] J. H. Thompson, P. Koutsogiannis, and A. Jahangir, “Tibia Fractures Overview,” *StatPearls*, Aug. 2022.
- [28] G. Lloyd-Jone, “Trauma X-ray - lower limb,” *Radiology Masterclass*. Jul-2019.
- [29] M. A. J. Te Stroet, M. Holla, J. Biert, and A. Van Kampen, “The value of a CT scan compared to plain radiographs for the classification and treatment plan in tibial

- plateau fractures," *Emerg. Radiol.*, vol. 18, no. 4, p. 279, Aug. 2011, doi: 10.1007/S10140-010-0932-5.
- [30] M. Ronga, U. G. Longo, and N. Maffulli, "Minimally Invasive Locked Plating of Distal Tibia Fractures is Safe and Effective," *Clin. Orthop. Relat. Res.*, vol. 468, no. 4, p. 975, 2010, doi: 10.1007/S11999-009-0991-7.
- [31] G. Haidukewych, S. A. Sems, D. Huebner, D. Horwitz, and B. Levy, "Results of polyaxial locked-plate fixation of periarticular fractures of the knee. Surgical technique," *J. Bone Joint Surg. Am.*, vol. 90 Suppl 2 Pt 1, no. SUPPL. 2 PART 1, pp. 117–134, 2008, doi: 10.2106/JBJS.G.01086.
- [32] AO Foundation, "Locking Plate principles," *AO Surgery Reference*. AO Foundation Surgery Reference.
- [33] P. Cronier, G. Pietu, C. Dujardin, N. Bigorre, F. Ducellier, and R. Gerard, "The concept of locking plates," *Orthop. Traumatol. Surg. Res.*, vol. 96, no. 4 SUPPL., Jun. 2010, doi: 10.1016/J.OTSR.2010.03.008.
- [34] C. C. Joslin, S. J. Eastaugh-Waring, J. R. W. Hardy, and J. L. Cunningham, "Weight bearing after tibial fracture as a guide to healing," *Clin. Biomech. (Bristol, Avon)*, vol. 23, no. 3, pp. 329–333, Mar. 2008, doi: 10.1016/J.CLINBIOMECH.2007.09.013.
- [35] E. J. Strauss, R. Schwarzkopf, F. Kummer, and K. A. Egol, "The current status of locked plating: the good, the bad, and the ugly," *J. Orthop. Trauma*, vol. 22, no. 7, pp. 479–486, 2008, doi: 10.1097/BOT.0B013E31817996D6.
- [36] M. Leahy, "When locking plates fail," *AAOS Now*, 05-Jan-2010. [Online]. Available: <https://www.aaos.org/AAOSNow/2010/May/clinical/clinical4/?ssopc=1>. [Accessed: 18-Nov-2022].
- [37] N. Sarkalkan, H. Weinans, and A. A. Zadpoor, "Statistical shape and appearance models of bones," *Bone*, vol. 60, pp. 129–140, Mar. 2014, doi: 10.1016/j.bone.2013.12.006.
- [38] T. F. Cootes, C. J. Taylor, D. H. Cooper, and J. Graham, "Active Shape Models-Their Training and Application," *Comput. Vis. IMAGE Underst.*, vol. 61, no. 1, pp. 38–59, 1995.
- [39] H. Edgar, S. Daneshvari Berry, E. Moes, N. Adolphi, P. Bridges, and K. B. Nolte, "New Mexico Decedent Image Database (NMDID)." University of New Mexico, 2020, doi: 10.25827/5S8C-N515.
- [40] N. Tümer *et al.*, "Three-dimensional analysis of shape variations and symmetry of the fibula, tibia, calcaneus and talus," *J. Anat.*, vol. 234, no. 1, pp. 132–144, Jan. 2019, doi: 10.1111/joa.12900.
- [41] A. Fedorov *et al.*, "3D Slicer as an image computing platform for the Quantitative Imaging Network," *Magn. Reson. Imaging*, vol. 30, no. 9, pp. 1323–1341, Nov. 2012, doi: 10.1016/j.mri.2012.05.001.
- [42] P. Mitteroecker, P. Gunz, S. Windhager, and K. Schaefer, "A brief review of shape, form, and allometry in geometric morphometrics, with applications to human facial morphology," *Hystrix*, vol. 24, no. 1, pp. 59–66, May 2013, doi: 10.4404/hystrix-24.1-6369.
- [43] P. J. Besl and N. D. McKay, "A Method for Registration of 3-D Shapes," *IEEE Trans. Pattern Anal. Mach. Intell.*, vol. 14, no. 2, pp. 239–256, 1992, doi: 10.1109/34.121791.
- [44] P. Cignoni, M. Callieri, M. Corsini, M. Dellepiane, F. Ganovelli, and G. Ranzuglia,

- Fractures Treated with Fractures Treated wi," 2014.
- [61] S. Miramini, L. Zhang, M. Richardson, P. Mendis, and P. R. Ebeling, "Influence of fracture geometry on bone healing under locking plate fixations: A comparison between oblique and transverse tibial fractures," *Med. Eng. Phys.*, vol. 38, no. 10, pp. 1100–1108, 2016, doi: 10.1016/j.medengphy.2016.07.007.
- [62] C. Horn, S. Döbele, H. Vester, A. Schäffler, M. Lucke, and U. Stöckle, "Combination of interfragmentary screws and locking plates in distal meta-diaphyseal fractures of the tibia: a retrospective, single-centre pilot study," *Injury*, vol. 42, no. 10, pp. 1031–1037, Oct. 2011, doi: 10.1016/J.INJURY.2011.05.010.
- [63] M. Heyland, "Mechanotherapy of Bone Fracture : Adapted Fixation Conditions
Mechanotherapy of Bone Fracture : Adapted Fixation Conditions," no. August, 2019.
- [64] DePuy Synthes, "LCP Low Bend Medial Distal Tibia Plates 3.5 mm - Surgical Technique," *DePuy Orthopaedics*. [Online]. Available: [http://synthes.vo.llnwd.net/o16/LLNWMB8/INT Mobile/Synthes International/Product Support Material/legacy_Synthes_PDF/DSEM-TRM-1115-0544-2_LR.pdf](http://synthes.vo.llnwd.net/o16/LLNWMB8/INT%20Mobile/Synthes%20International/Product%20Support%20Material/legacy_Synthes_PDF/DSEM-TRM-1115-0544-2_LR.pdf). [Accessed: 12-Dec-2022].
- [65] M. K. A. Merino, S. C. Rahal, C. R. Ribeiro, and C. R. Padovani, "The effect of locked screw angulation on the biomechanical properties of the S.P.S. Free-Block plate," *Vet. Comp. Orthop. Traumatol.*, vol. 26, no. 2, pp. 117–122, 2013, doi: 10.3415/VCOT-12-03-0045.
- [66] A. MacLeod, A. H. R. W. Simpson, and P. Pankaj, "Experimental and numerical investigation into the influence of loading conditions in biomechanical testing of locking plate fracture fixation devices," *Bone Jt. Res.*, vol. 7, no. 1, pp. 111–120, Jan. 2020, doi: 10.1302/2046-3758.71.BJR-2017-0074.R2.
- [67] K. Takebe, A. Nakagawa, H. Minami, H. Kanazawa, and K. Hirohata, "Role of the fibula in weight-bearing.," *Clin. Orthop. Relat. Res.*, no. 184, pp. 289–292, Apr. 1984.
- [68] C. Perier-Metz, G. N. Duda, and S. Checa, "A mechanobiological computer optimization framework to design scaffolds to enhance bone regeneration," *Front. Bioeng. Biotechnol.*, vol. 10, p. 1622, Sep. 2022, doi: 10.3389/FBIOE.2022.980727/BIBTEX.
- [69] D. Blažević, J. Kodvanj, P. Adamović, D. Vidović, Z. Trobonjača, and S. Sabalić, "Comparison between external locking plate fixation and conventional external fixation for extraarticular proximal tibial fractures: a finite element analysis," *J. Orthop. Surg. Res.*, vol. 17, no. 1, p. 16, 2022, doi: 10.1186/s13018-021-02907-3.
- [70] Simulia, "Abaqus Analysis User's manual (V6.6)." [Online]. Available: [https://classes.engineering.wustl.edu/2009/spring/mase5513/abaqus/docs/v6.6/books/usb/default.htm?startat=pt09ch29s02aus114.html%7D,journal=%7BAbaqus Analysis User's manual \(V6.6\)%7D,publisher=%7BSimulia%7D%7D @misc%7Babaqus analysis user's manual \(v6.](https://classes.engineering.wustl.edu/2009/spring/mase5513/abaqus/docs/v6.6/books/usb/default.htm?startat=pt09ch29s02aus114.html%7D,journal=%7BAbaqus%20Analysis%20User%27s%20manual%20(V6.6)%7D,publisher=%7BSimulia%7D%7D%20@misc%7Babaqus%20analysis%20user%27s%20manual%20(v6))
- [71] L. E. Claes and C. A. Heigele, "Magnitudes of local stress and strain along bony surfaces predict the course and type of fracture healing," *J. Biomech.*, vol. 32, no. 3, pp. 255–266, 1999, doi: 10.1016/S0021-9290(98)00153-5.
- [72] V. Orassi, H. Fischer, G. N. Duda, M. Heiland, S. Checa, and C. Rendenbach, "In Silico Biomechanical Evaluation of WE43 Magnesium Plates for Mandibular Fracture Fixation," *Front. Bioeng. Biotechnol.*, vol. 9, Feb. 2022, doi:

- 10.3389/FBIOE.2021.803103/FULL.
- [73] "Online materials information resource," *MatWeb*. .
- [74] E. Schneider, M. C. Michel, M. Genge, K. Zuber, R. Ganz, and S. M. Perren, "Loads acting in an intramedullary nail during fracture healing in the human femur," *J. Biomech.*, vol. 34, no. 7, pp. 849–857, 2001, doi: 10.1016/S0021-9290(01)00037-9.
- [75] V. Vijayakumar, L. Marks, A. Bremmer-Smith, J. Hardy, and T. Gardner, "Load transmission through a healing tibial fracture," *Clin. Biomech.*, vol. 21, no. 1, pp. 49–53, Jan. 2006, doi: 10.1016/j.clinbiomech.2005.08.011.
- [76] P. Augat *et al.*, "Biomechanical methods for the assessment of fracture repair," *Injury*, vol. 45, no. SUPPL. 2, 2014, doi: 10.1016/j.injury.2014.04.006.
- [77] B. Kienast *et al.*, "An electronically instrumented internal fixator for the assessment of bone healing," *Bone Jt. Res.*, vol. 5, no. 5, pp. 191–197, May 2016, doi: 10.1302/2046-3758.55.2000611.
- [78] G. Bergmann, "OrthoLoad," *Orthoload*. Charité Universitaetsmedizin Berlin, 2008.
- [79] P. J. Prendergast, R. Huiskes, and K. Søballe, "Biophysical stimuli on cells during tissue differentiation at implant interfaces," *J. Biomech.*, vol. 30, no. 6, pp. 539–548, 1997, doi: 10.1016/S0021-9290(96)00140-6.
- [80] C. A. Grant, M. Schuetz, and D. Epari, "Mechanical testing of internal fixation devices: A theoretical and practical examination of current methods," *J. Biomech.*, vol. 48, no. 15, pp. 3989–3994, Nov. 2015, doi: 10.1016/J.JBIOMECH.2015.09.013.
- [81] P. Augat, U. Simon, A. Liedert, and L. Claes, "Mechanics and mechano-biology of fracture healing in normal and osteoporotic bone," *Osteoporos. Int.*, vol. 16, no. SUPPL. 2, 2005, doi: 10.1007/S00198-004-1728-9.
- [82] M. Privalov *et al.*, "Influence of reduction quality on functional outcome and quality of life in treatment of tibial plafond fractures: A retrospective cohort study," *BMC Musculoskelet. Disord.*, vol. 20, no. 1, pp. 1–8, Nov. 2019, doi: 10.1186/S12891-019-2932-2/TABLES/5.
- [83] J. Bellemans, K. Carpentier, H. Vandenuecker, J. Vanlauwe, and J. Victor, "The John Insall Award: Both morphotype and gender influence the shape of the knee in patients undergoing TKA," *Clin. Orthop. Relat. Res.*, vol. 468, no. 1, pp. 29–36, 2010, doi: 10.1007/S11999-009-1016-2.
- [84] B. L. Wise *et al.*, "The Association of Distal Femur and Proximal Tibia Shape with Sex: The Osteoarthritis Initiative," *Semin. Arthritis Rheum.*, vol. 46, no. 1, p. 20, Aug. 2016, doi: 10.1016/J.SEMARTHRT.2016.02.006.
- [85] H. Brzobohatá, V. Krajiček, Z. Horák, and J. Velemínská, "Sex classification using the three-dimensional tibia form or shape including population specificity approach," *J. Forensic Sci.*, vol. 60, no. 1, pp. 29–40, Jan. 2015, doi: 10.1111/1556-4029.12641.
- [86] H. Brzobohatá, V. Krajiček, Z. Horák, and J. Velemínská, "Sexual Dimorphism of the Human Tibia through Time: Insights into Shape Variation Using a Surface-Based Approach," *PLoS One*, vol. 11, no. 11, Nov. 2016, doi: 10.1371/JOURNAL.PONE.0166461.
- [87] O. L. Bruce, M. Baggaley, L. Welte, M. J. Rainbow, and W. B. Edwards, "A statistical shape model of the tibia-fibula complex: sexual dimorphism and effects of age on reconstruction accuracy from anatomical landmarks," *Comput. Methods Biomech.*

- Biomed. Engin.*, vol. 25, no. 8, pp. 875–886, 2022, doi: 10.1080/10255842.2021.1985111/SUPPL_FILE/GCMB_A_1985111_SM4474.DOCX.
- [88] D. S. Elliott *et al.*, “A unified theory of bone healing and nonunion: BHN theory,” *Bone Joint J.*, vol. 98-B, no. 7, pp. 884–891, 2016, doi: 10.1302/0301-620X.98B7.36061.
- [89] J. Elkins *et al.*, “Motion predicts clinical callus formation,” *J. Bone Jt. Surg. - Am. Vol.*, vol. 98, no. 4, pp. 276–284, 2016, doi: 10.2106/JBJS.O.00684.
- [90] S. H. Kim, S. H. Chang, and H. J. Jung, “The finite element analysis of a fractured tibia applied by composite bone plates considering contact conditions and time-varying properties of curing tissues,” *Compos. Struct.*, vol. 92, no. 9, pp. 2109–2118, 2010, doi: 10.1016/j.compstruct.2009.09.051.
- [91] J. Tan *et al.*, “Effects of bone-plate materials on the healing process of fractured tibia bone under time-varying conditions: a finite element analysis,” *Mater. Res. Express*, vol. 8, no. 9, p. 095308, Sep. 2021, doi: 10.1088/2053-1591/AC24F8.
- [92] J. Wieding, R. Souffrant, A. Fritsche, W. Mittelmeier, and R. Bader, “Finite Element Analysis of Osteosynthesis Screw Fixation in the Bone Stock: An Appropriate Method for Automatic Screw Modelling,” *PLoS One*, vol. 7, no. 3, p. e33776, Mar. 2012, doi: 10.1371/JOURNAL.PONE.0033776.
- [93] H. Wee, J. S. Reid, V. M. Chinchilli, and G. S. Lewis, “Finite Element-Derived Surrogate Models of Locked Plate Fracture Fixation Biomechanics,” *Ann. Biomed. Eng.*, vol. 45, no. 3, pp. 668–680, Mar. 2017, doi: 10.1007/s10439-016-1714-3.
- [94] G. S. Lewis, D. Mischler, H. Wee, J. S. Reid, and P. Varga, “Finite Element Analysis of Fracture Fixation,” *Curr. Osteoporos. Rep.*, vol. 19, no. 4, pp. 403–416, Aug. 2021, doi: 10.1007/s11914-021-00690-y.
- [95] P. Varga, J. A. Inzana, B. Gueorguiev, N. P. Südkamp, and M. Windolf, “Validated computational framework for efficient systematic evaluation of osteoporotic fracture fixation in the proximal humerus,” *Med. Eng. Phys.*, vol. 57, pp. 29–39, Jul. 2018, doi: 10.1016/j.medengphy.2018.04.011.
- [96] S. P. Wang, K. J. Lin, C. E. Hsu, C. P. Chen, C. M. Shih, and K. P. Lin, “Biomechanical comparison of a novel implant and commercial fixation devices for AO/OTA 43-C1 type distal tibial fracture,” *Appl. Sci.*, vol. 11, no. 10, 2021, doi: 10.3390/app11104395.
- [97] E. Pickering, M. J. Silva, P. Delisser, M. D. Brodt, Y. T. Gu, and P. Pivonka, “Estimation of load conditions and strain distribution for in vivo murine tibia compression loading using experimentally informed finite element models,” *J. Biomech.*, vol. 115, p. 110140, Jan. 2021, doi: 10.1016/J.JBIOMECH.2020.110140.
- [98] S. F. Scanlan, A. M. W. Chaudhari, C. O. Dyrby, and T. P. Andriacchi, “Differences in tibial rotation during walking in ACL reconstructed and healthy contralateral knees,” *J. Biomech.*, vol. 43, no. 9, pp. 1817–1822, Jun. 2010, doi: 10.1016/J.JBIOMECH.2010.02.010.
- [99] B. J. Braun *et al.*, “Individualized Determination of the Mechanical Fracture Environment After Tibial Exchange Nailing—A Simulation-Based Feasibility Study,” *Front. Surg.*, vol. 8, p. 432, Sep. 2021, doi: 10.3389/FSURG.2021.749209/BIBTEX.
- [100] S. Poelert, E. Valstar, H. Weinans, and A. A. Zadpoor, “Patient-specific finite element modeling of bones,” *Proc. Inst. Mech. Eng. Part H J. Eng. Med.*, vol. 227, no. 4, pp. 464–478, Apr. 2013, doi: 10.1177/0954411912467884.

- [101] E. Borgiani, G. N. Duda, and S. Checa, "Multiscale modeling of bone healing: Toward a systems biology approach," *Front. Physiol.*, vol. 8, no. MAY, p. 287, 2017, doi: 10.3389/fphys.2017.00287.
- [102] S. Checa, P. J. Prendergast, and G. N. Duda, "Inter-species investigation of the mechano-regulation of bone healing: Comparison of secondary bone healing in sheep and rat," *J. Biomech.*, vol. 44, no. 7, pp. 1237–1245, Apr. 2011, doi: 10.1016/j.jbiomech.2011.02.074.
- [103] S. Schumann, R. Bieck, R. Bader, J. Heverhagen, L. P. Nolte, and G. Zheng, "Radiographic reconstruction of lower-extremity bone fragments: a first trial," *Int. J. Comput. Assist. Radiol. Surg.*, vol. 11, no. 12, pp. 2241–2251, Dec. 2016, doi: 10.1007/s11548-016-1427-y.
- [104] R. H. Gong, J. Stewart, and P. Abolmaesumi, "Reduction of multi-fragment fractures of the distal radius using atlas-based 2D/3D registration," *Med. Imaging 2009 Vis. Image-Guided Proced. Model.*, vol. 7261, no. 13, p. 726137, Mar. 2009, doi: 10.1117/12.811638.
- [105] J. Buschbaum, R. Fremd, T. Pohlemann, and A. Kristen, "Introduction of a computer-based method for automated planning of reduction paths under consideration of simulated muscular forces," *Int. J. Comput. Assist. Radiol. Surg.*, vol. 12, no. 8, pp. 1369–1381, 2017, doi: 10.1007/s11548-017-1562-0.
- [106] F. A. Casari, S. Roner, P. Frnstahl, L. Nagy, and A. Schweizer, "Computer-assisted open reduction internal fixation of intraarticular radius fractures navigated with patient-specific instrumentation, a prospective case series," *Arch. Orthop. Trauma Surg.*, vol. 141, no. 8, pp. 1425–1432, 2021, doi: 10.1007/s00402-021-03856-6.
- [107] C. Zhao *et al.*, "Automatic reduction planning of pelvic fracture based on symmetry," *Comput. Methods Biomech. Biomed. Eng. Imaging Vis.*, 2021, doi: 10.1080/21681163.2021.2012830.
- [108] P. Frnstahl, G. Szkely, C. Gerber, J. Hodler, J. G. Snedeker, and M. Harders, "Computer assisted reconstruction of complex proximal humerus fractures for preoperative planning," *Med. Image Anal.*, vol. 16, no. 3, pp. 704–720, 2012, doi: 10.1016/j.media.2010.07.012.
- [109] R. Han *et al.*, "Fracture reduction planning and guidance in orthopaedic trauma surgery via multi-body image registration," *Med. Image Anal.*, vol. 68, p. 101917, Feb. 2021, doi: 10.1016/j.media.2020.101917.
- [110] M. S. Ead, M. Palizi, J. L. Jaremko, L. Westover, and K. K. Duke, "Development and application of the average pelvic shape in virtual pelvic fracture reconstruction," *Int. J. Med. Robot. Comput. Assist. Surg.*, vol. 17, no. 2, 2021, doi: 10.1002/rcs.2199.
- [111] L. Liu, X. Xu, X. Li, W. Wu, J. Cai, and Q. Lu, "Comparison of tibial intramedullary nailing guided by digital technology versus conventional method: A prospective study," *Med. Sci. Monit.*, vol. 23, pp. 2871–2878, 2017, doi: 10.12659/MSM.902261.
- [112] J. Wu, P. Davuluri, K. R. Ward, C. Cockrell, R. Hobson, and K. Najarian, "Fracture detection in traumatic pelvic CT images," *Int. J. Biomed. Imaging*, vol. 2012, 2012, doi: 10.1155/2012/327198.

